Charge Transport Analysis Using the Seebeck Coefficient-Conductivity Relation

Thesis by
Stephen Dongmin Kang

In Partial Fulfillment of the Requirements for the
degree of
Doctor of Philosophy

CALIFORNIA INSTITUTE OF TECHNOLOGY
Pasadena, California

2018
Defended May 14, 2018

Stephen Dongmin Kang
ORCID: 0000-0002-7491-7933

ACKNOWLEDGEMENTS

I am deeply indebted to many for all the support, collaboration, understanding, and criticism that has been invaluable to me throughout the course of graduate school. I must first express my gratitude to Jeff for giving me the opportunity to work with all the great minds in the group and supporting me in all the ways he did. He was one of the most open-minded, allowing me to not fear about exposing my naivety, but at the same time one of the most shrewd intellectuals, offering me the much needed insight and criticism. He was also one of the most generous, absorbing any of my unrefined actions that I failed to suppress. Without Jeff, the variety of topics that I was able to openly explore – including those not covered in this thesis – would not have been possible; any findings that I was able to learn and report could have been a pile of untied knots; the positive thinking that fuels the continuation and progress of research could have been mundane thought loops.

Much of the content in this thesis involved help from collaborators. Max Dylla helped me in the $SrTiO_3$ analysis part of Chapter II. Jimmy Kuo worked together with me on modeling work included in Chapter IV. Ian Witting did the reactivity testing included in Chapter VII. Jimmy Kuo and Ian Witting kindly reviewed the math and explanations in Chapter I. Any remaining errors are my own.

A number of have people supported me in winning a small prize from the International Thermoelectric Society during the last year of my doctoral research. Much appreciation to Prof. Narducci for spending the effort recommending me, and also for his professional interest in some of my work which led to valuable results. Prof. Chabinyc has not only recommended me, but also provided the original inspiration about conducting polymers with the stunning results from his research group. Alex Zevalkink was enthusiastically recommended me, which I am greatly thankful for. She was the first to defend from the Snyder group after I joined, and became such an encouraging role model to me and the group with a successful career path. She also offered me the opportunity to include parts of Chapter VI into her excellent review article.

I wish to give a big thanks to all the group members who made graduate school an enjoyable and intellectually stimulating experience. Saneyuki was the best comrade during the hardest times, sharing all the vents, beer, and whiskey. Jimmy and Kazuki most patiently absorbed my knowledge and quickly transformed into experts that

give me intellectual challenges, and I have learned much by working with them on their career-first projects. Hyun-Sik was one of the first to most kindly greet me to the group, and continued to help me out on so many matters despite himself being in a much demanding situation than me. Umut did not hesitate in helping me learn the lab environment at the very beginning when it was most needed, and was an extremely pleasant office mate during the times at Caltech. David invited me into exceptionally stimulating discussions, which naturally became the foundation of my first research projects in the group. I feel sorry that my work did not develop into what he had originally envisioned. Zach and Heng were kind enough to bear with my annoying questions when I was new to the group, and thanks to those teachings I was able to get involved in transport modeling for my later thesis projects. Tristan and Fivos gave me a good head start in chalcogenide synthesis, and I much appreciate their willingness to share all the experience with no hesitation. Nick was a charismatic leader in the lab who helped me learn the rules and culture of the lab. Yinglu set such a good example in excellence, which kept up the morale in the group. Saurabh helped me try out computational research, from which I have benefited much in appreciating literature in that field. Brett had such elegant machining skills and I owe him for much of my instrumentation work. Sam and Thomas were such kind helping hands, and without them it could have been very frustrating to get started at Northwestern. Ian was the one who appreciated the hardness of instrumentation, and kindly engaged into discussions that helped me solve problems. Riley always kept the approachable atmosphere in the main office, which I appreciate much. Matthias has fueled the late year group meetings with mind-stimulating fluids which kept my motivation alive for joining. He has also found some of my previous work interesting enough to be built upon, which I sincerely appreciate. Max Dylla has given me many exciting moments of discovery, thanks to the enlightening collaboration. Max Wood has shown great responsibility and awareness in the lab, thanks to which members and I were able to keep focused on projects. Shash showered me with great questions that alerted me to really reexamine myself if I understood things correctly. Jun has brought a totally new subject to the table, and I am indebted for being given the chance to have such a refreshing experience while working together. I must also thank Sev, Wolf, and Stefan for all the awesome events.

Graduate school would have been only a fancy without the support and guidance of my previous advisor Prof. Ki-Bum Kim at Seoul National University and also my previous supervisor Dr. Lyeo at Korea Research Institute of Standards and Science.

Funding support from both the AFOSR MURI program (FA9550-12-1-0002) and the Solid-State Solar- Thermal Energy Conversion Center, an Energy Frontier Research Center funded by the U.S. Department of Energy, Office of Science, Basic Energy Sciences (DE-SC0001299) is acknowledged.

Lastly, I dedicate this thesis to my dear wife Taeyeon, and my parents.

ABSTRACT

Charge transport properties like electrical conductivity or the Seebeck coefficient are defined phenomenologically from near-equilibrium thermodynamics, while the analysis or modeling of them often involves a physical model based on mechanistic principles. In other words, physical models connect microscopic and physical parameters to phenomenological and experimental properties. One of the challenges is that the complexity of solid state requires many physical parameters, whereas the measurable properties which help to determine those parameters are limited. The interrelations of measured properties are very important to overcome this challenge, but this aspect is not well recognized in conventional analysis themes. In this thesis, the concept of using a phenomenological transport function is devised to help combine a collection of measurements into an intermediate level of phenomenology, relevant for fermion transport but not dependent on a particular physical model. This phenomenological transport function can be determined by examining the electrical conductivity, the Seebeck coefficient, and potentially the Lorenz number. Because the phenomenological transport function combines information from a set of multiple measurable properties, a direct comparison to the transport function of a physical model serves as a strong test for the model.

Particular usefulness comes from extracting transport functions from the Seebeck coefficient-conductivity relation, especially in doped semiconductors. This approach is applied to contrast CeO_{2-x} and n-type $SrTiO_3$ as narrow and dispersive transport function materials, each consistent with polaron and band conduction, respectively. In band conductors such as $SrTiO_3$ and Mg_3Sb_2, the approach is used to test and refute previous claims about the scattering mechanism and find consistency with deformation potential scattering in both cases. In conducting polymers, which do not resemble any other type of conventional conductors, the Seebeck-conductivity relation reveals a qualitative disagreement with the commonly cited Mott's models. For the case of Cu_2Se, a peculiar band conductor which shows anomalies in the Hall measurement of the high temperature phase and also in other transport properties at the phase transition, the transport function approach is applied as a workaround for modeling. On the practical side, for thermoelectric applications, the transport function approach is used to characterize material quality factors for both majority carrier conduction and bipolar conduction. Finally, experimental efforts for improving the accuracy and applicability of Seebeck measurements is discussed.

PUBLISHED CONTENT AND CONTRIBUTIONS

[1] S. D. Kang, M. Dylla, and G. J. Snyder, "Thermopower-conductivity relation for distinguishing transport mechanisms: polaron hopping in CeO_2 and band conduction in $SrTiO_3$", Physical Review B, accepted (2018).

Developed the theory, analyzed data, and wrote the manuscript.

[2] S. D. Kang and G. J. Snyder, "Charge-transport model for conducting polymers", Nature Materials **16**, 252–257 (2017) 10.1038/nmat4784.

Developed the theory, analyzed data, and wrote the manuscript.

[3] S. D. Kang, J.-H. Pöhls, U. Aydemir, P. Qiu, C. C. Stoumpos, R. Hanus, M. A. White, X. Shi, L. Chen, M. G. Kanatzidis, and G. J. Snyder, "Enhanced stability and thermoelectric figure-of-merit in copper selenide by lithium doping", Materials Today Physics **1**, 7–13 (2017) 10.1016/j.mtphys.2017.04.002.

Synthesized the samples, measured properties, performed the analysis, and wrote the manuscript.

[4] S. D. Kang, S. A. Danilkin, U. Aydemir, M. Avdeev, A. Studer, and G. J. Snyder, "Apparent critical phenomena in the superionic phase transition of $Cu_{2-x}Se$", New Journal of Physics **18**, 013024 (2016) 10.1088/1367-2630/18/1/013024.

Synthesized the samples, measured sample properties, analyzed data, and wrote the manuscript.

[5] S. D. Kang and G. J. Snyder, "Transport property analysis method for thermoelectric materials: material quality factor and the effective mass model", arXiv:1710.06896 [cond-mat.mtrl-sci], https://arxiv.org/abs/1710.06896.

Developed the framework and wrote the manuscript.

[6] J. J. Kuo, S. D. Kang, K. Imasato, H. Tamaki, S. Ohno, T. Kanno, and G. J. Snyder, "Grain boundary dominated charge transport in Mg_3Sb_2-based compounds", Energy & Environmental Science **11**, 429–434 (2018) 10.1039/C7EE03326E.

Equal contribution with J. J. Kuo. Developed the model, analyzed data, and wrote the manuscript.

[7] K. Nan, S. D. Kang, K. Li, K. J. Yu, F. Zhu, J. Wang, A. C. Dunn, C. Zhou, Z. Xie, M. T. Agne, H. Wang, H. Luan, Y. Zhang, Y. Huang, G. J. Snyder, and J. A. Rogers, "Compliant and stretchable thermoelectric coils for energy harvesting in miniature flexible devices", under review (2018).

Equal contribution with K. Nan and K. Li. Oversaw the thermal and thermoelectric analyses, measured the thermoelectric properties, modeled the thermal and power characteristics, and wrote the manuscript.

[8] J. Peng, S. D. Kang, and G. J. Snyder, "Optimization principles and the figure of merit for triboelectric generators", Science Advances **3**, eaap8576 (2017) 10.1126/sciadv.aap8576.

Equal contribution with J. Peng. Developed the dimensionless model, analyzed simulation results, and wrote the manuscript.

[9] K. Imasato, S. D. Kang, S. Ohno, and G. J. Snyder, "Band engineering in Mg_3Sb_2 by alloying with Mg_3Bi_2 for enhanced thermoelectric performance", Materials Horizons **5**, 59–64 (2018) 10.1039/C7MH00865A.

Supervised the project. Assisted in the measurements and analysis, and wrote the manuscript.

[10] K. Imasato, S. Ohno, S. D. Kang, and G. J. Snyder, "Improving the thermoelectric performance in $Mg_{3+x}Sb_{1.5}Bi_{0.49}Te_{0.01}$ by reducing excess Mg", APL Materials **6**, 016106 (2018) 10.1063/1.5011379.

Assisted in the analysis and edited the manuscript.

[11] T. Kanno, H. Tamaki, H. K. Sato, S. D. Kang, S. Ohno, K. Imasato, J. J. Kuo, G. J. Snyder, and Y. Miyazaki, "Enhancement of average thermoelectric figure of merit by increasing the grain-size of $Mg_{3.2}Sb_{1.5}Bi_{0.49}Te_{0.01}$", Applied Physics Letters **112**, 033903 (2018) 10.1063/1.5016488.

Analyzed the transport data and partially wrote the manuscript.

[12] S. Ohno, K. Imasato, S. Anand, H. Tamaki, S. D. Kang, P. Gorai, H. K. Sato, E. S. Toberer, T. Kanno, and G. J. Snyder, "Phase boundary mapping to obtain n-type Mg_3Sb_2-based thermoelectrics", Joule **2**, 141–154 (2018) 10.1016/j.joule.2017.11.005.

Conceived the project. Assisted the interpretation and wrote the manuscript.

[13] H.-S. Kim, N. A. Heinz, Z. M. Gibbs, Y. Tang, S. D. Kang, and G. J. Snyder, "High thermoelectric performance in $(Bi_{0.25}Sb_{0.75})_2Te_3$ due to band convergence and improved by carrier concentration control", Materials Today **20**, 452–459 (2017) 10.1016/j.mattod.2017.02.007.

Assisted in the crystal growth and characterization.

[14] H.-S. Kim, S. D. Kang, Y. Tang, R. Hanus, and G. J. Snyder, "Dislocation strain as the mechanism of phonon scattering at grain boundaries", Materials Horizons **3** (2016) 10.1039/C5MH00299K.

Assisted in the modeling and edited the manuscript.

[15] U. Aydemir, J.-H. Pöhls, H. Zhu, G. Hautier, S. Bajaj, Z. M. Gibbs, W. Chen, G. Li, S. Ohno, D. Broberg, S. D. Kang, M. Asta, G. Ceder, M. A. White, K. Persson, A. Jain, and G. J. Snyder, "$YCuTe_2$: a member of a new class of thermoelectric materials with $CuTe_4$-based layered structure", Journal of Materials Chemistry A **4**, 2461–2472 (2016) 10.1039/C5TA10330D.

Characterized and analyzed the phase transition.

[16] M. Hong, Z.-G. Chen, L. Yang, T. C. Chasapis, S. D. Kang, Y. Zou, G. J. Auchterlonie, M. G. Kanatzidis, G. J. Snyder, and J. Zou, "Enhancing the thermoelectric performance of $SnSe_{1-x}Te_x$ nanoplates through band engineering", Journal of Materials Chemistry A **5**, 10713–10721 (2017) 10.1039/C7TA02677C.

Assisted in the measurements and analysis.

[17] S. Maier, S. Ohno, G. Yu, S. D. Kang, T. C. Chasapis, V. A. Ha, S. A. Miller, D. Berthebaud, M. G. Kanatzidis, G.-M. Rignanese, G. Hautier, G. J. Snyder, and F. Gascoin, "Resonant bonding, multiband thermoelectric transport, and native defects in n-type $BaBiTe_{3-x}Se_x$ (x = 0, 0.05, and 0.1)", Chemistry of Materials **30**, 174–184 (2017) 10.1021/acs.chemmater.7b04123.

Assisted in the measurements and analysis.

TABLE OF CONTENTS

Acknowledgements . . . iii
Abstract . . . vi
Published Content and Contributions . . . vii
Table of Contents . . . x
List of Illustrations . . . xii
List of Tables . . . xxi
List of Symbols . . . xxii
Chapter I: Charge transport analysis: phenomenological vs. physical model approach . . . 1
1.1 Semiclassical band transport . . . 3
1.2 Nearest neighbor hopping . . . 18
1.3 Semiclassical phenomenology of transport . . . 20
Chapter II: Polaron vs. band conduction: CeO_2 and $SrTiO_3$ . . . 29
2.1 Band conduction in $SrTiO_3$ . . . 32
2.2 Small polaron conduction in CeO_2 . . . 38
2.3 Notes on assumptions related to modeling oxide materials . . . 40
2.4 Appendix: Physical transport model for n-type $SrTiO_3$ . . . 42
Chapter III: Phenomenology in conducting polymers . . . 48
3.1 Failure of Mott's models for conducting polymers . . . 48
3.2 Phenomenological characterization of conducting polymers . . . 50
3.3 Physical interpretation of the phenomenological transport function . . . 55
3.4 Appendix: Chemical abbreviations . . . 58
Chapter IV: Inhomogeneous transport: Mg_3Sb_2 . . . 62
4.1 Erroneous interpretation of the thermally activated conduction . . . 62
4.2 Limitations in the homogeneous approach . . . 65
4.3 Mg_3Sb_2 modeled with an inhomogeneous approach . . . 68
Chapter V: Anomalous transport: superionic Cu_2Se . . . 77
5.1 Transport analysis of the superionic phase . . . 78
5.2 Two-phase description of the anomalous transport observed during the superionic phase transition . . . 83
5.3 Experimental notes on synthesis and stoichiometry control . . . 86
Chapter VI: Application to thermoelectrics: material quality factor . . . 90
6.1 Concept and derivation of the thermoelectric material quality factor . . . 90
6.2 Determination of B from measurements on S, σ, and κ . . . 95
6.3 Application to thermoelectric materials . . . 96
6.4 Quality factors for bipolar conduction and peak zT . . . 97
6.5 Appexdix: Derivation of bipolar thermal conductivity . . . 102
Chapter VII: Seebeck metrology: thermocouple probe issues and improvement strategies . . . 105

7.1 Limitations in using conventional thermocouples as probes 105
7.2 Candidate thermocouples and testing 108
7.3 Thermocouple vacuum feedthroughs: issues in commercial products and custom solutions 111
Chapter VIII: Concluding Remarks 114
Appendix A: Near-equilibrium transport equations: thermodynamic phenomenology 116
A.1 Generalized forces, fluxes, and Onsager reciprocity 116
A.2 Charge transport from electric fields and temperature gradients . . . 117

LIST OF ILLUSTRATIONS

Number *Page*

1.1 Fermi-Dirac distribution function and related "sampling" functions. **(a)** Fermi-Dirac distribution function **(b)** Sampling function relevant for electrical conductivity. Contribution to conduction comes from only near the Fermi-level E_F. **(c)** Sampling function relevant for the Seebeck coefficient. Contribution comes from only near the E_F, but with an opposite sign with respect to E_F. **(d)** Sampling function relevant for the (zero field) electronic thermal conductivity. Contribution comes from both above and below the E_F with the same sign, but is zero at the E_F. 8

1.2 The thermopower-conductivity relation plotted for a number of phenomenological exponents. In the degenerate limit (low $|S|$) the linear slope of the log-log plot is $-\frac{1}{s}$. In the non-degenerate limit (high $|S|$), all cases have an identical curve shape. The narrow transport function case is shown together in green for comparison (for which conductivity is normalized such as σ/σ_{E_0}), being very similar to $s = 0$. Practically, $s = 0$ is not considered a physically feasible case. 24

2.1 Schematic illustration of two processes that result in thermally activated conduction. Process ① is due to the Fermi-level being below the transport edge, whereas process ② is due to the transport function itself being a thermally activated process. 31

2.2 Analysis of the $\log|S| - \log\sigma$ relation in single crystal n-type $SrTiO_3$ doped with either La (circles) or Nb (squares). At **(a)** 450 K, data clearly follow the $s = 1$ relation rather than the Heikes relation, indicating band transport. At **(b)** 1050 K, the thermopower of the samples are too large to distinguish between different mechanisms. Data are from Ref.[17]. 32

2.3 Low temperature (120 K) analysis of the $\log|S| - \log\sigma$ relation in single crystal n-type $SrTiO_3$ doped with La. Conductivity of the open circle data point was interpolated from adjacent compositions. Data are from Ref.[18]. 33

2.4 The temperature dependent relaxation time of the light carriers in n-type single crystal $SrTiO_3$ extracted from thermopower and conductivity using Eq.2.5. A dashed line of $\propto T^{-2}$ dependency is drawn for comparison. High and low temperature data are from Ref.[17] and Ref.[18], respectively. The lattice constant was fixed at $a = 3.905$ Å [32] for the calculation. 35

2.5 Analysis of the $\log|S| - \log\sigma$ relation in single crystal n-type CeO_{2-x}, reduced to different compositions by CO/CO_2 atmosphere control. The data follow the Heikes relation rather than $s = 1$, indicating that a narrow transport function is governing the transport in this material (such as small polaron conduction). Data are from Ref.[15]. To find the thermopower corresponding to each conductivity measurement, the Seebeck coefficient vs. composition data reported in the same reference was fitted to find an empirical relation, which was then applied to the conductivity vs. composition data. 38

2.6 Temperature dependency of the Seebeck coefficient in single crystal CeO_{2-x}. The data set is a compilation from two studies as reported in Ref.[15]. The dashed lines are guides to the eye showing the average value with respect to temperature. 39

3.1 The thermopower-conductivity relation found from F4TCNQ- and FTS-doped polythiophenes at room temperature. Data are from Ref.[17]. The gray dashed line is a fitting based on the mobility edge model as presented in the same reference. The gray dotted line is an evaluation of the variable range hopping model as presented in the same reference. The black dashed-dotted line is the relation for a narrow transport function. The black solid line is the relation with a phenomenological exponent $s = 3$, showing the best fit to the data. Chemical abbreviations are listed in Table.3.1. 50

3.2 Phenomenological characterization of charge transport in polyacetylene. **(a)** Literature compilation of polyacetylene thermopower-conductivity data, as reported in Ref.[20]. The $s = 3$ transport exponent identified from polythiophenes (Fig.3.1) appears to also approximately fit the overall trend of polyacetylene. **(b)** Analysis of the temperature dependency. Using thermopower-conductivity data from three samples reported in Ref.[21], σ_{E_0} was extracted using the $s = 3$ relation and plotted (black data points; left axis). The activation energy ($W_{\frac{1}{2}} \approx 1$ eV; Eq.3.1) appears identical in all three samples despite vastly different doping levels (the slope is identical in the three black fits). By contrast, a simple variable range hopping analysis (gray data points; right axis) shows activation energies dependent on the doping level. 51

3.3 Compilation of room temperature Seebeck-conductivity data of various conducting polymers. Data are from Refs.[17, 20, 22–24]. The dashed lines show the $s = 3$ model relation with different values of σ_{E_0} as annotated on each line. As a guide to eyes, the markers are colored in accordance to the approximate value of average σ_{E_0} observed in each data set. Chemical abbreviations are listed in Table.3.1. . . . 53

3.4 The Seebeck-conductivity relation in PEDOT:tosylate and PEDOS-C_6. Data are from Refs.[9, 25]. The black lines show the $s = 1$ model relation with different values of σ_{E_0} as annotated on each line. The $s = 3$ relation found from other polythiophenes in Fig.3.1 is plotted together (gray dotted line) for reference. Chemical abbreviations are listed in Table.3.1. 54

4.1 Temperature dependent properties of n-type Mg_3Sb_2-based compounds: **(a)** Hall mobility (data from Ref.[3]); **(b)** Conductivity (data from Ref.[4]). 63

4.2 The $S-\sigma$ relation in n-type $Mg_{3+\delta}Sb_{1.5}Bi_{0.5}$ polycrystalline samples doped with various amounts of Te. The $S-\sigma$ relation for deformation potential scattering (dashed line) and ionized impurity scattering (dotted line) are drawn together for comparison. The data at each temperature show a relation that better resembles deformation potential scattering rather than ionized impurity scattering. The two-phase grain boundary model is shown to well describe the data at both low and high temperatures. Data are from Refs.[3, 4]. Regions of bipolar conduction were excluded from the plot and analysis. 65

4.3 Crossover behavior in the temperature exponent with respect to temperature (normalized with the crossover temperature) as described in Eq.4.6. The crossover is gradual with respect to the normalized temperature. 67

4.4 Schematic potential landscape for an electron across a grain boundary when grain boundary-induced charge transfer produces a potential barrier and associated charge depletion regions. The conduction band minimum is indicated as CBM and the potential barrier height is represented as $-e\phi$. 68

4.5 The simplified two phase grain boundary transport model. **(a)** An effective band offset of ΔE takes into account the potential barrier. This offset relates the Fermi-level of each phase (defined relative to the band edge of each phase). **(b)** A series circuit representation of the two phase model, which is equivalent to the core-shell effective medium model in the limit of a small grain boundary phase relative to the grain phase. 69

4.6 Band offsets that give the best fit for individual samples at a given temperature. The overall trend shows an increasing relation between the band offset and Fermi-level, which is a trend that is expected from the charge transfer mechanism that produces the offset. A linear fit to the individually determined offset values is used as an empirical function for determining the band offset in the data set. While this procedure apparently reduces the quality of the fits, it greatly reduces the fitting degree-of-freedom and also gives predictive power to the model. Circled and squared data points are from Refs.[4] and [3], respectively. 71

4.7 The grain boundary transport model using parameters listed in Table 4.1. **(a)** Conductivity as a function of temperature, showing good agreement with data. Data points are from Refs.[3, 4]. **(b)** Drift mobility calculated from the conductivity in (a) and using a density-of-states effective mass of $m^*_{\mathrm{DOS}} = N_{\mathrm{V}}^{2/3} m^*_{\mathrm{b}} \approx 6^{2/3} 0.3 m_{\mathrm{e}}$. 72

4.8 The grain boundary model applied to a different data set where the grain size was changed. All model parameters were fixed to that in Table 4.1 expect for t_{GB}. The scaling in t_{GB} required to best fit the data is similar to that of the measured average grain size. The model limit with no grain boundary resistance ($t_{\mathrm{GB}} = 0$) is also shown for comparison. Data points are from Ref.[2]. 73

5.1 Measured **(a)** Hall carrier concentration ($n_{\mathrm{H}} = 1/R_{\mathrm{H}}/e$) and **(b)** Seebeck coefficient of $Cu_{1.985}Se$ in the superionic cubic phase. Solid lines are guides to the eyes. 78

5.2 m^*_{Seeb} extracted from n_{H} and S in Fig.5.1, apparently showing a significant increase with temperature. 79

5.3 Measured **(a)** electrical resistivity and **(b)** Seebeck coefficient of $Cu_{2-x}Se$ and related compounds in the superionic cubic phase. Literature data from Ref.[3] is shown together for comparison. 80

5.4 Weighted mobilities extracted from the Seebeck coefficient and conductivity data shown in Fig.5.3. At high temperatures where minority carriers negate the thermopower from the majority hole carriers, the extracted μ_{w} values (solid lines) show a further decrease than the extrapolated trend; the extrapolated lines (dotted lines) are what is expected for the majority carriers. Extracted values in the bipolar conduction region could be considered an effective overall value. The Li-doped compound does not show any sign of bipolar conduction up to 1000 K due to an enlarged band gap. The unexpected break in the literature-extracted μ_{w} curve (gray dashed line; Ref.[3]) around 800 K corresponds to the temperature where the Seebeck measurement (Fig.5.3) shows a sudden increase in the $S(T)$ slope. . . 80

5.5 Determining the thermoelectric figure-of-merit in Cu_2Se. **(a)** Thermal conductivity evaluated by measuring the thermal diffusivity with the laser flash method. Identical heat capacity values as reported in Ref.[3] were used for the comparison. **(b)** Thermoelectric figure-of-merit zT evaluated. It is seen that the literature data apparently shows no sign of bipolar conduction in the zT curve. In the current study, suppressed bipolar conduction is only seen in Li-doped samples, in which the band gap is enlarged due to the alloying effect with Li_2Se, a wide band gap compound [10]. The discrepancy is attributed to the Seebeck measurement as seen in Figs.5.3 and 5.4. 82

5.6 Thermoelectric figure-of-merit evaluation near the superionic phase transition of Cu_2Se. Use of the Dulong-Petit value results in an erroneous overestimation in the zT value. Literature data are from Refs.[16, 17]. 83

5.7 Transport properties of $Cu_{1.99}Se$ near the superionic phase transition. **(a)** Conductivity measured upon heating with a rate of 6 K/h. The kink around 380 K indicates the onset of the phase transformation. The red solid line represents the calculated result from effective medium theory. **(b)** Seebeck coefficient measured upon repeated heating cycles with a ramping rate of 25 K/h. Each marker type represents a measurement with a different sample loading (cycled multiple times with a given loading) using the same sample. The filled circle markers represent the behavior observed in the majority of loadings. The open square markers represent a minority behavior occasionally observed. The difference is attributed to different microstructure evolution during the phase transformation with respect to the loaded probes. The dashed line shows the calculated upper bound from effective medium theory (microstructure equivalent to a series circuit connection of two phases) and dotted line shows the lower bound (equivalent to a parallel circuit). 85

6.1 Thermoelectrics-related properties as a function of reduced Fermi-level. **(a)** Thermopower is a decreasing function with η whereas conductivity and thermal conductivity is an increasing function with η. Figure-of-merit is thus a peaked function with respect to η. **(b)** Carrier concentration is an increasing function with η and is the primary means for controlling η. 91

6.2 Quality factor analysis for $s = 1$, applicable to thermoelectric materials dominated by deformation potential scattering. **(a)** The $zT(\eta)$ curve is determined for a given B. The curves are calculated by substituting Eqs.1.77,1.79, and 1.80 into Eq.6.3. **(b)** The peak zT value for a given B. Note that $B = 0.4$ gives a peak $zT > 1$. **(c)** The optimum thermopower $|S|$ at at which the peak zT occurs **(d)** The optimum carrier concentration n_{opt} at which the peak zT occurs, multiplied by a scaling factor that depends on the density-of-states effective mass and temperature. Example calculation: at $B = 0.4$ the vertical axis reads 1.2×10^{19} /cm^3; if $m^*_{\text{DOS}} = 3m_{\text{e}}$ and $T = 500$ K, then $n_{\text{opt}} = 1.2 \times 10^{19} \cdot (\frac{500}{300} \times 3)^{3/2} = 1.3 \times 10^{20}$ /cm^3. 94

6.3 Quality factor analysis for $s = 3$. **(a)** The peak zT value for a given B. **(b)** The optimum thermopower at at which the peak zT occurs. . 95

6.4 Quality factor analysis for Cu_2Se. The Li-doped sample (filled circle), calculated to have a quality factor of $B = 0.58$ at 930 K based on the data shown in Figs.5.3-5.5, appears to be doped to a near-optimum level. The undoped sample (open circle) has a similar B factor if the B of majority p-type carriers is inferred from extrapolation (Fig.5.4), but the actual zT is smaller due to the bipolar effect reducing the Seebeck coefficient. The η value of the undoped sample is an effective value converted from S with the non-bipolar equation (Eq.1.79). 96

6.5 Peak zT and T_{peak} due to majority carriers from the quality factors (B_1, B_2) for bipolar conductors. **(a)** The peak zT value obtainable for given quality factors (B_1, B_2). **(b)** The reduced band gap $E_{\text{g}}/k_{\text{B}}T$ at which the peak zT occurs. Example calculation: if $B_2 = 1$ and $B_1 = 1.7$, the peak zT obtainable is $zT \approx 1$; this peak zT occurs at a reduced gap $E_{\text{g}}/k_{\text{B}}T \approx 6.1$; if the band gap is $E_{\text{g}} = 0.3$ eV, then the peak zT would occur at $0.3 \text{ eV}/6.1k_{\text{B}} \approx 570\ K$. 100

7.1 Schematic of the thermocouple placement on a sample for Seebeck measurements. The temperature difference ΔT is measured between two thermocouple junctions, whereas the voltage difference ΔV is measured between the two sample terminals. This position difference for ΔT and ΔV contributes to an error in the Seebeck coefficient measurement. Another source of error is the temperature difference between the two probe wire contacts (red wire contacts with the sample). Because the temperatures are different, an additional voltage from the red wire Seebeck coefficient is measured in ΔV, which should be corrected from the measurement. However, that correction relies on the measured ΔT, which is from a different position. Therefore, the error due to the position difference between ΔV and ΔT is amplified with this second source of error. 106

7.2 Thermoelectric properties of Nb. **(a)** Seebeck coefficient **(b)** Thermoelectric voltage with respect to a reference junction at 0°C. Curves are based on data from Ref.[1]. 107

7.3 Pt reactivity with Sb vapor pressure. A type S thermocouple was sealed in a vacuumed fused quartz tube together with shots of Sb. The thermocouple and Sb were placed at opposite ends of the tube. After annealing at 500 °C, the thermocouple exposed to Sb vapor pressure turned black while no visual sign of Sb deposition was observed at any other places in the tube. Compare with the control where the thermocouple remained intact after the identical annealing conditions but without the Sb vapor pressure. 108

7.4 W95Re5/Nb thermocouples for Seebeck measurements. **(a)** Calibrated thermoelectric voltage of W95Re5/Nb with respect to a reference junction at 0°C (solid line), compared with type Chromel/Nb (dashed line) and W/Nb thermocouples (dotted line). Calibration was done by putting W95Re5/Nb in contact with a type S thermocouple in a vacuum furnace, and repeating heating and cooling cycles while recording voltage readings. Chromel data is from ITS-90 [3, 4]; W data is from Refs.[5, 6]; Nb data is from Fig.7.2. **(b)** Near room-temperature measurement test on a Bi_2Te_3 sample. The Seebeck coefficients measured using pristine W95Re5/Nb thermocouples agree well with those made using Chromel/Nb thermocouples. 109

7.5 Drift in the thermoelectric voltage signal in W95Re5/Nb thermocouples. **(a)** During a 3d annealing test at 900 °C, a reduction in the thermoelectric voltage is observed. **(b)** The resulting voltage curve after the 900 °C annealing shows a permanent reduction in signal. . 110

7.6 Making a custom thermocouple feedthrough for vacuum chambers. **(a)** For easy placement and isolation between two wires, the wires are inserted in a multi-bore alumina tube. The tube is then inserted into a stainless steel 1/4 in. tube. Stuffing in wax paper at one side of the tube can help to maintain the tube in a neutral position throughout the process. **(b)** The tube is filled in with TorrSeal epoxy. After applying the expoxy, the ceramic tube is pulled into the stainless steel tube to help move the epoxy in. Multiple cycles are repeated to get a thick layer of epoxy. **(c)** Cured at room temperature for a day. **(d)** The gas tube is attached to a commercial gas feed through using standard compression fittings with sleeves. 112

LIST OF TABLES

Number *Page*

1.1 Parameters in $\tau = \tau_0(T) \cdot \left(\frac{E}{k_B T}\right)^r$ for various scattering mechanisms. The exponent r is the leading order term for the energy dependency. . 16

3.1 Abbreviations for chemical formulae used in the current chapater . . 58

4.1 Parameters for the two-phase transport model of polycrystalline n-type $Mg_{3+\delta}Sb_{1.5}Bi_{0.5}$ doped with Te 70

LIST OF SYMBOLS

ρ	Electrical resistivity
σ	Electrical conductivity
L	Lorenz number
S	Seebeck coefficient
n	Carrier concentration
R_{H}	Hall coefficient
n_{H}	Hall carrier concentration
κ	Thermal conductivity κ_{L} lattice; κ_{e} electronic; κ_{B} bipolar; κ_0 zero-field electronic.
g	Density of electronic states
m^*	Effective Mass m^*_{b} band; m^*_{Hall} Hall; m^*_{Seeb} Seebeck; m^*_{DOS} desnity-of-states; m^*_{I} inertial.
μ	Mobility μ_{H} Hall; μ_{d} Drude; μ_{w} weighted; μ_0 parameter.
τ	Charge carrier relaxation time
q	Charge of carrier (signed)
E_{F}	Fermi-level (electron chemical potential)
F_i	Complete Fermi integral of ith order (non-normalized)
η	Reduced Fermi-level
f	Fermi-Dirac distribution function
E_t	Phenomenological transport edge
σ_E	Phenomenological transport function
σ_{E_0}	Phenomenological transport coefficient
s	Phenomenological transport exponent
T	Temperature
$\boldsymbol{E}$	Electric field

$\boldsymbol{J}$	Electrical current density
$\boldsymbol{U}$	Heat flux
E	Charge carrier energy
$\boldsymbol{k}$	Bloch wave vector
B	Thermoelectric material quality factor (dimensionless)
zT	Thermoelectric material figure-of-merit

Constants

e	Elementary charge
k_{B}	Boltzmann constant
m_{e}	Electron mass
$\hbar$	Reduced Plank constant
h	Plank constant

Chapter 1

CHARGE TRANSPORT ANALYSIS: PHENOMENOLOGICAL VS. PHYSICAL MODEL APPROACH

In solid state, charge transport is the central phenomena in a majority of electronic applications. In addition to its wide technical relevance, it is also intimately related to basic solid state properties such as the crystal structure, electronic structure, defect distribution, microstructure, and phonon properties. Because of such property relations, charge transport is routinely used as a tool to study the basic properties of a solid. It is apparent from the wide involvement that analysis of charge transport phenomena is one of the most fundamental topics in the study of solid materials.

Charge transport happens because of the presence of a driving force. For example, stationary driving forces like static electric or magnetic fields, thermal gradients, and chemical potential gradients are all capable of inducing steady-state charge transport. In fact, thermodynamics states that any general driving force can induce charge transport. How charge transport happens in response to a specific driving force (or a set of them) is what is called the transport properties.

Charge transport properties are phenomenologically (*i.e.* without specification about the mechanism of transport) defined using thermodynamics (see Appendix A for a detailed description). The presence of a driving force and charge transport indicates a non-equilibrium situation, according to the second law of thermodynamics. Nevertheless, transport properties can be well described with equilibrium properties in the limit of small driving forces, a regime referred to as "near-equilibrium" or the linear response regime. In this regime, fluxes (*e.g.* charge flux) are proportional to driving forces (*e.g.* electric field), from which the proportional constant can be defined as a transport property (*e.g.* electrical conductivity). Properties defined by this general phenomenology include electrical and thermal conductivity, the Seebeck coefficient, Lorenz number, and Hall coefficient. The phenomenology is not restricted to stationary driving forces; however, the primary interest of this thesis is on stationary properties.

Charge transport properties can be modeled using physical parameters and mechanistic principles, an approach that could be termed the "physical model" approach, or alternatively, the "mechanistic model" approach. For example, one could model

electrical conductivity with a function $F(a, b, c)$ where a, b, c are parameters related to specific physical quantities like temperature, mass, or velocity and F is a function that describes elementary physics principles. As seen in this example, physical models make the connection between elementary physical quantities and the general phenomenology.

Doing experimental measurements is naturally a phenomenological approach, whereas the analysis of experiments is ultimately a physical model approach. For example, because phenomenology defines what electrical conductivity is, it also dictates how electrical conductivity should be measured. Then, one would ideally want to either be able to predict conductivity with a function $F(a, b, c)$ or be able to infer a, b, c from the measurement, based on a physical model that gives the expression for F.

A general difficulty associated with validating a physical model is that numerous physical parameters (like $a, b, c, \ldots$) are needed to describe a single property. This difficulty is partly overcome by testing if the derivative with respect to each parameter, such as the temperature dependency of conductivity, agrees with experiments. However, more than often, physically controllable or measurable parameters are limited and the analysis is challenged with the risk of over-fitting (mathematically too many degrees-of-freedom for fitting). A much stronger test for a model is to see if the same set of model parameters also explain other transport properties, like the Seebeck coefficient or Lorenz number, simultaneously. However, this test for self-consistency is not always straightforward due to complexities in transport models. Above all, it is not a well-established procedure to study the interrelation of transport properties in the context of testing transport models (some cases are found in Refs.[1, 2]).

This difficulty in directly tackling the most general phenomenology (*i.e.* experimental measurements) could be eased if we had a phenomenological model or framework that can be extracted from experimental measurements in a manner that is not dependent on a particular physical model. For example, if the information in electrical conductivity and the Seebeck coefficient could be combined to determine an underlying phenomenological function that determines both properties, this phenomenological function would help the experimentalist to test the self-consistency of physical models (or see if the existing data allows one to meaningfully test the model at all). Furthermore, in the event when no physical model provides a satisfactory description, the phenomenological function could serve as a model itself for a set of transport properties until a better physical model is developed. This approach

could be called a "phenomenological approach" in contrast with the physical model approach, and the two can play a complementary role in the analysis of charge transport.

To find such an "advanced" level of phenomenology that is less general than that defined by the near-equilibrium limit, but still general enough to be widely applicable in the cases of interest, we must identify common features that allow to construct a useful phenomenological framework. For this purpose, both the semiclassical band transport model and a simple fermion hopping model will be reviewed in this chapter. Then, by focusing on the features that result simply from the commonality that fermions mediate charge transport, a phenomenological function that determines three different transport properties – electrical conductivity, the Seebeck coefficient, and the Lorenz number – will be found. The usefulness of this framework will be demonstrated by applying it to a number of material systems in the following chapters. The Seebeck-conductivity relation will prove to be particularly useful for this framework and also provide additional insight in the use or testing of physical models like electron scattering models in band transport.

1.1 Semiclassical band transport

Limitations of the Drude model

The classical Drude model is the most elementary transport model used for describing charge transport in crystals. It states that electrical conductivity σ is proportional to the carrier concentration n:

$$\sigma = \mu_{\mathrm{d}} e n. \tag{1.1}$$

Here, e is the absolute charge of an electron and μ_{d} is referred to as the Drude mobility, or drift mobility. The various shortfalls of the Drude model in its physical description is an elementary topic covered in standard solid state physics textbooks [3]. Nevertheless, it is one of the most widely used models in practice because it works well in many situations; for instance, for describing silicon in conventional transistor devices, the Drude model works sufficiently well [4]. Then, the relevant question is: why does it work at all? Knowing the answer to this question is important in understanding why one has to go further than the Drude model for other types of semiconductors like narrow gap or heavily doped semiconductors.

The reason why the Drude model apparently works in some cases is because of the fortuitous proportionality $\sigma \propto n$ when the Fermi-level is within the band gap and sufficiently far from the band edge. In general, only a part of the free carriers n

near the Fermi surface participates in charge transport due to the Pauli exclusion principle, and thus σ is hardly proportional to n, especially in metals. In low doped semiconductors or insulators (the non-degenerate limit) both n and σ are proportional to the same exponential function of the Fermi-level[1], making $\sigma \propto n$. For this reason, μ_d is simply a proportional coefficient (that happens to be constant with respect to n in the non-degenerate limit), rather than a true mobility (steady-state velocity gained per electric field strength) originally envisioned by the Drude model.

In narrow gap or heavily doped semiconductors, one will usually notice that σ increases sublinearly with n (*i.e.* μ_d decreases with n). This is not necessarily because the mobility is actually decreasing, but is simply an artifact of the Drude equation; even for a fixed (true) mobility that is constant with respect to energy, μ_d will decrease as the Fermi-level gets close or into the band. As soon as a simple exponential function (Boltzmann statistics) can no longer describe the distribution of electrons, the fortuitous proportionality of the Drude model is lost.

Therefore, to describe band transport in the general case where the non-degenerate statistics of fermions is not guaranteed, Fermi-Dirac statistics must be taken into account explicitly. Semiclassical band transport theory is the framework that describes band transport by combining Fermi-Dirac statistics with classical particle kinematics.

In this section, basic semiclassical band transport will be reviewed using the Boltzmann transport equation. Equations derived in this section will be an important basis for extracting the semiclassical phenomenological equations.

The Boltzmann transport equation for charge transport

Near-equilibrium transport phenomena describes the linear response to driving forces that perturb the equilibrium state, the regime in which thermodynamic quantities like temperature are well defined at any local position despite the macroscopic system being in non-equilibrium [5] (detailed discussion in Appendix A). In finding the coefficients that characterize the flux from a given driving force (*e.g.* conductivity characterizes charge flux due to an electric field), the fundamental quantity that needs to be described is the distribution function for the quasiparticle (fermion) being driven. The Boltzmann transport equation states that, in steady state, all

[1] The distribution function for electrons (fermions) reduces to an exponential function in the non-degenerate limit.

processes perturbing the equilibrium must net to zero:

$$\sum \left.\frac{\partial f_{\mathrm{neq}}(\boldsymbol{r},\boldsymbol{k},t)}{\partial t}\right|_{\mathrm{process}} = 0. \tag{1.2}$$

Here, f_{neq} is the particle distribution function at non-equilibrium, $\boldsymbol{r}$ is position, $\boldsymbol{k}$ is the wave vector of the quasiparticle, and t is time. By taking into account time variances in f_{neq} due to diffusion (no-field limit), stationary fields (external forces), and scattering (redistribution of momenta):

$$-\boldsymbol{v}_{\boldsymbol{k}}\frac{\partial f_{\mathrm{neq}}}{\partial \boldsymbol{r}} - \frac{\partial \boldsymbol{k}}{\partial t}\frac{\partial f_{\mathrm{neq}}}{\partial \boldsymbol{k}} + \left.\frac{\partial f_{\mathrm{neq}}}{\partial t}\right|_{\mathrm{scattering}} = 0. \tag{1.3}$$

The first term (position derivative) describes the diffusion of particles, and the second term (momentum derivative) describes external forces exerted on the particle by fields. The negative signs reflect that the distribution function decreases at a particular phase space coordinate $(\boldsymbol{r},\boldsymbol{k})$ due to such events at that coordinate (particles are "removed" from $(\boldsymbol{r},\boldsymbol{k})$ due to diffusion or field effects). The third term describes the scattering events. A specific description for this scattering term is required to solve the Boltzmann transport equation. It is seen that Eq.1.3 governs the particle kinetics under non-equilibrium, by which the particle transport properties are determined.

Relaxation time approximation

For small departures from equilibrium, the scattering process can be described as a Poisson process with a relaxation time τ (*i.e.* rate of $1/\tau$):

$$\left.\frac{\partial f_{\mathrm{neq}}}{\partial t}\right|_{\mathrm{scattering}} = -\frac{f_{\mathrm{neq}} - f_{\mathrm{eq}}}{\tau} = -\frac{f_{\Delta}}{\tau}, \tag{1.4}$$

where f_{eq} is the equilibrium distribution function and f_{Δ} denotes the small linearized departure from equilibrium. It is seen in Eq.1.4 that the relaxation of f_{neq} due to scattering in the absence of field or diffusion effects is proportional to the departure f_{Δ}, a differential equation that yields an exponentially decaying solution towards equilibrium. By using the relaxation time approximation in Eq.1.4, the Boltzmann transport equation Eq.1.3 becomes a solvable form:

$$-\boldsymbol{v}_{\boldsymbol{k}}\frac{\partial(f+f_{\Delta})}{\partial \boldsymbol{r}} - \frac{\partial \boldsymbol{k}}{\partial t}\frac{\partial(f+f_{\Delta})}{\partial \boldsymbol{k}} = \frac{f_{\Delta}}{\tau}. \tag{1.5}$$

Here, f_{eq} has been replaced with the Fermi-Dirac distribution function f for fermions (Fig.1.1a):

$$f_{\mathrm{eq}} = f = \frac{1}{1+\exp\frac{E-E_{\mathrm{F}}}{k_{\mathrm{B}}T}}. \tag{1.6}$$

E_F is the Fermi-level, or electron chemical potential[2].

Electrical Conductivity

Direct current (DC) electrical conductivity σ is the proportional constant for current density $\boldsymbol{J}$ under a stationary electric field $\boldsymbol{E}$ (boldface representing vector quantities), but with no thermal gradients or magnetic fields:

$$\boldsymbol{J} = \sigma \boldsymbol{E}. \tag{1.7}$$

Because σ describes the linear response regime, we are interested in the leading order term in response to the perturbation f_Δ. Higher order terms like the derivatives $\partial f_\Delta / \partial \boldsymbol{r}$ and $\partial f_\Delta / \partial \boldsymbol{k}$ can thus be neglected. Furthermore, the $\partial f / \partial \boldsymbol{r}$ term is also dropped since σ is defined in the limit where there is no temperature gradient. From Eq.1.5, the transport equation relevant for σ becomes

$$-\frac{\partial \boldsymbol{k}}{\partial t}\frac{\partial f}{\partial \boldsymbol{k}} = \frac{f_\Delta}{\tau}. \tag{1.8}$$

Electric field causes $q\boldsymbol{E} = \hbar \partial \boldsymbol{k} / \partial t$ here, where q is the charge of the carrier. Then, the perturbation can be expressed as

$$f_\Delta = -\tau q \frac{1}{\hbar}\frac{\partial f}{\partial \boldsymbol{k}} \cdot \boldsymbol{E} = -\tau q \frac{1}{\hbar}\frac{\partial E}{\partial \boldsymbol{k}}\frac{\partial f}{\partial E} \cdot \boldsymbol{E} = \tau q \left(-\frac{\partial f}{\partial E}\right) \boldsymbol{v_k} \cdot \boldsymbol{E}, \tag{1.9}$$

where E (normal font weight representing scalar quantities) is the energy of the carrier. Now $\boldsymbol{J}$ in Eq.1.7 also needs to be expressed using similar terms. Current density is the flux of charges, and flux is simply the velocity of particles multiplied by the volume density of those particles. Since velocity is dependent on $\boldsymbol{k}$,

$$\boldsymbol{J} = q \int_{\mathrm{BZ}} \boldsymbol{v_k} f_{\mathrm{neq}} = q \int_{\mathrm{BZ}} \boldsymbol{v_k} (f + f_\Delta) = q \int_{\mathrm{BZ}} \boldsymbol{v_k} f_\Delta. \tag{1.10}$$

Here $\int_{\mathrm{BZ}} f_{\mathrm{neq}}$ is an integral over each $\boldsymbol{k}$-state in the Brillouin zone[3] that gives the density of particles. Note that $\int_{\mathrm{BZ}} \boldsymbol{v_k} f = 0$ because at equilibrium there is no flux; only after a perturbation from equilibrium (f_Δ) is when particles are transported. By substituting Eq.1.9 into 1.10 and then comparing to 1.7, the expression for

[2]It is customary to use μ_e (electron chemical potential) interchangeably with E_F (Fermi-level) in the literature. In this usage, E_F is distinguished from "Fermi-energy" which some may use to refer to the 0 K property of a system.

[3]The volume element for integration $\frac{2d^3k}{(2\pi)^3}$ is implied and omitted except for the end results. The factor of 2 is for spin degeneracy, and 2π is the length per $\boldsymbol{k}$ point in each dimension

conductivity is obtained:

$$\begin{aligned}\sigma_{ij} &= e^2 \int_{\mathrm{BZ}} \tau v_{k,i} v_{k,j} \left(-\frac{\partial f}{\partial E}\right) \\ &= \frac{e^2}{4\pi^2} \int_{\mathrm{BZ}} \tau v_{k,i} v_{k,j} \left(-\frac{\partial f}{\partial E}\right) d^3k.\end{aligned} \tag{1.11}$$

Here q was substituted with $\pm e$ (charge for holes and electrons, respectively[4]) and the explicit volume element in k space was given (including the spin degeneracy of two). For the scalar quantity in a particular direction, one could set $i = j = x$. Since $\boldsymbol{k}$ and E are related through a band dispersion relation, Eq.1.11 can also be expressed with an integral over energy space[5]:

$$\sigma_{xx} = e^2 \int \tau(E) v_x^2(E) \left(-\frac{\partial f}{\partial E}\right) g(E) dE, \tag{1.12}$$

where $g(E)$ is the density of states. Here $-\partial f/\partial E$ is a peak function centered around E_{F} (Fig.1.1b) that "samples" contributions from only near the Fermi surface. This feature reflects the mutually exclusive character of fermions that only make the near-Fermi surface relevant for transport.

Seebeck Coefficient

A temperature gradient can also drive electrical current, just like an electric field. In an open circuit where current cannot flow, an electric field develops instead, until the thermal drive is exactly countered. The proportionality between the thermal gradient and electric field in an open circuit condition is the Seebeck coefficient S:

$$S = -\frac{\nabla V}{\nabla T}. \tag{1.13}$$

Here $\nabla V = -\boldsymbol{E}$ is the electric potential gradient[6] in the same direction as the thermal gradient. To derive the semiclassical expression for S, the Boltzmann

[4]Here the convention for hole notation is used where holes are positively charged particles that increase in energy when moving into the valence band away from the band edge. This notation allows to use identical equations for both electrons and holes by just changing the sign of q.

[5]This process of converting $\tau(\boldsymbol{k})$ and $v(\boldsymbol{k})$ to $\tau(E)$ and $v(E)$, respectively, is equivalent to constructing an effective band. Construction of an effective band might be not straightforward with band structure complexity.

[6]Strictly speaking, $\boldsymbol{E}$ here is an observed, measured, or apparent electric field $\boldsymbol{E}^{\mathrm{obs}}$ but not the true electric field. $\boldsymbol{E}^{\mathrm{obs}} = \boldsymbol{E} - \frac{\nabla E_{\mathrm{F}}}{q}$, where ∇E_{F} could be induced by temperature gradients. Therefore, $\boldsymbol{E}^{\mathrm{obs}} = -\nabla V - \frac{\nabla E_{\mathrm{F}}}{q}$. The strict definition for S may be written as $S = \frac{\boldsymbol{E}^{\mathrm{obs}}}{\nabla T} = \frac{-\nabla V - \nabla E_{\mathrm{F}}/q}{\nabla T}$. See Appendix A for the thermodynamic connection. This distinction has no apparent consequences in the transport property expressions derived in this chapter because one can simply substitute $\boldsymbol{E}$ with $\boldsymbol{E}^{\mathrm{obs}}$ and arrive at the same results. $\boldsymbol{E}^{\mathrm{obs}}$ could therefore be considered an effective $\boldsymbol{E}$ in a solid.

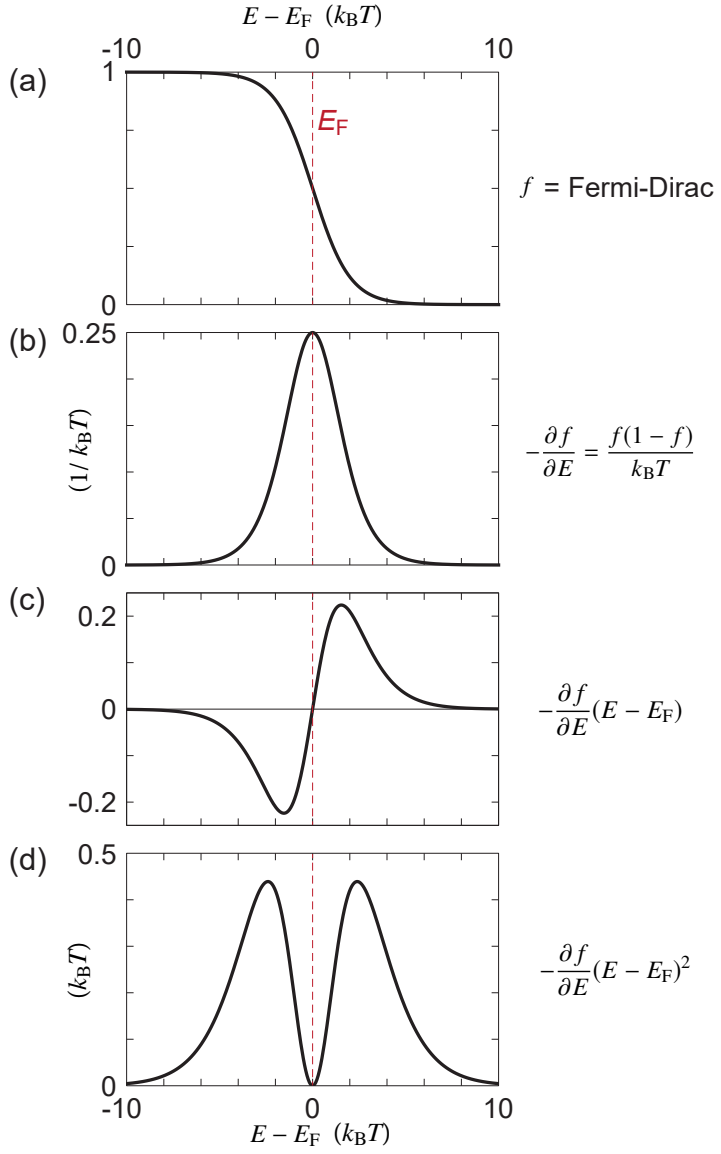

Figure 1.1: Fermi-Dirac distribution function and related "sampling" functions. **(a)** Fermi-Dirac distribution function **(b)** Sampling function relevant for electrical conductivity. Contribution to conduction comes from only near the Fermi-level E_F. **(c)** Sampling function relevant for the Seebeck coefficient. Contribution comes from only near the E_F, but with an opposite sign with respect to E_F. **(d)** Sampling function relevant for the (zero field) electronic thermal conductivity. Contribution comes from both above and below the E_F with the same sign, but is zero at the E_F.

transport equation (Eq.1.5) is used again, but for a thermal driving force ∇T. By dropping the field term and retaining only the first order perturbation terms in Eq.1.5, the Boltzmann transport equation for diffusion becomes

$$-\boldsymbol{v_k}\frac{\partial f}{\partial \boldsymbol{r}} = \frac{f_\Delta}{\tau}. \tag{1.14}$$

Diffusion is caused by the thermal gradient:

$$\frac{\partial f}{\partial r} = \frac{\partial f}{\partial T}\frac{\partial T}{\partial \boldsymbol{r}}. \tag{1.15}$$

By carrying out the derivative $\partial f/\partial T$, it can be rewritten in terms of an energy derivative (one might find it helpful to use the identity shown in Fig.1.1b for this procedure):

$$\frac{\partial f}{\partial T} = \frac{E - E_\mathrm{F}}{T}\left(-\frac{\partial f}{\partial E}\right). \tag{1.16}$$

Then, the thermal perturbation can be expressed as

$$f_\Delta = -\tau\frac{E - E_\mathrm{F}}{T}\left(-\frac{\partial f}{\partial E}\right)\boldsymbol{v_k}\cdot\nabla T. \tag{1.17}$$

The current density due to a thermal gradient can be found by substituting Eq.1.17 into the same equation that we used for a field-driven current (Eq.1.10):

$$\boldsymbol{J} = -q\int_\mathrm{BZ}\tau\boldsymbol{v_k}\boldsymbol{v_k}\frac{E - E_\mathrm{F}}{T}\left(-\frac{\partial f}{\partial E}\right)\nabla T. \tag{1.18}$$

The total current density under both a thermal gradient and electric field can be obtained by adding the electric field contribution (Eq.1.7) to Eq.1.18:

$$\boldsymbol{J} = -q\int_\mathrm{BZ}\tau\boldsymbol{v_k}\boldsymbol{v_k}\frac{E - E_\mathrm{F}}{T}\left(-\frac{\partial f}{\partial E}\right)\nabla T - \sigma\nabla V. \tag{1.19}$$

This process is equivalent to adding two perturbation terms Eqs.1.9 and 1.17 and then substituting into Eq.1.10. By applying the open circuit condition $\boldsymbol{J} = 0$ in Eq.1.19 and comparing to Eq.1.13, the expression for S is found:

$$S_{xx} = \frac{q}{\sigma_{xx}}\int_\mathrm{BZ}\tau v_x v_x\frac{E - E_\mathrm{F}}{T}\left(-\frac{\partial f}{\partial E}\right). \tag{1.20}$$

By writing out the expression for σ and explicitly adding the volume element for integration,

$$S_{xx} = \frac{k_\mathrm{B}}{q}\frac{\int_\mathrm{BZ}\tau v_x v_x\left(\frac{E-E_\mathrm{F}}{k_\mathrm{B}T}\right)\left(-\frac{\partial f}{\partial E}\right)d^3k}{\int_\mathrm{BZ}\tau v_x v_x\left(-\frac{\partial f}{\partial E}\right)d^3k}. \tag{1.21}$$

By changing into an integration in energy space,

$$S_{xx} = \frac{k_B}{q} \frac{\int \tau v_x v_x \left(\frac{E-E_F}{k_B T}\right) \left(-\frac{\partial f}{\partial E}\right) g(E) dE}{\int \tau v_x v_x \left(-\frac{\partial f}{\partial E}\right) g(E) dE}. \tag{1.22}$$

Notice that q determines the sign of the Seebeck coefficient. k_B/e is 86.17 μV/K, the natural unit for thermopower[7]. It is also found in the numerator that the "sampling" at E_F comes with a weighting factor $\frac{E-E_F}{k_B T}$ (plotted in Fig.1.1c), that makes it an odd function with respect to E_F. This asymmetry is because moving a particle with more energy than the chemical potential contributes to positive heat or energy flow, whereas moving a particle with less actually contributes to negative heat or energy flow (recall that chemical potential is an indicator for particle energy of the system – *i.e.* the partial molar Gibbs free energy).

Lorenz Number

A flow of charges is also a flow of heat. In fact, the heat transported by charge carriers can be orders of magnitude larger than that from phonons in highly conductive metals. The proportionality between electrical conductivity and its contribution to thermal conductivity is characterized by the Lorenz number L:

$$L = \frac{\kappa_e}{\sigma T}, \tag{1.23}$$

where κ_e is the electronic contribution to thermal conductivity[8]. This equation is referred to as the Wiedemann–Franz law, and L for a classical metal is $\frac{\pi^2}{3}\left(\frac{k_B}{e}\right)^2$. In general, L is dependent on the kinetic transport parameters and also E_F just like the Seebeck coefficient, which will be shown in this subsection.

Heat flux[9] $\boldsymbol{U}$ due to charge carriers can be expressed in a fashion similar to current density in Eq.1.10, but by tracking energy instead of charge:

$$\boldsymbol{U} = \int_{BZ} \boldsymbol{v_k} (E_{\boldsymbol{k}} - E_F) f_\Delta. \tag{1.24}$$

[7]The term thermopower will be used to refer to the magnitude of the Seebeck coefficient $|S|$. The term "absolute Seebeck coefficient" is avoided because, in a metrology context, it often refers to simply S, but not $|S|$, in the sense that a measured S^{meas} ("relative" Seebeck coefficient) must be converted to an "absolute" Seebeck coefficient by subtracting the S of the probe wires.

[8]When there are two different type of carriers (*e.g.* electrons and holes), there is an additional electronic contribution due to bipolar diffusion. In the notation used here, we do not include the bipolar term in κ_e. This bipolar term is discussed and derived in sections 6.4 and 6.5, respectively.

[9]The heat flux definition here is *not* a unique definition. For example, Ref.[5] uses an alternative definition and explains the freedom to include other terms like particle flux carrying their chemical potentials in heat flux (Eq.A.6). All definitions arrive at same descriptions about the physical phenomena.

Note that q was replaced with energy. Here $E_{\boldsymbol{k}} - E_{\mathrm{F}}$ was placed instead of $E_{\boldsymbol{k}}$, because replacing a carrier at the electron chemical potential (which is the Fermi-level E_{F}) with a carrier with energy above and below E_{F} makes that system warmer and cooler, respectively; in other words, the indicator or reference of the electron energy is the electron chemical potential. The perturbation term can be found by adding together the electric field term Eq.1.9 and the thermal gradient term Eq.1.17, which gives

$$f_{\Delta} = \tau q \left(-\frac{\partial f}{\partial E}\right) \boldsymbol{v_k} \cdot \boldsymbol{E} - \tau \frac{E - E_{\mathrm{F}}}{T} \left(-\frac{\partial f}{\partial E}\right) \boldsymbol{v_k} \cdot \nabla T. \tag{1.25}$$

By substituting f_{Δ} into Eq.1.24, one can obtain

$$\boldsymbol{U} = TS\sigma \boldsymbol{E} - \kappa_0 \nabla T, \tag{1.26}$$

where we have used the result for S obtained in the previous section for writing the coefficient for $\boldsymbol{E}$ as $TS\sigma$ here[10], and κ_0 is

$$\kappa_0 = \frac{1}{4\pi^3} \int_{\mathrm{BZ}} \tau \boldsymbol{v_k} \boldsymbol{v_k} \frac{(E - E_{\mathrm{F}})^2}{T} \left(-\frac{\partial f}{\partial E}\right) d^3k. \tag{1.27}$$

Note that both $S\sigma$ and κ_0 are tensors in general, indicated by the $\boldsymbol{v_k} \boldsymbol{v_k}$ term.

κ_0 is *not* the conventionally used thermal conductivity; it is a thermal conductivity for zero field (see footnote 6 for the precise condition of zero field). The conventionally used thermal conductivity measured in the lab is under *zero current* conditions. To find this condition, we rewrite the current density driven by both ∇T and $\boldsymbol{E}$ (Eq.1.19) using S and σ previously derived:

$$\boldsymbol{J} = -S\sigma \nabla T + \sigma \boldsymbol{E}. \tag{1.28}$$

It is seen that the zero current condition is equivalent to $\boldsymbol{E} = S\nabla T$, which is just the condition that defines the Seebeck coefficient. By substituting this relation into Eq.1.26, $\boldsymbol{U}|_{\boldsymbol{J}=0} = -(-TS^2\sigma + \kappa_0)\nabla T$ which yields the thermal conductivity by charge carriers:

$$\kappa_{\mathrm{e}} = \kappa_0 - TS^2\sigma. \tag{1.29}$$

The Lorenz number follows by using Eq.1.23 with this result:

$$L = \frac{\kappa_0}{\sigma T} - S^2. \tag{1.30}$$

[10]This relation is not a simple coincidence, but from an identity originating from time-reversal symmetry. Onsager reciprocity is discussed in Appendix A.

By writing out the full expression:

$$L = \left(\frac{k_B}{e}\right)^2 \frac{\int_{BZ} \tau \boldsymbol{v_k} \boldsymbol{v_k} \left(\frac{E-E_F}{k_B T}\right)^2 \left(-\frac{\partial f}{\partial E}\right) d^3k}{\int_{BZ} \tau \boldsymbol{v_k} \boldsymbol{v_k} \left(-\frac{\partial f}{\partial E}\right) d^3k} - S^2,$$

$$L = \left(\frac{k_B}{e}\right)^2 \left[\frac{\int_{BZ} \tau \boldsymbol{v_k} \boldsymbol{v_k} \left(\frac{E}{k_B T}\right)^2 \left(-\frac{\partial f}{\partial E}\right) d^3k}{\int_{BZ} \tau \boldsymbol{v_k} \boldsymbol{v_k} \left(-\frac{\partial f}{\partial E}\right) d^3k} - \left(\frac{\int_{BZ} \tau \boldsymbol{v_k} \boldsymbol{v_k} \left(\frac{E}{k_B T}\right) \left(-\frac{\partial f}{\partial E}\right) d^3k}{\int_{BZ} \tau \boldsymbol{v_k} \boldsymbol{v_k} \left(-\frac{\partial f}{\partial E}\right) d^3k}\right)^2\right]. \tag{1.31}$$

It is seen that natural unit for L is $\left(\frac{k_B}{e}\right)^2$. Also note the sampling function in the numerator of the first term, which is plotted in Fig.1.1d. Other than the sampling function and constants, the expression constitutes the same terms that described both conductivity and the Seebeck coefficient. This common structure will play a key role in formulating the semiclassical phenomenology later in section 1.3.

Hall Coefficient

The Hall coefficient is a measured property classically related to the sign and concentration of charge carriers. For a magnetic $\boldsymbol{B}$ field along the z-axis and an electric field driving current along the x-axis, an electric field is developed along the y-axis due to the Lorentz force acting on the carriers. The Hall coefficient R_H is defined from the measurement of this field developed along y:

$$R_H = \frac{E_y}{B_z J_x}. \tag{1.32}$$

This definition also defines the Hall carrier concentration $n_H = \frac{1}{qR_H}$, which derives from the Drude model for the Hall effect[11].

Although the Hall coefficient will not be a primary means for analyzing transport in this thesis, it is important to see how the usefulness of the Hall effect is different than that of conductivity or the Seebeck coefficient. Here the semiclassical expression for the Hall coefficient will be derived to show that, in addition to the kinetic parameters τ and v, introduction of an effective mass is necessary to describe the R_H.

The simultaneous application of electric and magnetic fields can be taken into account by

$$\frac{\partial \boldsymbol{k}}{\partial t} = \frac{q}{\hbar}(\boldsymbol{E} + \boldsymbol{v} \times \boldsymbol{B}). \tag{1.33}$$

[11]Hall carrier concentration n_H is only equal to the actual carrier concentration n under special conditions. Therefore n_H should be considered as a type of measurement. A Hall factor r_H is conventionally defined to account for the difference: $n = n_H r_H$.

If one attempts to find f_Δ by substituting this equation into Eq.1.8 as was done for electrical conductivity, one would notice that the perturbation due to the magnetic field becomes zero:

$$(f_\Delta)_{\boldsymbol{B},\text{leading order}} = \tau q(\boldsymbol{v}\times\boldsymbol{B})\cdot\boldsymbol{v}\left(-\frac{\partial f}{\partial E}\right) = 0 \tag{1.34}$$

This result indicates that the next order term must be considered for describing the response to a magnetic field. From Eq.1.5, the equivalent to Eq.1.8 that is relevant for $\boldsymbol{E}$ and $\boldsymbol{B}$ fields is found by including the next order term for the $\boldsymbol{B}$ field:

$$-\left(\frac{\partial \boldsymbol{k}}{\partial t}\frac{\partial f}{\partial \boldsymbol{k}}\right)_{\boldsymbol{E}-\text{field}} - \left(\frac{\partial \boldsymbol{k}}{\partial t}\frac{\partial f_\Delta}{\partial \boldsymbol{k}}\right)_{\boldsymbol{B}-\text{field}} = \frac{f_\Delta}{\tau}. \tag{1.35}$$

By using $\frac{\partial \boldsymbol{k}}{\partial t} = \frac{q}{\hbar}\boldsymbol{E}$ for the $\boldsymbol{E}$-field and $\frac{\partial \boldsymbol{k}}{\partial t} = \frac{q}{\hbar}(\boldsymbol{v}\times\boldsymbol{B})$ in Eq.1.35, the equation for the perturbation term can be obtained:

$$q\boldsymbol{E}\cdot\boldsymbol{v}\left(-\frac{\partial f}{\partial E}\right) = \left(\frac{1}{\tau} + q(\boldsymbol{v}\times\boldsymbol{B})\frac{\partial \boldsymbol{v}}{\hbar\partial \boldsymbol{k}}\frac{\partial}{\partial \boldsymbol{v}}\right) f_\Delta. \tag{1.36}$$

Notice that, contained in the magnetic perturbation term is

$$\frac{\partial \boldsymbol{v}}{\hbar\partial \boldsymbol{k}} = \left[m_\text{b}^{*-1}\right]_{ij}, \tag{1.37}$$

where m_b^* is the band effective mass. Subscripts ij indicate that the quantity is a second rank tensor.

The involvement of the band effective mass in Eq.1.36 is what distinguishes a measurement involving a magnetic field from others like conductivity, the Seebeck coefficient, or the Lorenz number. On one hand, the magnetic field allows one to extract more information from the material – information related to the band structure that governs the quasiparticle transport. On the other hand, the information extracted from a magnetic measurement is only relevant for σ, S, or L when there is a good physical understanding about how quantities like m_b^* or R_H should be interpreted. Therefore, for developing a phenomenological framework to tackle some of the more general cases, measurements under a magnetic field is less useful; it is just one more measurement and one more unknown at the same time. In the case where a material of interest turns out to be a conventional band conductor, magnetic measurements become an extremely useful tool to further advance the understanding of the band structure underlying transport properties.

For completeness, derivation of the Hall coefficient will be continued. Readers mostly interested in the development of the semiclassical phenomenology are encouraged to move on to the next section.

To simplify the problem, here it will be assumed that the μ_b is a scalar quantity (isotropic case). Then, f_Δ, the solution to Eq.1.36 is needed, which is obtained[12] as

$$f_\Delta = q\tau\left(-\frac{\partial f}{\partial E}\right)\boldsymbol{v}\cdot\frac{\boldsymbol{E}+(\mu_\mathrm{b}\boldsymbol{B}\cdot\boldsymbol{E})\mu_\mathrm{b}\boldsymbol{B}+\mu_\mathrm{b}\boldsymbol{B}\times\boldsymbol{E}}{1+(\mu_\mathrm{b}B)^2}. \tag{1.38}$$

Here, μ_b was defined as

$$\mu_\mathrm{b} = \frac{q\tau}{m_\mathrm{b}^*}. \tag{1.39}$$

It is seen that the sensitivity to the magnetic field is governed by the dimensionless quantity $\mu_\mathrm{b}B$ (containing a sign). The current density under the influence of general electric and magnetic fields can be obtained by substituting Eq.1.38 into Eq.1.10. For the Hall coefficient, the magnetic field is only along the z-direction (B_z) perpendicular to the electric field. In this situation, f_Δ in Eq.1.38 simplifies to an expression with only x and y components:

$$f_\Delta^{B_z} = q\tau\left(-\frac{\partial f}{\partial E}\right)\frac{1}{1+(\mu_\mathrm{b}B)^2}\boldsymbol{v}\cdot\begin{pmatrix}1 & \mu_\mathrm{b}B_z\\ -\mu_\mathrm{b}B_z & 1\end{pmatrix}\boldsymbol{E}, \tag{1.40}$$

where $\boldsymbol{v}$ and $\boldsymbol{E}$ here only have x and y components. By substituting Eq.1.40 into Eq.1.10, the current density can be obtained. It is convenient to show the result in the matrix form of a magnetoconductivity tensor:

$$\sigma(B_z) = \begin{pmatrix}\sigma_{xx} & \sigma_{xy}\\ \sigma_{yx} & \sigma_{yy}\end{pmatrix} = \begin{pmatrix}\sigma_{xx} & -\sigma_{yx}\\ \sigma_{yx} & \sigma_{xx}\end{pmatrix}, \tag{1.41}$$

where

$$\sigma_{xx} = \frac{q^2}{4\pi^3}\int_\mathrm{BZ}\frac{\tau\frac{v^2}{3}\left(-\frac{\partial f}{\partial E}\right)}{1+(\mu_\mathrm{b}B_z)^2}d^3k, \tag{1.42}$$

$$\sigma_{yx} = -\frac{q^2B_z}{4\pi^3}\int_\mathrm{BZ}\frac{\tau\frac{v^2}{3}\left(-\frac{\partial f}{\partial E}\right)\mu_\mathrm{b}}{1+(\mu_\mathrm{b}B_z)^2}d^3k. \tag{1.43}$$

Here, $v_x^2 = v_xv_y = v^2/3$ was used since an isotropic case was already assumed. Note that μ_b is inside the integral because it is dependent on k; τ and (and in some cases also μ_b) are k-dependent.

[12] Solving is similar to a first order differential equation, where the solution would be of a form $a\boldsymbol{v}+b$. Instead of a being a scalar constant, it should be a vector that is independent of $\boldsymbol{v}$. Substitution shows that b must be zero because all the remaining terms contain $\boldsymbol{v}$. Therefore $f_\Delta = \boldsymbol{a}\cdot\boldsymbol{v}$. Then, it can be noticed that all the directional degrees of freedom possible in the equation is covered by a linear combination of $\boldsymbol{B}$, $\boldsymbol{E}$, and $\boldsymbol{B}\times\boldsymbol{E}$ in $\boldsymbol{a}$. With three unknown coefficients, the solution can be found.

The Hall effect is measured using weak magnetic fields where $(\mu_\mathrm{b} B_z)^2 \ll 1$, which simplifies σ_{xx} in Eq.1.42 to just that identical to normal conductivity σ. σ_{yx} simplifies to

$$\sigma_{yx} = -\frac{q^3 B_z}{4\pi^3} \int_\mathrm{BZ} \tau^2 \frac{v^2}{3m_\mathrm{b}^*} \left(-\frac{\partial f}{\partial E}\right) d^3k. \tag{1.44}$$

The Hall coefficient is equivalent to

$$R_\mathrm{H} = \frac{\rho_{yx}}{B_z}, \tag{1.45}$$

where ρ_{yx} is a component of the magnetoresistivity tensor, for which the magneto-conductivity tensor must be inverted:

$$\rho_{yx} = \frac{-\sigma_{yx}}{\sigma^2 + \sigma_{yx}^2}. \tag{1.46}$$

When $(\sigma_{yx}/\sigma)^2 \ll 1$ is satisfied, which is usually the case because the condition is approximately same as the weak field condition ($(\mu_\mathrm{b} B_z)^2 \ll 1$), the relation simplifies to $\rho_{yx} = -\sigma_{yx}/\sigma^2$. Therefore, R_H in the weak magnetic field limit finally becomes

$$R_\mathrm{H} = \frac{q}{\sigma} \frac{\int_\mathrm{BZ} \frac{\tau^2}{m_\mathrm{b}^*} v^2 \left(-\frac{\partial f}{\partial E}\right) d^3k}{\int_\mathrm{BZ} \tau v^2 \left(-\frac{\partial f}{\partial E}\right) d^3k}. \tag{1.47}$$

It is seen that, R_H depends on the sign of q. Also notice that, by assuming a Drude model where τ/m_b^* is k-independent, $\sigma = ne^2\tau/m^*$, and $m_\mathrm{b}^* = m^*$, Eq.1.47 reduces to $R_\mathrm{H} = \frac{1}{nq}$ as originally envisioned by the Drude model.

Transport properties with scattering models

In the previous sections, transport properties were derived using general kinematic parameters such as τ or v placed inside integrals over $\boldsymbol{k}$ or E. To actually calculate the integrals, the $\boldsymbol{k}$ or E dependencies must be specified. That of velocity v can be specified by referring to the band structure because it represents the group velocity of Bloch waves. τ, on the other hand, requires a specific physical model for scattering. Here, some typical scattering models will be used to find the corresponding transport property expressions. This exercise will help identifying a generally useful form for a phenomenological transport function in section 1.3.

In this section, an isotropic free electron dispersion relation $E = \frac{\hbar^2 k^2}{2m_\mathrm{b}^*}$ will be used (E is 0 at the band edge), while also allowing for valley degeneracy (multiple bands that are identical by symmetry). In a semiconductor, the free electron term is the leading order term for the dispersion relation at the band edge, providing the most

Table 1.1: Parameters in $\tau = \tau_0(T) \cdot \left(\frac{E}{k_B T}\right)^r$ for various scattering mechanisms. The exponent r is the leading order term for the energy dependency.

Scattering source	**Scattering parameter**, r	$\tau_0(T)$
Point defects	$-\frac{1}{2}$	$\propto T^r$
Acoustic or non-polar optical phonons (deformation potential)	$-\frac{1}{2}$	$\propto T^{-1+r}$
Polar optical or piezoacoustic phonons	$\frac{1}{2}$	$\propto T^{-1+r}$
Ionized impurities	$\frac{3}{2}$	$\propto T^r$

efficient means of describing transport; transport is governed only within an energy range of a few $k_B T$ from the band edge. Extensions to anisotropic cases can be done by considering different m_b^*'s in each direction, although it is not done here for simplicity.

A common structure found in the expression for τ in various scattering models is a power dependency on the carrier energy (or, one could understand it as a leading order dependency on energy). Considering this commonality, the relaxation time (inverse of scattering rate) can be expressed in a general form such as

$$\tau = \tau_0(T) \cdot \left(\frac{E}{k_B T}\right)^r . \tag{1.48}$$

Here, τ_0 is temperature dependent but energy independent, and a reduced energy $E/k_B T$ scale is used because it becomes a convenient scale for calculating the transport properties. Table 1.1 summarizes the parameters corresponding to various scattering mechanisms, including the energy dependency (scattering parameter r) needed to calculate the integrals for transport properties. For details including the model description of τ_0 in each scattering mechanism given in terms of microscopic physical parameters, see the following: Refs.[6–10].

Using the general form in Eq.1.48, transport properties can be calculated using Eqs.1.11, 1.21, and 1.31. Each integral over the Brillouin zone should multiplied by valley degeneracy N_V; *i.e.* $\frac{1}{4\pi^2}\int_{BZ} d^3k$ converts to $N_V \int_0^\infty g_b(E)dE$ where the density of states of each band is $g_b(E) = \frac{4\pi}{h^3}(2m_b^*)^{3/2}E^{1/2}$. v_x^2 can be replaced with $v^2/3$ (isotropy). Then, by changing variables to reduced energy ($\epsilon = E/k_B T$) and taking care of the Fermi derivative using integration by parts, conductivity becomes

$$\sigma = \frac{8\pi}{3}\frac{e^2 \tau_0 N_V}{h^3 m_b^*}(2k_B T m_b^*)^{\frac{3}{2}} \cdot \left(r + \frac{3}{2}\right) F_{r+\frac{1}{2}}(\eta). \tag{1.49}$$

Here, the reduced Fermi-level η,

$$\eta = \frac{E_{\mathrm{F}}}{k_{\mathrm{B}}T}, \tag{1.50}$$

and (non-normalized) complete Fermi-Dirac integral,

$$F_i(\eta) = \int_0^\infty \frac{\epsilon^i}{e^{\epsilon-\eta}+1} d\epsilon, \tag{1.51}$$

were defined. Mobility parameter μ_0 is commonly used, defined as

$$\mu_0 = \frac{e\tau_0}{m_{\mathrm{b}}^*}. \tag{1.52}$$

A weighted mobility μ_{w} is then defined:

$$\mu_{\mathrm{w}} = \mu_0 N_{\mathrm{V}} \left(\frac{m_{\mathrm{b}}^*}{m_{\mathrm{e}}}\right)^{\frac{3}{2}}, \tag{1.53}$$

where m_{e} is the mass of an electron. Eq.1.49 can then be recast:

$$\sigma = \frac{8\pi e(2m_{\mathrm{e}}k_{\mathrm{B}}T)^{\frac{3}{2}}}{3h^3}\mu_{\mathrm{w}} \cdot \left(r+\frac{3}{2}\right) F_{r+\frac{1}{2}}(\eta). \tag{1.54}$$

It is seen that the magnitude of conductivity is proportional to weighted mobility for a given η and T.

An analogous procedure for the Seebeck coefficient yields

$$S = \left(\frac{k_{\mathrm{B}}}{q}\right)\left[-\eta + \frac{\left(r+\frac{5}{2}\right)F_{r+\frac{3}{2}}(\eta)}{\left(r+\frac{3}{2}\right)F_{r+\frac{1}{2}}(\eta)}\right]. \tag{1.55}$$

It is seen that S is a function of only η, independent of μ_w.

The Lorenz number is calculated as

$$L = \left(\frac{k_{\mathrm{B}}}{q}\right)^2\left[\frac{\left(r+\frac{7}{2}\right)F_{r+\frac{5}{2}}(\eta)}{\left(r+\frac{3}{2}\right)F_{r+\frac{1}{2}}(\eta)} - \left(\frac{\left(r+\frac{5}{2}\right)F_{r+\frac{3}{2}}(\eta)}{\left(r+\frac{3}{2}\right)F_{r+\frac{1}{2}}(\eta)}\right)^2\right]. \tag{1.56}$$

It is seen that L is also a function of only η, independent of μ_w.

The Hall coefficient can be calculated using Eq.1.47:

$$R_{\mathrm{H}} = \frac{3h^3}{8\pi q(2m_{\mathrm{e}}k_{\mathrm{B}}T)^{\frac{3}{2}}}\frac{1}{N_{\mathrm{V}}\left(\frac{m_{\mathrm{b}}^*}{m_{\mathrm{e}}}\right)^{\frac{3}{2}}}\frac{\left(2r+\frac{3}{2}\right)F_{2r+\frac{1}{2}}(\eta)}{\left[\left(r+\frac{3}{2}\right)F_{r+\frac{1}{2}}(\eta)\right]^2}, \tag{1.57}$$

which shows that R_H is sensitive to $N_V \left(\frac{m_b^*}{m_e}\right)^{\frac{3}{2}}$. When valley degeneracy is not explicitly considered, $N_V \left(\frac{m_b^*}{m_e}\right)^{\frac{3}{2}}$ is sometimes simply expressed as $\left(\frac{m_H^*}{m_e}\right)^{\frac{3}{2}}$, where $m_H^* = N_V^{2/3} m_b^*$ is another type of an effective mass[13]. The Hall factor $r_H = n/n_H = qnR_H$ can be calculated using the expression for n:

$$n = \int g(E) f \, dE. \tag{1.58}$$

Calculation yields

$$r_H = \frac{3}{2} \frac{\left(2r + \frac{3}{2}\right) F_{2r+\frac{1}{2}}(\eta)}{\left[\left(r + \frac{3}{2}\right) F_{r+\frac{1}{2}}(\eta)\right]^2}. \tag{1.59}$$

It is seen that r_H is also a function of only η.

Drude mobility can be calculated from the definition Eq.1.1:

$$\mu_d = \frac{2}{3} \frac{e\tau_0}{m_b^*} \cdot \frac{\left(r + \frac{3}{2}\right) F_{r+\frac{1}{2}}(\eta)}{F_{\frac{1}{2}}(\eta)}. \tag{1.60}$$

It is customary in the literature to use the temperature dependency of μ_d or μ_H to distinguish scattering mechanisms. These temperature dependencies and their pitfalls will be discussed in Ch.4 (section 4.1).

Up to here, the essential parts of the semiclassical band transport theory needed for developing the semiclassical phenomenological transport formalism has been reviewed. For more details related to the Boltzmann transport equation, the following textbooks can be consulted: Refs.[6, 7, 11, 12].

1.2 Nearest neighbor hopping

One of the simplest hopping models for conduction is nearest neighbor hopping, which is similar to the atomic diffusion model with atoms diffusing through nearest neighbor sites but for fermionic quasiparticles (charge carriers) instead of atoms. In this section, the hopping model given by Cutler and Mott [13] is derived. This model will be used to help notice some general features by comparing to the semiclassical band transport model in the next section.

[13] The Hall effective mass m_H^* in this context is sometimes interpreted as a density-of-states mass (m_{DOS}^*) due to its connection to Hall carrier concentration. However, as seen from Eq.1.47, the Hall coefficient is a weighted measure of τ/m^* rather than m^* alone, and thus does not simply reflect only the density of states. In this thesis, m_{DOS}^* is reserved for the quantity that yields the true density of states at energy E through the relation $g(E) = \frac{4\pi}{h^3}(2m_{DOS}^*)^{3/2}E^{1/2}$.

Consider two localized states 1 and 2 of identical energy, both with a spatial density of N, separated by average distance L. For a characteristic hopping time τ, the current density from this hopping motion is $q\frac{L}{\tau}N$ multiplied by the probability of the hopping action to happen. For the hopping to occur from state 1 to 2, state 1 must be occupied (noted f_1 using the distribution function) and state 2 must be unoccupied $(1-f_2)$, which results in a probability of $f_1(1-f_2)$. The presence of an electric field changes these hopping rates. For a charge q hopping along the direction of an E_x field, potential energy gain due to the hopping is $qE_xL/2$, which gives modulation to the hopping rate by a factor of $\exp\left(\frac{qE_xL}{2k_BT}\right)$ assuming an exponential dependency on energy for the hopping rate. After subtracting the hoping in the backwards direction calculated in the same manner, the total current density from the 1 to 2 hopping is

$$J_{12} = \frac{qLN}{\tau}\left[f_1(1-f_2)\exp\left(\frac{qE_xL}{2k_BT}\right) - f_2(1-f_1)\exp\left(\frac{-qE_xL}{2k_BT}\right)\right]. \tag{1.61}$$

The leading order terms for E_x and $\frac{dT}{dx}$ must be found from this equation to find conductivity and the Seebeck coefficient. The expansion of f_1 and f_2 are

$$\begin{aligned} f_1 &= f - \frac{dT}{dx}\frac{df}{dT}\frac{L}{2} + \dots \\ f_2 &= f + \frac{dT}{dx}\frac{df}{dT}\frac{L}{2} + \dots, \end{aligned} \tag{1.62}$$

where f is the average distribution between the two states. Then, the 0^{th} order term with respect to E/T in J_{12} is found by replacing the exponential terms with 1, giving

$$J_{12}^{0^{\text{th}}} = -\frac{qL^2N}{\tau}\frac{dT}{dx}\frac{df}{dT} = -\frac{qL^2N}{\tau}\frac{E-E_F}{T}\left(-\frac{\partial f}{\partial E}\right)\frac{dT}{dx}, \tag{1.63}$$

where the equality Eq.1.16 was used. The 1^{st} order term with respect to E/T is then found by replacing the e^x with x:

$$J_{12}^{1^{\text{st}}} = \frac{q^2L^2N}{\tau K_BT}E_xf(1-f) = \frac{q^2L^2N}{\tau}\left(-\frac{\partial f}{\partial E}\right)E_x, \tag{1.64}$$

where the equality in Fig.1.1b was used. Eqs.1.63 and 1.64 are the leading order terms for the driving forces $\frac{dT}{dx}$ and E_x, respectively, which could be added to write the expression for J_{12} in the linear response regime:

$$J_{12} = q^2ND\left(-\frac{\partial f}{\partial E}\right)E_x - qND\frac{E-E_F}{T}\left(-\frac{\partial f}{\partial E}\right)\frac{dT}{dx}, \tag{1.65}$$

where $D = \frac{L^2}{\tau}$ was defined as diffusivity. Next, to take into account states with other energies, N can be replaced with $\int g(E)$. The final result for current density due to

nearest neighbor hopping is

$$J = q^2 \int D(E)g(E)\left(-\frac{\partial f}{\partial E}\right)dE \cdot E_x - q\int D(E)g(E)\frac{E-E_\mathrm{F}}{T}\left(-\frac{\partial f}{\partial E}\right)dE \cdot \frac{dT}{dx}. \tag{1.66}$$

Here, conductivity and the Seebeck coefficient is found (compare to Eq.1.28):

$$\sigma = q^2 \int D(E)g(E)\left(-\frac{\partial f}{\partial E}\right)dE, \tag{1.67}$$

and,

$$S = \frac{k_\mathrm{B}}{q}\frac{\int D(E)g(E)\frac{E-E_\mathrm{F}}{k_\mathrm{B}T}\left(-\frac{\partial f}{\partial E}\right)dE}{\int D(E)g(E)\left(-\frac{\partial f}{\partial E}\right)dE}. \tag{1.68}$$

Despite completely different physical meanings in the parameters and mechanistic description used compared with the band conduction case, obvious similarities are found when the end results are compared: see Eqs.1.9 and 1.22.

1.3 Semiclassical phenomenology of transport

Transport models described in the previous sections (band transport model in 1.1 and hopping transport model in 1.2) are physical models that describe the microscopic physical processes that underly the macroscopic transport phenomena. By contrast, phenomenological models do not describe the microscopic physical processes, but are more general because they are based on principles independent of the microscopic process. For example, the equation defining conductivity, $\boldsymbol{J} = \sigma\boldsymbol{E}$, is also a phenomenological model. It predicts a quantity σ based on near-equilibrium thermodynamics, but does not specify how microscopic processes actually constitute σ; it only specifies that $\boldsymbol{J}$ is proportional to $\boldsymbol{E}$ under certain thermodynamic conditions. Obviously, phenomenological models play a different role than physical models. Phenomenological models allow one to assess experimental results on more general grounds, especially when the microscopic processes are not understood very well. They also help to compare different physical models. For example, it is much easier to compare σ of a band conduction model with that of a hopping model, rather than to compare the descriptions for $\boldsymbol{J}$. In this section, the objective is to establish a phenomenological model that is more specific than the thermodynamic phenomenology, but still general enough to be widely applicable to charge transport phenomena.

Phenomenological models are built around a common and general feature. The feature that is common for any case described by linearized transport equations is that

a local equilibrium is well defined at an arbitrary infinitesimal region of the system. For electronic charge transport, a common and important feature that is applicable to a wide variety of experiments is that the charge carrier is a fermion that behaves according to the Fermi-Dirac distribution function. This feature is equivalent to the charge carrier being a non-interacting fermion, which is an assumption underlying band theory and many other theories for electronic phenomena. Even when electron-electron interactions are present, they are often described using terms relevant for non-interacting fermions (*e.g.* DFT+U theory for effective bands) because of the difficulty of describing electronic properties with a many-body framework. Therefore, phenomenology relevant for fermion charge carriers and the Fermi-Dirac distribution function should be widely applicable. The phenomenology established in such a manner will be referred to as "semiclassical phenomenology," where the fermion nature is considered in addition to the classical (irreversible) thermodynamic equations (analogous to how semiclassical band transport is termed).

Extracting semiclassical phenomenology from physical models

From the previously derived band and hopping transport models, one can notice that the common feature related to the Fermi-Dirac distribution function is the presence of a $-\frac{\partial f}{\partial E}$ term in conductivity (Eqs.1.12 and 1.67), which we referred to as the sampling function for conductivity (Fig.1.1b). The identity $-\frac{\partial f}{\partial E} = \frac{f(1-f)}{k_\mathrm{B}T}$ offers an easy interpretation of its physical origin: the exclusive fermion nature that needs an empty state $(1-f)$ for a particle in an occupied fermion state (f) to be transported. Similarly, the common feature in the Seebeck coefficient was $\frac{E-E_\mathrm{F}}{T}\left(-\frac{\partial f}{\partial E}\right)$ (Eqs.1.22 and 1.68), which could be thought of as a modified sampling function (Fig.1.1c). Physically, this feature is associated with the need to quantify the heat transported by a carrier $(E-E_\mathrm{F})$, as opposed to the need to simply count the number of charges.

Based on these sampling functions that result from the general property of fermion transport, it is possible to abstract a phenomenological function that governs transport. From the conductivity equation (Eqs.1.12 or 1.67), by grouping all of the parameters, expect for the sampling function, into $\sigma_E(E)$, we obtain

$$\sigma = \int \sigma_E(E)\left(-\frac{\partial f}{\partial E}\right)dE. \tag{1.69}$$

Through an analogous process for the Seebeck coefficient, we obtain

$$S = \left(\frac{k_\mathrm{B}}{q}\right)\frac{\int \sigma_E(E)\left(\frac{E-E_\mathrm{F}}{k_\mathrm{B}T}\right)\left(-\frac{df}{dE}\right)dE}{\int \sigma_E(E)\left(-\frac{\partial f}{\partial E}\right)dE}. \tag{1.70}$$

One can notice that $\sigma_E(E)$ is self-consistent within each model (band or hopping), but different in terms of physical meaning. For band transport:

$$\sigma_E(E) = q^2\tau(E)v_x^2(E)g(E), \tag{1.71}$$

where τ and v_x are for Bloch waves. For hopping transport,

$$\sigma_E(E) = q^2D(E)g(E), \tag{1.72}$$

where D is for localized carriers. We name this phenomenological function $\sigma_E(E)$ the "transport function[14]" because it is a function that determines each of the transport properties.

The Lorenz number can also be described self-consistently (within a particular model like band transport). The phenomenological equation for Lorenz number becomes

$$L = \left(\frac{k_\mathrm{B}}{e}\right)^2 \left[\frac{\int \sigma_E(E)\left(\frac{E}{k_\mathrm{B}T}\right)^2\left(-\frac{df}{dE}\right)dE}{\int \sigma_E(E)\left(-\frac{\partial f}{\partial E}\right)dE} - \left(\frac{\int \sigma_E(E)\left(\frac{E}{k_\mathrm{B}T}\right)\left(-\frac{df}{dE}\right)dE}{\int \sigma_E(E)\left(-\frac{\partial f}{\partial E}\right)dE}\right)^2\right]. \tag{1.73}$$

It has been seen that, with a phenomenological $\sigma_E(E)$, transport properties σ, S, and L are determined. On the other hand, R_H is *not* determined by $\sigma_E(E)$. By considering Eq.1.47, we find

$$R_\mathrm{H} = \frac{q}{\sigma^2}\int \left(\frac{\tau}{m_\mathrm{I}^*}\right)\sigma_E(E)\left(-\frac{\partial f}{\partial E}\right)dE, \tag{1.74}$$

where m_I^* is the inertial mass from changing the integral to energy space (multiple bands will result in an inertial effective mass that is smaller than the band effective mass of each band). One could alternatively write an expression for Hall mobility:

$$\mu_\mathrm{H} = \sigma R_\mathrm{H} = \pm\frac{1}{\sigma}\int \mu(E)\sigma_E(E)\left(-\frac{\partial f}{\partial E}\right)dE, \tag{1.75}$$

where the sign is determined by the sign of q and $\mu(E)$ is the mobility of a carrier at a particular energy. Therefore, Hall measurements are not relevant for determining $\sigma_E(E)$ (but can be useful for extracting $\mu(E)$ if $\sigma_E(E)$ is already known).

[14]In the literature [14], this function is sometimes referred to as the "transport distribution function." However, what really describes the actual transport distribution is $\sigma_E(E)\left(-\frac{\partial f}{\partial E}\right)$ rather than just $\sigma_E(E)$. For example, at energies far away from E_F, the transport distribution should be zero; the potential capability to transport if E_F were to be shifted, however, can still be finite. Therefore, "transport function" appears to be a more appropriate term.

General forms of the phenomenological transport function $\sigma_E(E)$

The main purpose of the phenomenological formalism using $\sigma_E(E)$ is to extract $\sigma_E(E)$ from experimentally measured σ, S, and L. A general or ideal functional form of $\sigma_E(E)$ can be useful for this process, and will also help to identify outlying cases. In many cases, $\sigma_E(E)$ scales with energy in a simple power law above a certain edge. In Eq.1.71, τ, v_x, and $g(E)$ all scale with a power of energy above the band edge for the most typical case described in section 1.1. Thus, $\sigma_E(E) \propto E^s$ could be thought of as the most typical case for a dispersive $\sigma_E(E)$. Another case that represents a number of models when $\sigma_E(E)$ is a narrow function that can be approximated as a Dirac delta function. Both cases will be discussed in this section.

Dispersive Transport Function

As a general form of a dispersive $\sigma_E(E)$, it will prove useful to define parameters such as

$$\begin{aligned} \sigma_E(E) &= \sigma_{E_0} \cdot \left(\frac{E - E_\mathrm{t}}{k_\mathrm{B}T}\right)^s \qquad (E \geq E_\mathrm{t}) \\ &= 0. \qquad\qquad\qquad\quad (E < E_\mathrm{t}) \end{aligned} \tag{1.76}$$

Here, E_t is a phenomenological transport edge[15], s is a transport exponent, and σ_{E_0} is a transport coefficient in the units of conductivity. With this definition, phenomenological equations for the transport properties can be obtained. Conductivity from Eqs.1.69 and 1.76:

$$\sigma = \sigma_{E_0} \cdot sF_{s-1}(\eta), \tag{1.77}$$

where F_i was defined in Eq.1.51. Note that the definition of η, first given in Eq.1.50, is generalized here to explicitly reference the transport edge:

$$\eta = \frac{E_\mathrm{F} - E_\mathrm{t}}{k_\mathrm{B}T}. \tag{1.78}$$

In most contexts, $E_\mathrm{t} = 0$, making no difference in the equations. Seebeck Coefficient from Eqs.1.70 and 1.76:

$$S = \left(\frac{k_\mathrm{B}}{q}\right)\left[-\eta + \frac{(s+1)\,F_s(\eta)}{sF_{s-1}(\eta)}\right]. \tag{1.79}$$

Finally, Lorenz number from Eqs.1.73 and 1.76:

$$L = \left(\frac{k_\mathrm{B}}{q}\right)^2\left[\frac{(s+2)F_{s+1}(\eta)}{sF_{s-1}(\eta)} - \left(\frac{(s+1)F_s(\eta)}{sF_{s-1}(\eta)}\right)^2\right]. \tag{1.80}$$

[15]For example, in a band conductor, the band edge plays the role of a transport edge. Then one can set $E_\mathrm{t} = 0$ since the free carrier energy is 0 at the band edge

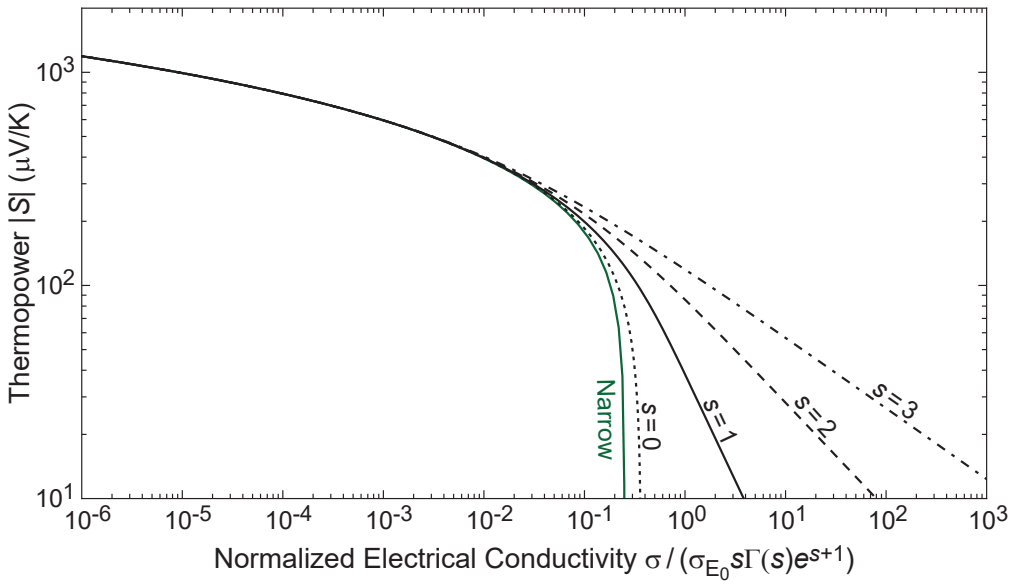

Figure 1.2: The thermopower-conductivity relation plotted for a number of phenomenological exponents. In the degenerate limit (low $|S|$) the linear slope of the log-log plot is $-\frac{1}{s}$. In the non-degenerate limit (high $|S|$), all cases have an identical curve shape. The narrow transport function case is shown together in green for comparison (for which conductivity is normalized such as σ/σ_{E_0}), being very similar to $s = 0$. Practically, $s = 0$ is not considered a physically feasible case.

Correspondence between the phenomenological (σ_{E_0}, s) and a particular physical model can be easily found by comparing the equations for σ, S, and L. For example, the deformation potential scattering model for band transport (section 1.1) would be observed with a phenomenological exponent $s = 1$. Ionized impurity scattering would be observed with $s = 3$. In both cases, σ_{E_0} is proportional to weighted mobility. Here it is seen that the exponent s is a parameter useful for distinguishing different transport mechanisms, whereas σ_{E_0} is useful for quantifying how conductive a sample could be for a given η.

Narrow transport function

The narrow transport function regime describes charge transport phenomena that results from having a transport channel that is narrow in energy such as an impurity band with almost no dispersion or for polaron states that are essentially centered around a particular energy level. Because extended states naturally form a dispersive energy landscape, the regime described with a narrow transport function could be considered a characteristic regime for transport through localized states.

The transport function in this regime could be a function with arbitrary shape that has finite values only around a particular energy level E_t. Since the energy scale relevant for the Fermi-Dirac distribution is $k_\mathrm{B}T$, any function that is sufficiently narrow relative to $k_\mathrm{B}T$ could be approximated as a Dirac delta function around E_t. That is, when

$$\begin{aligned} \sigma_E(E) &\neq 0 \qquad E - E_\mathrm{t} < k_\mathrm{B}T, \\ \sigma_E(E) &= 0 \qquad \text{Otherwise,} \end{aligned} \tag{1.81}$$

the transport function can be approximated such as

$$\sigma_E(E) = A_t \cdot \delta(E - E_\mathrm{t}), \tag{1.82}$$

where δ is a Dirac delta function and A_t is an energy-independent integrated property representing $\int \sigma_E dE$. By using Eqs.1.69 and 1.70, conductivity and the Seebeck coefficient become

$$\sigma = \sigma_{E_0} \cdot f(E_\mathrm{t})[(1 - f(E_\mathrm{t})], \tag{1.83}$$

and

$$S = \frac{E_\mathrm{t} - E_\mathrm{F}}{qT} = \frac{k_\mathrm{B}}{q} \cdot \ln\left(\frac{1 - f(E_\mathrm{t})}{f(E_\mathrm{t})}\right), \tag{1.84}$$

where q is the (signed) charge quantity of the charge carrier and $\sigma_{E_0} = A_\mathrm{t}/k_\mathrm{B}T$ is a coefficient in units of conductivity that determines the magnitude of conductivity.

It is interesting to note that, by setting $f(E_\mathrm{t}) = c$ (c: state occupancy) in Eqs.1.83 and 1.84, one obtains the Heikes formulae that are commonly referred to in the oxide literature. If one decides to use "site occupancy" as a parameter, which we here define as c', instead of state occupancy c, then spin degeneracy allows $f(E_\mathrm{t}) = c = c'/2$, giving the modified Heikes formulae [15, 16]. From the derivation here, it is seen that the difference between two versions of the formulae are simply a change in parameterization, and avoidable if one keeps the notation in terms of state occupancy. In the literature [15, 16], the Heikes formulae are often derived with the infinite temperature assumption, but mathematically it is equivalent to the narrow transport function assumption.

By calculating the Lorenz number using Eqs.1.73 with the narrow transport function:

$$L = 0. \tag{1.85}$$

This result is an interesting prediction of the phenomenology that has not yet been studied experimentally.

Using the $S-\sigma$ relation to determine $\sigma_E(E)$

In the dispersive transport function case, from Eqs.1.77-1.80, it is seen that σ_{E_0} and s can both be determined by the relation of either $S-\sigma$ or $L-\sigma$ where both relations are parameterized by η; S and L are a function of only η and s while σ is a function of σ_{E_0} in addition to η and s. In practice, L is more challenging to determine than S because: first, L does not change much (only about 60 % at maximum for $s = 1$) with η; second, it is difficult to distinguish whether thermal conductivity is changing with respect to η due to the Wiedemann-Franz law (effect of Lorenz number) or a variation in lattice thermal conductivity (*e.g.* doping causing increased phonon scattering).

The practically more rewarding approach is to thus investigate the $S-\sigma$ relation. In general, the $S-\sigma$ relation does not have an analytical expression, but the degenerate ($\eta \gg 1$) and non-degenerate ($\eta \ll -1$) limits can be studied to show that transport mechanisms are best distinguished in the degenerate limit. In the degenerate limit, Eqs.1.77 and 1.79 can be simplified by using the Sommerfeld expansion. Conductivity becomes

$$\sigma = \sigma_{E_0}\eta^s \quad (\eta \gg 1). \tag{1.86}$$

The Seebeck coefficient becomes

$$S = \left(\frac{k_B}{q}\right)\frac{\pi^2}{3}\frac{s}{\eta} \quad (\eta \gg 1). \tag{1.87}$$

By combining Eqs.1.86-1.87, the $S-\sigma$ relation in this limit becomes

$$S = \left(\frac{k_B}{q}\right)\frac{\pi^2}{3}s\left(\frac{\sigma}{\sigma_{E_0}}\right)^{-\frac{1}{s}} \quad (\eta \gg 1). \tag{1.88}$$

From this limit, it is seen that the s exponent can be readily found by examining the linear slope in a $\log S - \log\sigma$ plot (Fig.1.2). This type of plot is different than the traditional Jonker plot (linear S-$\log\sigma$). On the other hand, in the non-degenerate limit, conductivity becomes

$$\sigma = \sigma_{E_0}s\Gamma(s)\exp(\eta) \quad (\eta \ll -1), \tag{1.89}$$

where Γ is the gamma function ($\Gamma(n) = (n-1)!$ for positive integer n). The Seebeck coefficient becomes

$$S = \left(\frac{k_B}{q}\right)(s + 1 - \eta) \quad (\eta \ll -1). \tag{1.90}$$

By combining Eqs.1.89-1.90, the $S-\sigma$ relation in this limit becomes

$$S = \left(\frac{k_B}{q}\right)\left[s + 1 - \ln\left(\frac{\sigma}{\sigma_{E_0} s\Gamma(s)}\right)\right] \quad (\eta \ll -1). \tag{1.91}$$

It is seen that, regardless of s, the relation is always $S/\left(\frac{k_B}{q}\right) = \ln\sigma + \text{constant}$, making it hard to distinguish s in this limit (Fig.1.2). The Jonker plot (linear S-$\log\sigma$) yields a linear relation in this limit, which is a good way to visually demonstrate that the sample is in the non-degenerate limit and determine σ_{E_0} if s is already known.

In the narrow transport function case, by combining Eqs.1.83 and 1.84 to eliminate f, the $S-\sigma$ relation can be obtained:

$$\frac{\sigma}{\sigma_{E_0}} \cdot \left[1 + \exp\left(\frac{S}{k_B/q}\right)\right] \cdot \left[1 + \exp\left(\frac{-S}{k_B/q}\right)\right] = 1. \tag{1.92}$$

This equation determines the $\log|S| - \log\sigma$ curve shape, which is different than the dispersive cases (other than the non-physical $s = 0$). In Ch.2, two experimental cases, one showing $s = 1$ and the other showing narrow transport, will be contrasted.

Overall, for the purpose of phenomenologically characterizing the transport mechanism, it is best to have low thermopower ($|S| < 200\ \mu\text{V/K}$) samples and study them on a $\log S - \log\sigma$ plot.

References

[1] G. H. Döhler, "Conductivity, thermopower, and statistical shift in amorphous semiconductors", Physical Review B **19**, 2083–2091 (1979).

[2] J. Nell, B. Wood, S. Dorris, and T. Mason, "Jonker-type analysis of small polaron conductors", Journal of Solid State Chemistry **82**, 247–254 (1989).

[3] N. W. Ashcroft and N. D. Mermin, *Solid state physics* (Brooks Cole, 1976).

[4] S. M. Sze and K. K. Ng, *Physics of semiconductor devices* (Wiley-Interscience, 2006).

[5] S. R. de Groot and P. Mazur, *Non-equilibrium thermodynamics*, Dover edition, 1984 (North-Holland Pub. Co., 1962).

[6] B. M. Askerov, *Electron transport phenomena in semiconductors* (World Scientific, 1994).

[7] V. I. Fistul, *Heavily doped semiconductors* (Plenum Press, 1969).

[8] J. Bardeen and W. Shockley, "Deformation potentials and mobilities in non-polar crystals", Physical Review **80**, 72–80 (1950).

[9] E. Conwell and V. F. Weisskopf, "Theory of impurity scattering in semiconductors", Physical Review **77**, 388–390 (1950).

[10] J. W. Harrison and J. R. Hauser, "Alloy scattering in ternary III-V compounds", Physical Review B **13**, 5347–5350 (1976).

[11] J. M. Ziman, *Electrons and phonons* (Oxford Univ. Press, 1960).

[12] M. S. Dresselhaus, "Solid State Physics Part I: Transport Properties of Solids", MIT Lecture Notes.

[13] M. Cutler and N. F. Mott, "Observation of Anderson localization in an electron gas", Physical Review **181**, 1336–1340 (1969).

[14] G. D. Mahan and J. O. Sofo, "The best thermoelectric", Proceedings of the National Academy of Sciences **93**, 7436–7439 (1996).

[15] P. M. Chaikin and G. Beni, "Thermopower in the correlated hopping regime", Physical Review B **13**, 647–651 (1976).

[16] W. Koshibae, K. Tsutsui, and S. Maekawa, "Thermopower in cobalt oxides", Physical Review B **62**, 6869–6872 (2000).

Chapter 2

POLARON VS. BAND CONDUCTION: CeO_2 AND $SrTiO_3$

In certain metal oxides where conductivity is thermally activated and has a magnitude typically much lower than doped semiconductors, whether charge is transported through the hopping of localized small polarons[1] or the propagation of Bloch waves has been an elusive subject since the earliest studies [1]. Nowadays it is still not uncommon to find a lack of wide consensus on the electrical charge transport mechanism in broadly studied materials such as oxide perovskites. For example, the thermally activated electrical conduction observed in some $SrCoO_3$-based derivatives is not understood very well despite of much interest on those materials for their electrical conductivity in the air electrodes of electrochemical cells. In Nb-substituted polycrystals, the activation energy shows an apperent linear dependency on oxygen deficiency that extrapolates to zero [2], which is unexpected for polaron conduction. Impedance spectroscopy seems to preclude grain boundary effects, whereas single crystal measurements on the parent compound [3] suggest that the bulk conductivity should be band conduction. Relating the possible shift in the Fermi-level [4] to the activation energy could offer a good explanation, but additional measurements such as the Seebeck coefficient would be required to test different transport models. With materials being newly developed or discovered everyday, similar examples of materials that are technologically relevant, but are not yet well-understood fundamentally, seem to be increasing in number as well. A good case study demonstrating how transport analysis could be used to distinguish transport mechanisms would be helpful for motivating experimental effort on fundamental transport properties and for eventually facilitating the mechanistic understanding on modern materials.

The biggest reason why the conduction mechanism is not straightforwardly determined from basic conductivity measurements is because the temperature dependence $\sigma(T)$, by itself, does not provide an unambiguous signature. Even though polaron hopping [5–7] and band conduction [8] are completely different mechanisms in the physical description, they could both look similar in their exponential thermal activation behavior. In a non-degenerate band conductor where the Fermi-level is more

[1] "Polarons" are to be understood as small polarons unless noted otherwise.

than a few $k_{\mathrm{B}}T$ away from the band edge, exponential thermal activation behavior would be observed due to

$$\sigma = \sigma_{E_0} \cdot sF_{s-1}(\eta) \rightarrow \sigma_{E_0} \cdot \exp\eta \qquad (\eta \ll -1), \tag{2.1}$$

using the phenomenological description of conductivity (Eq.1.77 in Ch.1). This exponential dependency, $\exp\eta = \exp\left(\frac{E_{\mathrm{F}}-E_{\mathrm{t}}}{k_{\mathrm{B}}T}\right)$, is often understood as activation in the carrier concentration in Drude model terminology (see process ① in Fig.2.1). On the other hand, in small polaron conduction, the mobility of charge carriers are modeled as a thermally activated process such as $\mu \propto \frac{1}{T}\exp\left(-\frac{E_{\mathrm{a}}}{k_{\mathrm{B}}T}\right)$, where E_{a} is an activation energy for polaron hopping. In the phenomenological description, activation in mobility corresponds to

$$\sigma_{E_0} \propto \frac{1}{T}\exp\left(-\frac{E_{\mathrm{a}}}{k_{\mathrm{B}}T}\right), \tag{2.2}$$

which would, most of the times, combine with the activation effect of Eq.2.1 when measuring $\sigma(T)$, as illustrated in Fig.2.1 (process ② in addition to ①). Even in the more general case when the transport function is not exactly in a form of a power law [9] as was assumed in Eq.2.1, or when the mobility is described with a different type of thermal activation (*e.g.* $\exp\left[\left(-\frac{E_a}{k_{\mathrm{B}}T}\right)^{\gamma}\right]$ which appears in both variable range hopping or percolation models [5]), the ambiguity between the $E_{\mathrm{F}} - E_{\mathrm{t}} < 0$ effect and the thermally activated mobility effect remains to be a problem in interpreting $\sigma(T)$.

It should be noted that extrinsic effects like grain boundary resistance [10] could also give rise to a thermally activated $\sigma(T)$ (see Ch.4). Although it is desired to avoid such complications from the perspective of understanding the intrinsic charge transport mechanism of the material, grain boundary effects more than often dominate the behavior of $\sigma(T)$. This tendency is partly inevitable because our interest is in non-metals where grain boundary effects cannot be screened very well by charges [11]. Such extrinsic effects could be ruled out if measurements on single crystals are available.

Due to such a variety of causes that could make conductivity appear to be a thermally activated property, attribution to a particular cause could be based on support from circumstantial observations. For example, signatures in optical measurements are able to be associated with the presence of polarons [6, 12–14]. However, the mere presence of polarons, or their contribution to optical conductivity, does not warrant that they significantly contribute to the direct current (DC) charge transport behavior.

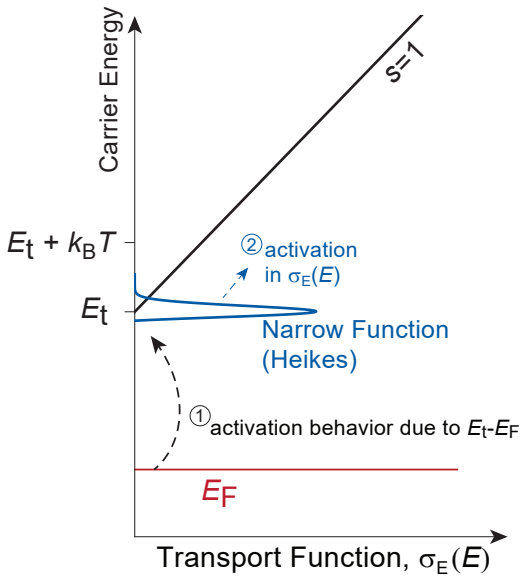

Figure 2.1: Schematic illustration of two processes that result in thermally activated conduction. Process ① is due to the Fermi-level being below the transport edge, whereas process ② is due to the transport function itself being a thermally activated process.

Therefore, it is difficult to pinpoint a mechanism when the essential data – stationary transport data – is limited to only DC conductivity.

Seebeck coefficient has been used in some studies to complement the analysis on conductivity. In one of the rare cases where narrow band conduction has been shown unambiguously, Tuller and Nowick [15] investigate both conductivity and the Seebeck coefficient of ceria; particularly, their dependencies on temperature and carrier concentration is compared with the Heikes model. In general, the Seebeck coefficient is a very useful addition in understanding transport because it reflects the same transport function $\sigma_E(E)$ as conductivity, but with a different weighting at each energy of the carrier (recall from Ch.1 that the same $\sigma_E(E)$ described both S and σ and the difference was mainly the sampling functions shown in Fig.1.1).

In this chapter, it will be shown that the thermopower-conductivity $|S| - \sigma$ relation could be examined to determine the transport function and characterize the transport mechanism in a more straightforward manner compared with studying S and σ separately. $SrTiO_3$ and CeO_2 are used as examples to show that these materials show charge transport behavior consistent with band and polaron conduction, respectively [16].

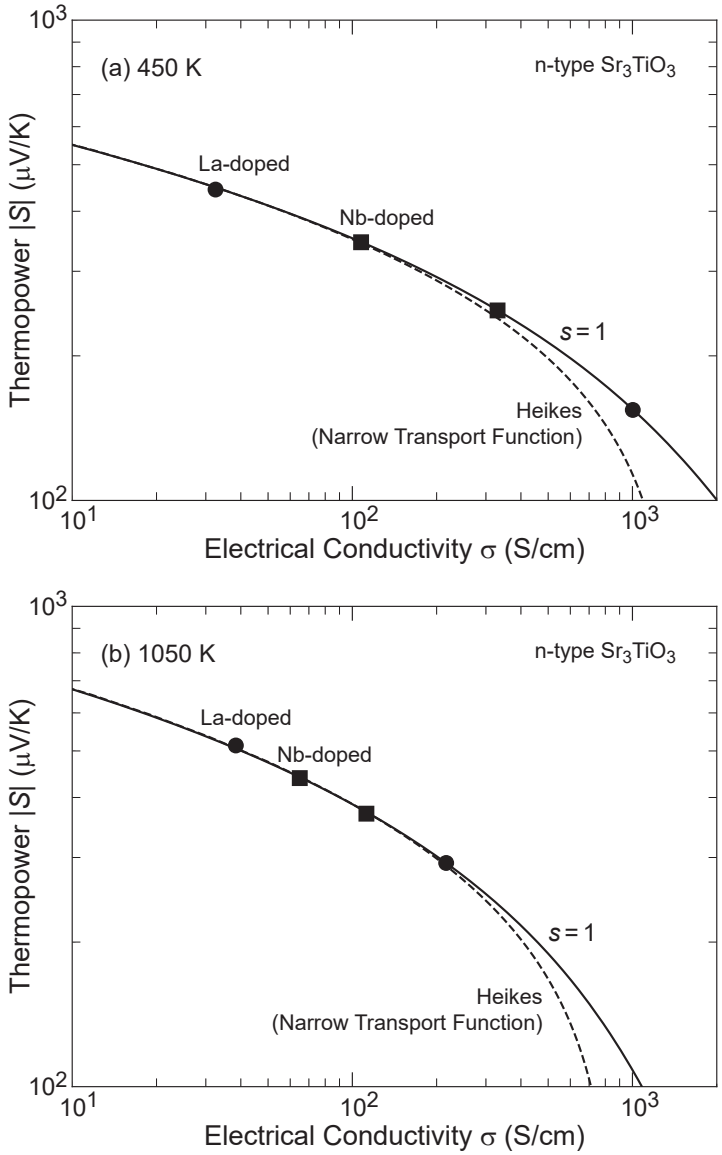

Figure 2.2: Analysis of the $\log|S| - \log\sigma$ relation in single crystal n-type $SrTiO_3$ doped with either La (circles) or Nb (squares). At **(a)** 450 K, data clearly follow the $s = 1$ relation rather than the Heikes relation, indicating band transport. At **(b)** 1050 K, the thermopower of the samples are too large to distinguish between different mechanisms. Data are from Ref.[17].

2.1 Band conduction in $SrTiO_3$

Strontium titanate $SrTiO_3$ is one of the most widely studied perovskites for its electronic properties [19–21]. $SrTiO_3$ has been widely recognized as a band conductor in the literature [17, 18, 22–26], although some reports on the polycrystalline form cite hopping conduction [27–30]. Precisely how band conduction should be justified and what models should be used to quantitatively analyze transport measurements

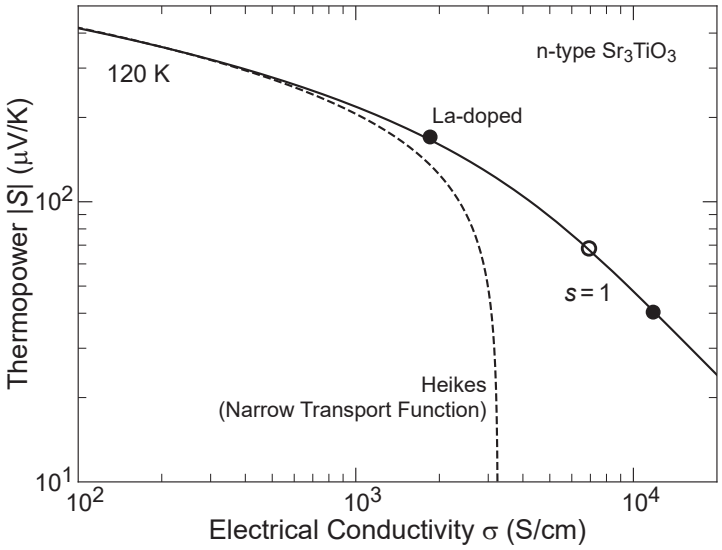

Figure 2.3: Low temperature (120 K) analysis of the $\log|S| - \log\sigma$ relation in single crystal n-type $SrTiO_3$ doped with La. Conductivity of the open circle data point was interpolated from adjacent compositions. Data are from Ref.[18].

are topics with not much consensus; found in the literature are mixed assessments on the scattering mechanisms including ionized impurity scattering [18, 22], deformation potential scattering [17], and polar optical phonon scattering [17]. Here, we show through a Seebeck-conductivity analysis that doped n-type $SrTiO_3$, at 120 K and above, clearly follows the model curve for band conduction as predicted by deformation potential scattering.

The experimental $\log|S| - \log\sigma$ relation in n-type doped $SrTiO_3$ is seen to follow the $s = 1$ curve (Fig.2.2 and 2.3), which corresponds to the typical relation of band conduction with deformation potential scattering (acoustic or non-polar optical phonons). On the other hand, the curve predicted for a narrow transport function, which includes the case of small polaron hopping, shows a steeper decrease in thermopower at high doping levels. This analysis allows us to unambiguously conclude that the energy dependency of the transport function is $\sigma_E \propto E$ above the transport edge.

At this point the transport function is phenomenologically determined to be $s = 1$, but not particularly associated with a physical model. This phenomenology already allows one to reject the claim of narrow-energy polaron mediated transport (see section 1.3) in favor of band transport. To find a physical model consistent with the phenomenology, the energy and temperature dependencies of the function σ_E

should be further investigated.

$s = 1$ is consistent with the energy dependency of deformation potential scattering. It is worth noting why this correspondence is still true in $SrTiO_3$ despite of the non-spherical complex Fermi-surface. For deformation potential scattering, the energy dependency of scattering originates from the dependency on the density of states $g(E)$:

$$\tau(E) \propto \frac{1}{g(E)}, \tag{2.3}$$

Therefore, in the transport function, the energy dependencies of $\tau(E)$ and $g(E)$ cancel each other and the energy dependency of $\sigma_E(E)$ is determined by the square of group velocity v_x of Bloch waves (for transport in the a particular direciton x):

$$\sigma_E(E) = e^2 \left\langle v_x^2(E) \right\rangle_E \tau(E) g(E) \propto \left\langle v_x^2(E) \right\rangle_E . \tag{2.4}$$

Here, the bracket $\langle\rangle_E$ indicats an average at energy E. To understand the relevant $v^2(E)$ relation for the $SrTiO_3$ Fermi-surface which has a three-fold symmetry from the cubic crystal system, one could conceptually decompose the Fermi-surface into three interpenetrating prolate ellipsoids that are orthogonal to each other. In ellipsoids, $\left\langle v_x^2(E) \right\rangle_E \propto E$, yielding the $s = 1$ relation. In general, as long as the Fermi-surface can be described well-enough with an effective inertial mass, the transport function for deformation potential scattering will be well described with $s = 1$.

The identification of the $s = 1$ relation also indicates that polar-optical phonon scattering, which has been suggested in Ref.[17], is not the dominating transport mechanism in $SrTiO_3$. From an argument analogous to that for deformation potential scattering, polar-optical phonon scattering can be shown to yield a $s = 2$ relation [31], which is discrepant than the experimental observation shown in Fig.2.2. In Ref.[17], analysis on the scattering mechanism was done by fitting the scattering parameter to reproduce the thermopower-carrier concentration relation. However, unlike conductivity or thermopower which could be effectively characterized by a single effective mass in $SrTiO_3$, for carrier concentration the actual dispersion matters since it takes into account all states regardless of its contribution to transport. In other words, the effective mass for density of states is not energy- and temperature-independent. This complication illustrates another reason why it is more straightforward to investigate the thermopower-conductivity relation when studying the transport mechanism. Carrier concentration is more useful for un-

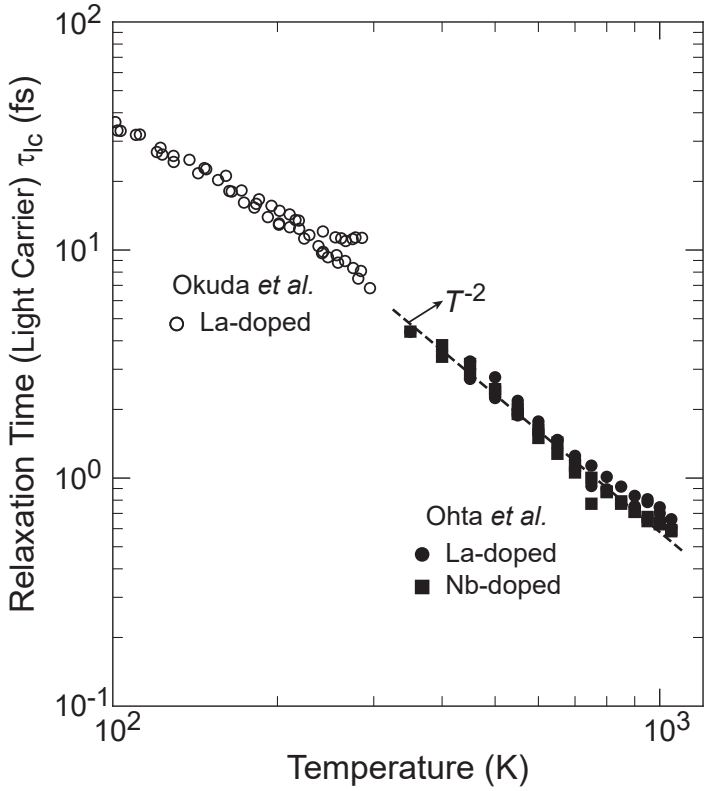

Figure 2.4: The temperature dependent relaxation time of the light carriers in n-type single crystal $SrTiO_3$ extracted from thermopower and conductivity using Eq.2.5. A dashed line of $\propto T^{-2}$ dependency is drawn for comparison. High and low temperature data are from Ref.[17] and Ref.[18], respectively. The lattice constant was fixed at $a = 3.905$ Å [32] for the calculation.

derstanding the structure of the Fermi-surface rather than for understanding the transport mechanism due to their dependency on density of states.

Ionized impurity scattering, which has been suggested as the dominant mechanism at low temperatures [18, 22], is also excluded at temperatures above 120 K since it would result in $s = 3$.

It is seen from Fig.2.2b that, at 1050 K, the thermopower of the samples are too high to be able to distinguish between different scattering mechanisms. However, since no obvious signs of a crossover in the transport mechanism is observed with increasing temperature, it is most likely that the transport mechanism remains consistent throughout the temperature range. To illustrate this point more clearly, $\tau(T)$ is examined by assuming $s = 1$. To quantify τ, a more specific model of the Fermi-surface is needed, which can be done in a simplified way by decomposing the $SrTiO_3$ Fermi-surface into three prolate ellipsoids. Each ellipsoid is then char-

acterized by one light effective mass for the two short principal axes and another heavy effective mass for the one long principal axis. The big contrast between the light and heavy effective masses makes only the light one important for transport. The identical mass determines the transport in the other two prolate ellipsoids due to the three-fold cubic symmetry. As a result, a single effective mass largely determines the isotropic transport in the $SrTiO_3$ conduction band, even when the actual dispersion is highly non-spherical. In this limit where each prolate ellipsoid of the Fermi-surface is characterized by a single effective mass (*i.e.* an ellipsoid becomes a cylinder), the conductivity can be described as (see Section 2.4 of the chapter)

$$\sigma = \frac{8\pi e^2 k_B T}{ah^2} \tau_{lc}(T) \cdot \ln(1 + \exp \eta), \tag{2.5}$$

where a is the lattice constant and τ_{lc} is the relaxation time of the light carriers (which is independent of energy due to the two-dimensional nature of the density of states of the light carriers). The extracted relaxation time using Eq.2.5 is shown in Fig.2.4. It is seen that the relaxation time largely follows an identical trend over the entire temperature range, suggesting that the form of the transport function is unchanged at high temperatures.

The next question is whether $\tau \propto T^{-2}$ is consistent with deformation potential scattering. At first glance, it may seem not because $\tau \propto T^{-1}$ for deformation potential scattering from a typical 3D Fermi-surface, as summarized in Table 1.1. However, when the Fermi surface is elongated like a cylinder, it has been pointed out [33] that a distinct regime with $\tau \propto T^{-2}$ emerges when the phonon wave vectors responsible for deformation potential scattering are thermally saturated in the Fermi surface short axis while still under-saturated in the long-axis. This behavior has been observed in Bi at low temperature (noted as $\rho \propto T^2$, where ρ is resistivity) [33, 34], but in $SrTiO_3$ it is expected to be observed at a higher temperature because of the much larger Fermi surface. The lower bound of this temperature range can be estimated by finding at which temperature the relevant phonon waves exceed the diameter of the Fermi surface cylinder (T_D). The highest doping sample will have the highest T_D: using the $S \approx 40$ μV/K sample at 120 K (Fig.2.3), $T_D \approx 180$ K (speed of sound of $v_s = 7900$ m/s in the [100] direction and $m_l^* = 1.1 m_e$ assumed for this estimation). Therefore, this explanation is consistent with the observation of $\tau \propto T^{-2}$ in Fig.2.4.

Consideration of the upper temperature bound of the $\tau \propto T^{-2}$ suggests that optical deformation potential could be involved, in addition to the acoustic deformation

potential. The Fermi surface of n-type $SrTiO_3$ is elongated along the entire Brillouin zone, making the upper temperature bound simply limited to the Debye temperature for the contribution from acoustic phonons. Using v_s = 7900 m/s, the Debye temperature is estimated as 485 K, but the $\tau \propto T^{-2}$ seems to continue above this temperature in Fig.2.4. The dispersive optical branches in $SrTiO_3$ could contribute in a similar way to acoustic phonons. The energy dependencies of acoustic and long range optical phonons (*i.e.* non-polar optical phonons) are the same [31].

In the literature, the $\tau \propto T^{-2}$ (or $\rho \propto T^2$) dependency has mostly been discussed in the context of Fermi liquid behavior and electron-electron interactions [35]. However, it is not clear whether electron-electron scattering should dominate over deformation potential scattering at temperatures as high as 1000 K. Furthermore, whether electron-electron scattering should closely follow $s = 1$ is also unclear. Overall, deformation potential scattering seems to provide a better explanation for the charge transport in n-type $SrTiO_3$.

Most transition metal oxide perovskites have a similar orbital and bonding configuration, and thus have similar features in the Fermi surface (cylinder-like and elongated). A number of these materials have been highlighted for its T^2 resistivity behavior at temperatures not too low: $PrNiO_3$ [36], $KTaO_3$ [37], $SrNbO_3$ [38], and $SrMoO_3$ [39]. These examples with similar behavior further support the idea that $\tau \propto T^{-2}$ is related to the Fermi surface anisotropy rather rather than electron-electron scattering.

Overall, the observed $s = 1$ relation in single crystals concludes the transport mechanism in n-type $SrTiO_3$ to be band conduction as opposed to polaron hopping. Deformation potential scattering is found to be consistent with the energy and temperature dependency of the phenomenological transport function. The thermally activated conduction behavior observed in some polycrystalline samples should therefore be attributed to grain boundary effects rather than an intrinsic conduction mechanism of $SrTiO_3$. The mathematically identical $S - \sigma$ relation between band transport and hopping at low doping levels illustrates how any hopping model could appear to apparently explain the transport when only low doping samples are studied. Although the temperature dependency of the transport function, which would increase with temperature in hopping models, would still allow to show disagreement with experiments, interpretation of the temperature dependence could be ambiguous if $\sigma(T)$ is analyzed instead of properly extracting the transport function. Finally, it should be noted that features of band transport do indicate it as the dominant trans-

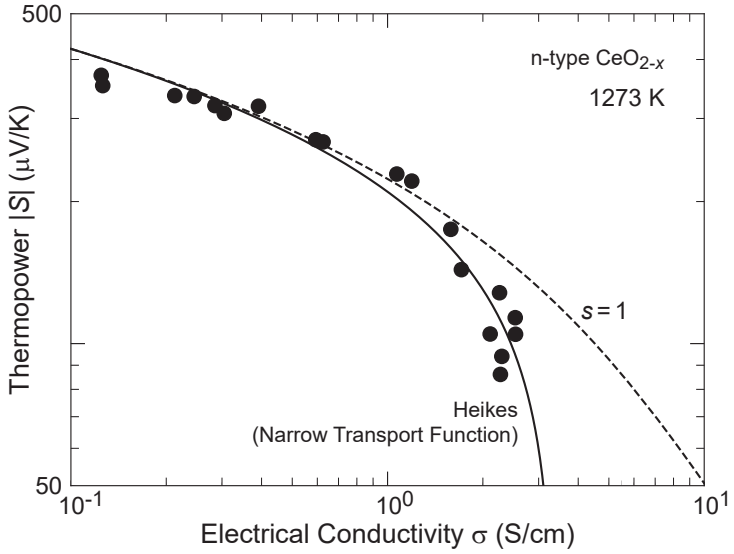

Figure 2.5: Analysis of the $\log|S| - \log\sigma$ relation in single crystal n-type CeO_{2-x}, reduced to different compositions by CO/CO_2 atmosphere control. The data follow the Heikes relation rather than $s = 1$, indicating that a narrow transport function is governing the transport in this material (such as small polaron conduction). Data are from Ref.[15]. To find the thermopower corresponding to each conductivity measurement, the Seebeck coefficient vs. composition data reported in the same reference was fitted to find an empirical relation, which was then applied to the conductivity vs. composition data.

port mechanism in doped n-type $SrTiO_3$, but does not preclude polaron conduction entirely for other regimes. In pure and stoichiometric $SrTiO_3$ where the extrinsic or self-doping level is extremely low, the conductivity due to band conduction could be low enough to make polaron hopping conduction possibly the dominant transport mechanism [40, 41].

2.2 Small polaron conduction in CeO_2

Ceria is a material widely used for its promising oxygen redox properties [42, 43]; for instance, in electrochemical cells, the electro-oxidation of hydrogen gas is effective with ceria, owing to its electrical conductivity that increases the reaction zone at which the electrochemical reaction can happen [44]. The mechansim by which charge is transported has been described as small polaron conduction [15]. Here, it is shown that the identical conclusion can be reached thorugh a simpler route of analyzing the $S - \sigma$ relation at a given temperature. The complicated phase diagram of CeO_{2-x}, which limits the temperature and off-stoichiometry range in which the material is a single fluorite phase, makes the simple $S - \sigma$ analysis more meritable.

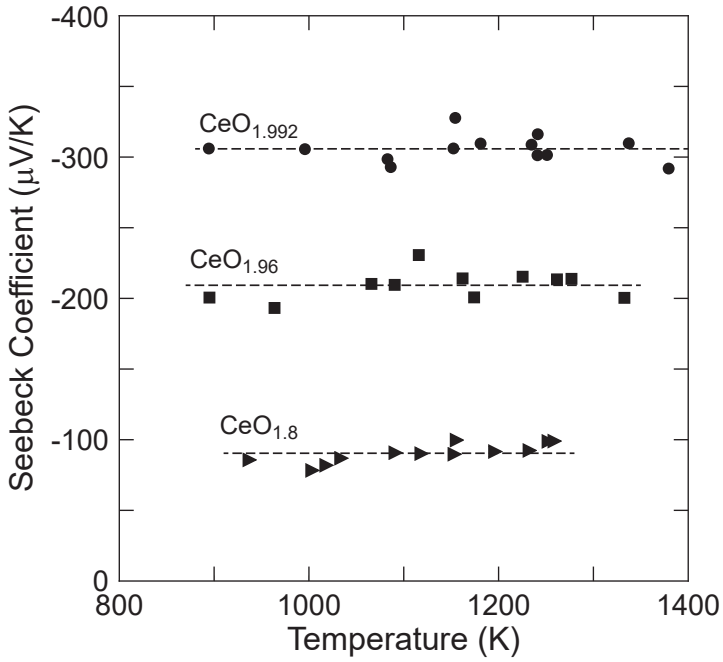

Figure 2.6: Temperature dependency of the Seebeck coefficient in single crystal CeO_{2-x}. The data set is a compilation from two studies as reported in Ref.[15]. The dashed lines are guides to the eye showing the average value with respect to temperature.

The $\log|S| - \log\sigma$ relation observed in single crystal CeO_{2-x} at 1273 K follows that predicted by a narrow transport function, which is significantly different than what is predicted by band transport (Fig.2.5). A narrow transprot function indicates that transport only occurs at or near a particular energy level (the transport edge) but not at energies above or below more than $\approx k_B T$. Such a feature is characteristic of polarons as opposed to band carriers with an energy dispersion.

Note that information about polaron site occupancy (c', see notes in section 1.3), or even composition, is not explicitly required for the analysis in Fig.2.5. This analysis is more straightforward than analyzing $S(c')$ or $\sigma(c')$ because of the ambiguity of how c' corresponds to a particular composition. As long as it is known how a particular S corresponds to a particular σ, which is a matter of experimental control rather than an issue of making assumptions about polaronic states and defect concentrations, the $S - \sigma$ relation can be examined. This advantage of analyzing $S - \sigma$ is analogous to not requiring information about the carrier concentration when studying band conductors.

The temperature dependence of the Seebeck coefficient could be used to support the

conclusion of a narrow transport function. When the number of charge carriers is extrinsically fixed in a material (*e.g.* a fixed defect concentration while having no bipolar exciations), thermopower becomes temperature independent for a desnity of states that is a narrow peak function around a particular energy level. This independency results from the Fermi-level self-adjusting with temperature in a way that gives a constant reduced Fermi-level. Suppose that the number of electrons provided by defects or dopants is fixed at n_0. Then, the Fermi-level would be determined by

$$n_0 = \int g(E) f\left(\frac{E - E_\mathrm{F}}{k_\mathrm{B}T}\right) dE, \tag{2.6}$$

where f is the Fermi-Dirac distribution function. When the density of states is a narrow function around E_t, $g(E) \approx N \cdot \delta(E_\mathrm{t})$. As a result,

$$n_0 \approx N \cdot f\left(\frac{E_\mathrm{t} - E_\mathrm{F}}{k_\mathrm{B}T}\right) = N \cdot f(-\eta). \tag{2.7}$$

Therefore, when $c = n_0/N$ is fixed with respect to temperature, η is also fixed (*i.e.* E_F shifts in a way that keeps η constant). Recalling that the Seebeck coefficient is a function of only η for a given system, a temperature-independent η makes the Seebeck coefficient also temperature-independent.

The Seebeck coefficient of CeO_{2-x} is indeed observed to be insensitive to temperature for a fixed oxygen deficiency x, as shown in Fig.2.6. In this measurement, the composition of CeO_{2-x} was fixed by equilibrating with a predetermined reducing atmosphere and then quenching to lower temperatures. Since the electrons are provided by the oxygen vacancies in CeO_{2-x}, fixing the composition is equivalent to fixing n_0 or c. The observation that S and η appears to be fixed with respect to temperature under these measurement conditions thus supports the conclusion from the $\log|S| - \log\sigma$ that the transport is described with a narrow transport function.

2.3 Notes on assumptions related to modeling oxide materials

On the use of a homogeneous transport function

Decomposing conductivity in energy space such as $\sigma = \int \sigma_E(E)\frac{-\partial f}{\partial E}dE$ is a procedure that relies on the assumption that the material system can be described with a single homogeneous transport function [10]. This assumption is conventionally discussed in terms of phase or compositional homogeneity, but it should be noted that there could be subtle but significant differences between the transport function homogeneity and chemical homogeneity. For example, a phase-pure and compositionally homogeneous polycrystalline sample could be considered chemically

homogeneous if the impact of grain boundaries on compositional variation is negligible. However, even for a chemically ideal grain boundary, the grain boundary electronic structure is always different than the grain, inducing some charge transfer (of varying degrees). Depending on how significant the charge transfer is and how well the transfered charges are screened, the consequential electronic structure change in the *grain* (*e.g.* band bending) could be significant enough to result in an added resistance larger than that of the grain boundary itself. In this case, the transport function would be inhomogeneous, requiring to integrate the transport function separately near the grain boundary (which effectively results in a multi-phase problem; see Ch.4 showing a case where the use of an effective homogeneous function is not a sufficient workaround), despite of chemical homogeneity. Now, suppose that the polycrystalline material was modified to have a more conductive composition near the grain boundary such that the grain boundaries do not provide added resistance anymore (*e.g.* n-type oxides synthesized under reducing conditions [45–47]). Then, the material could possibly be described well enough with a homogeneous transport function because of the grain boundary only being a minuscule part of the entire material, but chemically the material has become inhomogeneous.

Therefore, it is critical to consider whether the material being studied can be described effectively with a homogeneous transport function. When single crystal samples are not available and the impact of grain boundaries is unknown, this question about the homogeneous assumption could limit the conclusiveness of a $\log|S| - \log\sigma$ analysis. This issue is of more concern in oxides where the redox kinetics, combined with ineffective screening, make the sample prone to the development of space charge regions near the grain boundary.

On the rigid transport function assumption

Inferring the form of the transport function from a $\log|S| - \log\sigma$ plot requires multiple samples with different Fermi-levels. In oxides, E_F can be controlled either by extrinsic doping or by oxygen off-stoichiometry control. Whether such processes will keep the transport function unchanged could be a challenging question to answer. Largely two different cases should be considered when rethinking the starting assumption of a "rigid" transport function (the term "rigid" originates from the "rigid band assumption" in electronic structure studies).

The first concern is whether the functional form of the transport function is changing as the sample is tuned in order to change E_F. Since a change in the functional form

is indicative of a change or crossover in the dominant transport mechanism, it is expected to exhibit other accompanying changes that signify the crossover. For example, crossovers in the temperature dependency of mobility, relaxation time, or σ_{E_0} would indicate possible crossovers in the transport mechanism.

Another concern is the transport coefficient σ_{E_0} being systematically correlated to changes in the E_F. A common example would be a dopant – intended to only change the E_F but not the band itself – rather acting as an alloying element to change the band effective mass, such as the case of Fe-substituted $SrTiO_3$ [23]. This type of breakdown of the rigid transport function is harder to notice because of its continuous and systematic dependence of σ_{E_0} on the chemical substitution; a system with a transport function of $s = 1$ could appear to have a significantly different curve shape in the $\log|S| - \log\sigma$ plot due to a continuously changing σ_{E_0}. Measurement of the Hall mobility could help notice such changes, but only if Hall mobility is converted to an η-independent transport parameter (*e.g.* μ_0 or σ_{E_0}); Hall mobility itself is intrinsically η-dependent in the heavily doped regime even for a rigid transport function. Comparing the effect of multiple types of dopants (*e.g.* comparing Nb and La dopants in $SrTiO_3$) is a useful way to confirm the validity of a rigid transport function assumption. Investigation of the non-degenerate limit, in which Hall mobility is expected to be constant with respect to E_F for a rigid transport function, is an alternative way to test the rigidity assumption.

2.4 Appendix: Physical transport model for n-type $SrTiO_3$

The Fermi-surface of n-type $SrTiO_3$ originates from three interpenetrating prolate ellipsoids along each principal axis that are symmetrically identical. The dispersion relation of a prolate ellipsoid aligned along the z-axis is

$$E = \frac{\hbar^2(k_x^2 + k_y^2)}{2m_{\mathrm{lc}}^*} + \frac{\hbar^2 k_z^2}{2m_{\mathrm{hc}}^*}, \tag{2.8}$$

where k_i is the Bloch wave number along the i-direction. Due to the order-of-magnitude difference between m_{lc}^* and m_{hc}^* in $SrTiO_3$, transport is dominated by the light carriers with an effective mass of m_{lc}^*. Therefore, in terms of transport, the second term in Eq.2.8 becomes non-significant, making the cylindrical geometry a good model Fermi-surface.

Conductivity along the x-direction in a cylindrical Fermi-surface aligned with z can be calculated by using the solution of the Boltzmann transport equation (Eq.1.12):

$$\sigma_{xx} = e^2 \int v_x^2(E)\tau(E)g(E)\left(\frac{-\partial f}{\partial E}\right) dE. \tag{2.9}$$

By taking advantage of the rotational symmetry in the $x-y$ plane of a cylinder, v_x^2 can be replaced with $v^2/2 = E/m_{\mathrm{lc}}^*$ (equipartition). $g(E)$ can be derived from that of a 2D k-space ($m^*/\pi\hbar^2$) by multiplying it with the number of k-points along the z-axis ($1/a$ where a is the lattice parameter in real space):

$$g^{\mathrm{cylinder}} = \frac{m_{\mathrm{lc}}^*}{a\pi\hbar^2}. \tag{2.10}$$

The conductivity of a cylindrical Fermi-surface becomes

$$\sigma_{xx}^{\mathrm{cylinder}} = \frac{e^2}{a\pi\hbar^2}\int E\tau(E)\left(\frac{-\partial f}{\partial E}\right)dE. \tag{2.11}$$

In $SrTiO_3$, two cylinders (aligned along z- and $y-$axes) contribute to conduction in the x-direction such that $\sigma_x = 2\sigma_x^{\mathrm{cylinder}}$, which is also the isotropic conductivity. For $\tau(E)$, it is known from the phenomenological identification of $s = 1$ that τ should be energy-independent. This conclusion is consistent with deformation potential scattering because the density-of-states, which determines the energy dependency of τ for deformation potential scattering (Eq.2.3), is energy-independent (Eq.2.10). Taking into account these understandings, the conductivity in $SrTiO_3$ due to light carriers becomes:

$$\begin{aligned}\sigma_{\mathrm{lc}}^{\mathrm{SrTiO_3}} &= \frac{2e^2\tau_{\mathrm{lc}}}{a\pi\hbar^2}\int E\left(\frac{-\partial f}{\partial E}\right)dE \\ &= \frac{2e^2k_{\mathrm{B}}T\tau_{\mathrm{lc}}}{a\pi\hbar^2}F_0(\eta).\end{aligned} \tag{2.12}$$

For a full derivation, one could integrate in k-space to obtain the identical result.

References

[1] A. Bosman and H. van Daal, "Small-polaron versus band conduction in some transition-metal oxides", Advances in Physics **19**, 1–117 (1970).

[2] R. E. Usiskin, T. C. Davenport, R. Y. Wang, W. Guan, and S. M. Haile, "Bulk properties of the oxygen reduction catalyst $SrCo_{0.9}Nb_{0.1}O_{3-\delta}$", Chemistry of Materials **28**, 2599–2608 (2016).

[3] Y. Long, Y. Kaneko, S. Ishiwata, Y. Taguchi, and Y. Tokura, "Synthesis of cubic $SrCoO_3$ single crystal and its anisotropic magnetic and transport properties", Journal of Physics: Condensed Matter **23**, 245601 (2011).

[4] M. H. R. Lankhorst, H. J. M. Bouwmeester, and H. Verweij, "Use of the rigid band formalism to interpret the relationship between O chemical potential and electron concentration in $La_{1-x}Sr_xCoO_{3-\delta}$", Physical Review Letters **77**, 2989–2992 (1996).

[5] N. F. Mott and E. A. Davis, *Electronic processes in non-crystalline materials*, 2nd ed. (Oxford University Press, 1979).

[6] J. T. Devreese and A. S. Alexandrov, "Fröhlich polaron and bipolaron: recent developments", Reports on Progress in Physics **72**, 066501 (2009).

[7] R. R. Heikes and R. W. Ure, *Thermoelectricity: science and engineering* (Interscience Publishers, 1961).

[8] J. M. Ziman, *Electrons and phonons* (Oxford Univ. Press, 1960).

[9] H. Killias, "Temperature-dependent Arrhenius factor for small-polaron conduction in glasses", Physics Letters **20**, 5–6 (1966).

[10] J. J. Kuo, S. D. Kang, K. Imasato, H. Tamaki, S. Ohno, T. Kanno, and G. J. Snyder, "Grain boundary dominated charge transport in Mg_3Sb_2-based compounds", Energy & Environmental Science **11**, 429–434 (2018) 10.1039/C7EE03326E.

[11] G. E. Pike and C. H. Seager, "The dc voltage dependence of semiconductor grain-boundary resistance", Journal of Applied Physics **50**, 3414–3422 (1979).

[12] H. G. Reik, "Optical effects of small polarons at high frequencies with an application to reduced strontiumtitanate", Zeitschrift für Physik **203**, 346–361 (1967).

[13] J. T. Devreese, S. N. Klimin, J. L. M. van Mechelen, and D. van der Marel, "Many-body large polaron optical conductivity in $SrTi_{1-x}Nb_xO_3$", Physical Review B **81**, 125119 (2010).

[14] D. M. Eagles and P. Lalousis, "Optical absorption by mixed polarons. II. application to $SrTiO_3$", Journal of Physics C: Solid State Physics **17**, 655–668 (1984).

[15] H. Tuller and A. Nowick, "Small polaron electron transport in reduced CeO_2 single crystals", Journal of Physics and Chemistry of Solids **38**, 859–867 (1977).

[16] S. D. Kang, M. Dylla, and G. J. Snyder, "Thermopower-conductivity relation for distinguishing transport mechanisms: polaron hopping in CeO_2 and band conduction in $SrTiO_3$", Physical Review B, accepted (2018).

[17] S. Ohta, T. Nomura, H. Ohta, and K. Koumoto, "High-temperature carrier transport and thermoelectric properties of heavily La- or Nb-doped $SrTiO_3$ single crystals", Journal of Applied Physics **97**, 034106 (2005).

[18] T. Okuda, K. Nakanishi, S. Miyasaka, and Y. Tokura, "Large thermoelectric response of metallic perovskites: $Sr_{1-x}La_xTiO_3$ ($0 \leq x \leq 0.1$)", Physical Review B **63**, 113104 (2001).

[19] J. Mannhart and D. G. Schlom, "Oxide interfaces–an opportunity for electronics", Science **327**, 1607–1611 (2010).

[20] A. F. Santander-Syro, O. Copie, T. Kondo, F. Fortuna, S. Pailhès, R. Weht, X. G. Qiu, F. Bertran, A. Nicolaou, A. Taleb-Ibrahimi, P. L. Fèvre, G. Herranz, M. Bibes, N. Reyren, Y. Apertet, P. Lecoeur, A. Barthélémy, and M. J. Rozenberg, "Two-dimensional electron gas with universal subbands at the surface of $SrTiO_3$", Nature **469**, 189–193 (2011).

[21] R. Waser and M. Aono, "Nanoionics-based resistive switching memories", Nature Materials **6**, 833–840 (2007).

[22] M. Ahrens, R. Merkle, B. Rahmati, and J. Maier, "Effective masses of electrons in n-type $SrTiO_3$ determined from low-temperature specific heat capacities", Physica B: Condensed Matter **393**, 239–248 (2007).

[23] A. Rothschild, W. Menesklou, H. L. Tuller, and E. Ivers-Tiffée, "Electronic structure, defect chemistry, and transport properties of $SrTi_{1-x}Fe_xO_{3-y}$ solid solutions", Chemistry of Materials **18**, 3651–3659 (2006).

[24] H. Muta, K. Kurosaki, and S. Yamanaka, "Thermoelectric properties of rare earth doped $SrTiO_3$", Journal of Alloys and Compounds **350**, 292–295 (2003).

[25] R. Moos, A. Gnudi, and K. H. Härdtl, "Thermopower of $Sr_{1-x}La_xTiO_3$ ceramics", Journal of Applied Physics **78**, 5042–5047 (1995).

[26] H. P. R. Frederikse, W. R. Thurber, and W. R. Hosler, "Electronic transport in strontium titanate", Physical Review **134**, A442–A445 (1964).

[27] T. Hara and K. Shinozaki, "Effect of oxygen adsorption on polaron conduction in nanometer-scale Nb^{5+}-, Fe^{3+}-, and Cr^{3+}-doped $SrTiO_3$ thin films", Japanese Journal of Applied Physics **50**, 065807 (2011).

[28] P. Roy, V. Pal, and T. Maiti, "Effect of spark plasma sintering (SPS) on the thermoelectric properties of $SrTiO_3$:15 at% Nb", Ceramics International **43**, 12809–12813 (2017).

[29] C. Ang, J. R. Jurado, Z. Yu, M. T. Colomer, J. R. Frade, and J. L. Baptista, "Variable-range-hopping conduction and dielectric relaxation in disordered $Sr_{0.97}(Ti_{1-x}Fe_x)O_{3-\delta}$", Physical Review B **57**, 11858–11861 (1998).

[30] G. Campet, S. Z. Wen, C. Puprichitkun, J. P. Manaud, and J. Claverie, "Physical properties of (n+)$SrTiO_3$ films", Physica Status Solidi (a) **103**, 175–184 (1987).

[31] B. M. Askerov, *Electron transport phenomena in semiconductors* (World Scientific, 1994).

[32] F. W. Lytle, "X-ray diffractometry of low-temperature phase transformations in strontium titanate", Journal of Applied Physics **35**, 2212–2215 (1964).

[33] C. A. Kukkonen, "T^2 electrical resistivity due to electron-phonon scattering on a small cylindrical fermi surface: application to bismuth", Physical Review B **18**, 1849–1853 (1978).

[34] V. F. Gantmakher, "The experimental study of electron-phonon scattering in metals", Reports on Progress in Physics **37**, 317–362 (1974).

[35] X. Lin, B. Fauque, and K. Behnia, "Scalable T^2 resistivity in a small single-component Fermi surface", Science **349**, 945–948 (2015).

[36] J.-S. Zhou, J. B. Goodenough, and B. Dabrowski, "Pressure-induced non-Fermi-liquid behavior of $PrNiO_3$", Physical Review Letters **94**, 226602 (2005).

[37] A. Sakai, T. Kanno, S. Yotsuhashi, H. Adachi, and Y. Tokura, "Thermoelectric properties of electron-doped $KTaO_3$", Japanese Journal of Applied Physics **48**, 097002 (2009).

[38] D. Oka, Y. Hirose, S. Nakao, T. Fukumura, and T. Hasegawa, "Intrinsic high electrical conductivity of stoichiometric $SrNbO_3$ epitaxial thin films", Physical Review B **92**, 205102 (2015).

[39] I. Nagai, N. Shirakawa, S.-i. Ikeda, R. Iwasaki, H. Nishimura, and M. Kosaka, "Highest conductivity oxide $SrMoO_3$ grown by a floating-zone method under ultralow oxygen partial pressure", Applied Physics Letters **87**, 024105 (2005).

[40] D. Keroack, Y. Lepine, and J. L. Brebner, "Drift mobility measurements of small-polaron transport in $SrTiO_3$", Journal of Physics C: Solid State Physics **17**, 833–842 (1984).

[41] S. Saraf, I. Riess, and A. Rothschild, "Parallel band and hopping electron transport in $SrTiO_3$", Advanced Electronic Materials **2**, 1500368 (2016).

[42] T. Montini, M. Melchionna, M. Monai, and P. Fornasiero, "Fundamentals and catalytic applications of CeO_2-based materials", Chemical Reviews **116**, 5987–6041 (2016).

[43] W. C. Chueh and S. M. Haile, "A thermochemical study of ceria: exploiting an old material for new modes of energy conversion and CO_2 mitigation", Philosophical Transactions of the Royal Society A: Mathematical, Physical and Engineering Sciences **368**, 3269–3294 (2010).

[44] W. C. Chueh, Y. Hao, W. Jung, and S. M. Haile, "High electrochemical activity of the oxide phase in model ceria-Pt and ceria-Ni composite anodes", Nature Materials **11**, 155–161 (2011).

[45] A. J. Bosman and C. Crevecoeur, "Mechanism of the electrical conduction in li-doped NiO", Physical Review **144**, 763–770 (1966).

[46] H. Wang, C. Wang, W. Su, J. Liu, H. Peng, J. Zhang, M. Zhao, J. Li, N. Yin, and L. Mei, "Substitution effect on the thermoelectric properties of reduced Nb-doped $Sr_{0.95}La_{0.05}TiO_3$ ceramics", Journal of Alloys and Compounds **486**, 693–696 (2009).

[47] A. V. Kovalevsky, A. A. Yaremchenko, S. Populoh, P. Thiel, D. P. Fagg, A. Weidenkaff, and J. R. Frade, "Towards a high thermoelectric performance in rare-earth substituted $SrTiO_3$: effects provided by strongly-reducing sintering conditions", Physical Chemistry Chemical Physics **16**, 26946–26954 (2014).

Chapter 3

PHENOMENOLOGY IN CONDUCTING POLYMERS

In the previous chapter (Ch.2), the phenomenological characterization of transport eventually led to the identification of physical models that are consistent with the phenomenology. However, it may not always be the case that there is a relevant physical model for the material system. It might be even unrecognized in the literature that existing physical models fail to explain the reported phenomenology. It will be seen in this chapter that conducting polymers exemplify such a case [1]. Here, the phenomenological characterization method using the Seebeck-conductivity relation will help to clearly manifest the failure of models currently employed in the literature. In the absence of a proper physical model, the phenomenological model will be useful for its predictive power, which will be applied to the quality factor analysis for thermoelectrics in Ch.6.

3.1 Failure of Mott's models for conducting polymers

The unique merit of conducting polymers as "plastic semiconductors" has spurred much motivation for implementing these flexible materials into electronic applications such as transistors [2], photovoltaics [3], and thermoelectrics [4]. The field has seen exciting progress such as mobilities exceeding that of amorphous silicon [5, 6], solar cells with $\approx$ 10% conversion efficiency [7, 8], and thermoelectric figure-or-merit $zT > 0.1$ [9, 10].

The understanding for charge transport in conducting polymers, on the other hand, has not changed much fundamentally since some of the earliest ideas despite intensive research on the topic. A mechanistic understanding for conduction was naturally one of the earliest interests following the first development of doped polyacetylene [11] that exhibited an increase in conductivity by seven orders of magnitude after doping. For a charge in an isolated 1D chain (or in the limit of weak interchain coupling), localization by the formation of solitons or polarons has been highlighted in many studies [12]. For high macroscopic conductivity, preventing this 1D localization through strong interchain coupling has been considered a crucial element [13]. Structurally coherent domains, in which interchain or intermolecular coupling is strong, were thus expected to have charges delocalized and contribute to some metallic signatures [14]. In amorphous regions where such

interchain coupling is weak, charge transport has been understood with hopping models (based on Mott's variable range hopping model) describing the interchain hopping of localized charges [15]. The consistency between experiments and the variable range hopping model has been emphasized largely around one central feature: that the measured temperature dependency of conductivity is approximately $\sigma(T) \propto \exp\left[-\left(\frac{W}{k_B T}\right)^{\gamma=1/2}\right]$, with $\gamma = \frac{1}{2}$ considered as a result of hopping in polymers being different in dimensionality than silicon or germanium (for which Mott's model was originally devised [16]). In light of the variable range hopping-type $\sigma(T)$ being observed in conductivity, measurements on the Seebeck coefficients have also been typically interpreted with the variable range hopping model [14]. Further scrutiny into the model-experiment consistency has been very limited, with many studies analyzing conductivity or thermopower only separately.

Only recently has the charge transport phenomenology been revisited to unveil previously unnoticed features. Glaudell *et al.* have showed that a large number of conducting polymers exhibit a strikingly similar $S - \sigma$ relation [17]. This universal relation was not successfully explained with any of the existing transport models nowadays used for conducting polymers. A particularly interesting part of the analysis was the failure of Mott's transport models (both the variable range hopping model and mobility edge model). The astonishing aspect of the failure of Mott's models is not the failure itself, but the fact that the inability of the models has not been properly recognized for such a long time. Highlighted from such long ignorance is once again the ambiguity in interpreting $\sigma(T)$ as a signature for a particular transport mechanism, as was discussed previously in Ch.2.

The polythiophene data reported by Glaudell *et al.* are plotted in Fig.3.1, showing disagreement with Mott's models. The model fittings labeled "ME-based fitting" and "VRH" are model estimations based on Mott's mobility edge and variable range hopping models, respectively, given in the same reference; models were allowed to free-fit the data with a relaxed restriction on parameters, but nevertheless could not describe the experimental data. As an alternate way of testing the hopping picture, the $S - \sigma$ relation from a narrow transport function is also compared with data in Fig.3.1, but shows disagreement. In an earlier chapter in section 1.3, it has been discussed that a narrow transport function is associated with hopping. In fact, even for variable range hopping models, if model equations for transport are found to use the transport energy concept [16, 18, 19], the model is mathematically equivalent to a narrow transport function case.

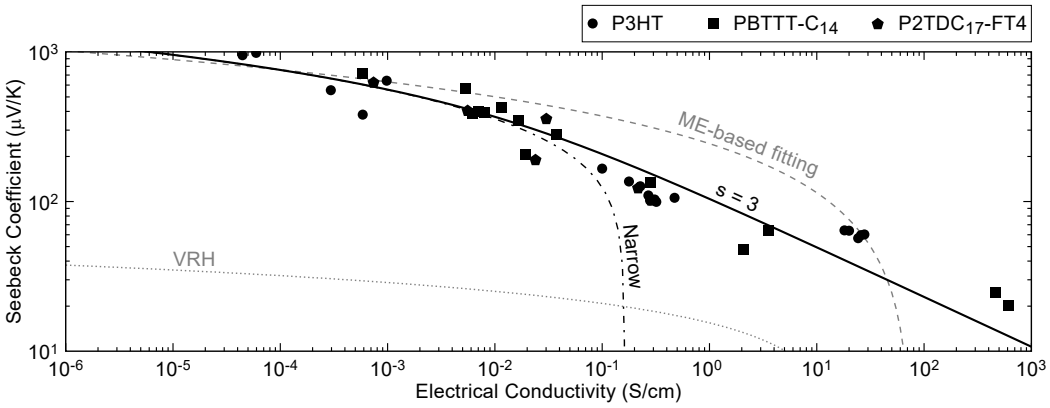

Figure 3.1: The thermopower-conductivity relation found from F4TCNQ- and FTS-doped polythiophenes at room temperature. Data are from Ref.[17]. The gray dashed line is a fitting based on the mobility edge model as presented in the same reference. The gray dotted line is an evaluation of the variable range hopping model as presented in the same reference. The black dashed-dotted line is the relation for a narrow transport function. The black solid line is the relation with a phenomenological exponent $s = 3$, showing the best fit to the data. Chemical abbreviations are listed in Table.3.1.

The best fit to the data in Fig.3.1 is found to rather be a dispersive phenomenological transport function (Eq.1.76) with an exponent $s = 3$. Hopping models do not offer an explanation for such a dispersive function.

3.2 Phenomenological characterization of conducting polymers

Not having any relevant physical model in hand, one should resort to phenomenology. A phenomenological model is established in this section, which will be used as a basis for discussing physical origins.

Transport function from temperature-dependency analysis

For gaining insight from temperature dependency, it has been shown in Ch.2 that analyzing $\sigma(T)$-$S(T)$ data pairs (*i.e.* $S(T)$ and $\sigma(T)$ from the identical sample) is much more useful than analyzing $\sigma(T)$ alone. Such experimental data are rare in the conducting polymer literature, but one study by Park reports $\sigma(T)$-$S(T)$ data pairs measured from polyacetylene [21]. In this subsection, we use polyacetylene data to establish the phenomenological model.

First interest is in the exponent s; by testing the $s = 3$ found from polythiophenes (Fig.3.1) on a literature compilation of room temperature polyacetylene data, we find that $s = 3$ also describes polyacetylene reasonably well (Fig.3.2a).

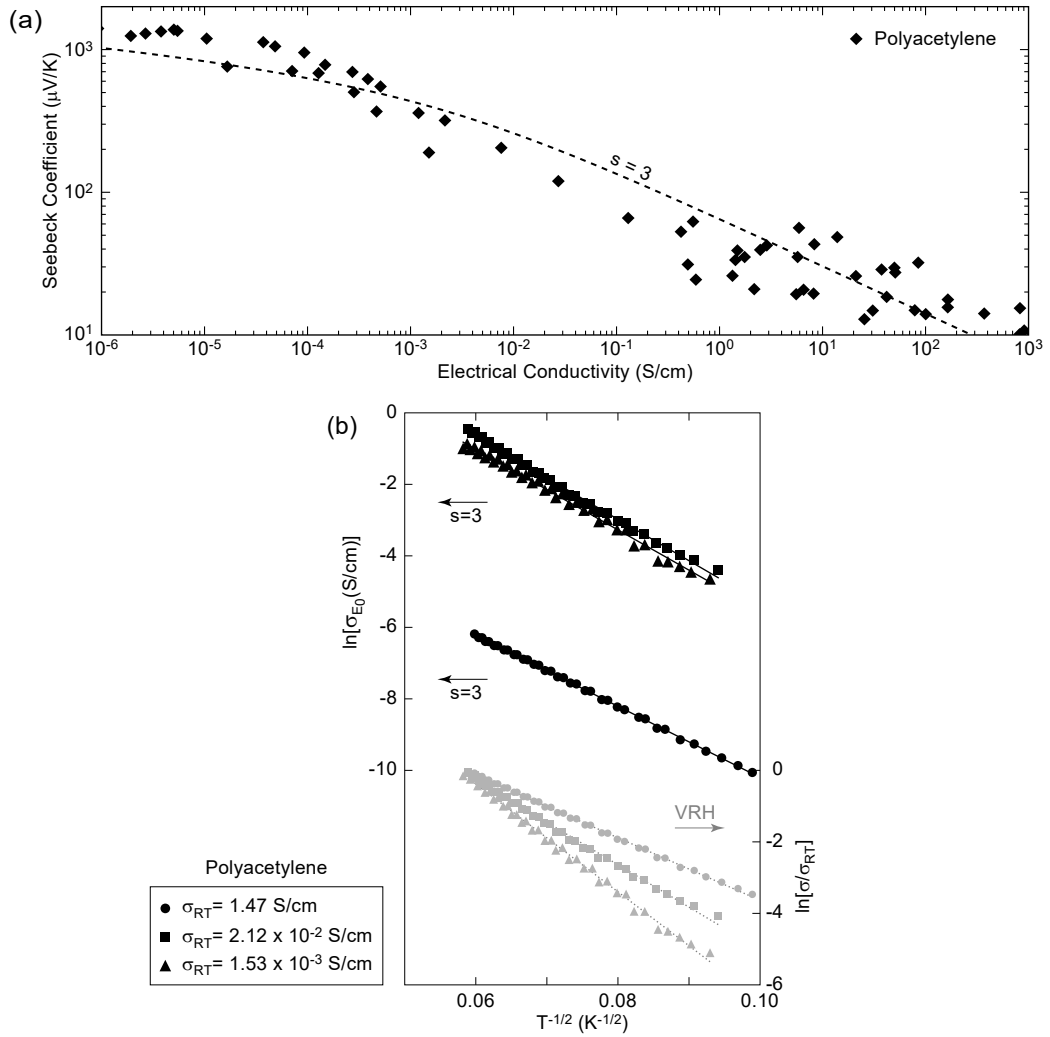

Figure 3.2: Phenomenological characterization of charge transport in polyacetylene. **(a)** Literature compilation of polyacetylene thermopower-conductivity data, as reported in Ref.[20]. The $s = 3$ transport exponent identified from polythiophenes (Fig.3.1) appears to also approximately fit the overall trend of polyacetylene. **(b)** Analysis of the temperature dependency. Using thermopower-conductivity data from three samples reported in Ref.[21], σ_{E_0} was extracted using the $s = 3$ relation and plotted (black data points; left axis). The activation energy ($W_{\frac{1}{2}} \approx 1$ eV; Eq.3.1) appears identical in all three samples despite vastly different doping levels (the slope is identical in the three black fits). By contrast, a simple variable range hopping analysis (gray data points; right axis) shows activation energies dependent on the doping level.

Then, using $s = 3$, the phenomenological coefficient σ_{E_0} (Eq.1.76) is extracted from the temperature dependent data reported in Ref.[21]. It is seen in Fig.3.2b that the coefficient is well described with the following form:

$$\sigma_{E_0}(T) = \sigma_{E_{00}} \exp\left[-\left(\frac{W_{\frac{1}{2}}}{k_{\mathrm{B}}T}\right)^{1/2}\right]. \tag{3.1}$$

Here $\sigma_{E_{00}}$ is simply an energy and temperature-independent coefficient[1]. Recall that σ_{E_0} is expected to be independent of E_{F} for a rigid transport function (see discussion in section 2.3). It is found from the identical slopes in Fig.3.2b (which indicate $W_{\frac{1}{2}}$) that this rigidity is observed within each polyacetylene sample. To ones surprise, $W_{\frac{1}{2}}$ is identical even when one of the three samples has a very different $\sigma_{E_{00}}$ value (*i.e.* not all three samples collapse onto a single line in Fig.3.2b, which means that the $s = 3$ curve corresponding to each sample in a $\log S - \log \sigma$ plot will be at a different horizontal position). Said differently, even when the transport function is not entirely rigid with respect to repeated synthesis (even when there are some "bad" samples), the samples have an identical $W_{\frac{1}{2}}$. This E_{F}-independence of $W_{\frac{1}{2}}$ suggests that the $s = 3$ description for transport is working well because it indicates that conductivity is properly "normalized" with respect to E_{F} using the S data and $s = 3$ relation. The E_{F}-independence of $W_{\frac{1}{2}}$ is also in direct contrast to the variable range hopping analysis in which conductivity is analyzed by $\sigma(T) \propto \exp\left[-\left(\frac{W_{\mathrm{VRH}}}{k_{\mathrm{B}}T}\right)^{1/2}\right]$; it is seen in Fig.3.2b that W_{VRH} is dependent on the doping level.

Combining the energy and temperature dependencies found from the analysis in 3.2, the phenomenological transport function could be expressed as

$$\begin{aligned} \sigma_E(E,T) &= \sigma_{E_{00}} \exp\left[-\left(\frac{W_{\frac{1}{2}}}{k_{\mathrm{B}}T}\right)^{1/2}\right] \cdot \left(\frac{E - E_{\mathrm{t}}}{k_{\mathrm{B}}T}\right)^3 && (E \geq E_{\mathrm{t}}) \\ &= 0. && (E < E_{\mathrm{t}}) \end{aligned} \tag{3.2}$$

Application to other conducting polymers

The resemblance between polyacetylene and polythiophenes (Figs.3.1 and 3.2) implies that the phenomenological transport model (Eq.3.2) could possibly be used to characterize a wider variety of conducting polymer samples. An extended compilation of literature data consisting of Seebeck and conductivity measurements at room

[1] It is not possible from the given data to phenomenologically determine whether $\sigma_{E_{00}}$ should weakly contribute to the temperature dependency of σ_{E_0} such as $\sigma_{E_{00}} \propto \frac{1}{T}$.

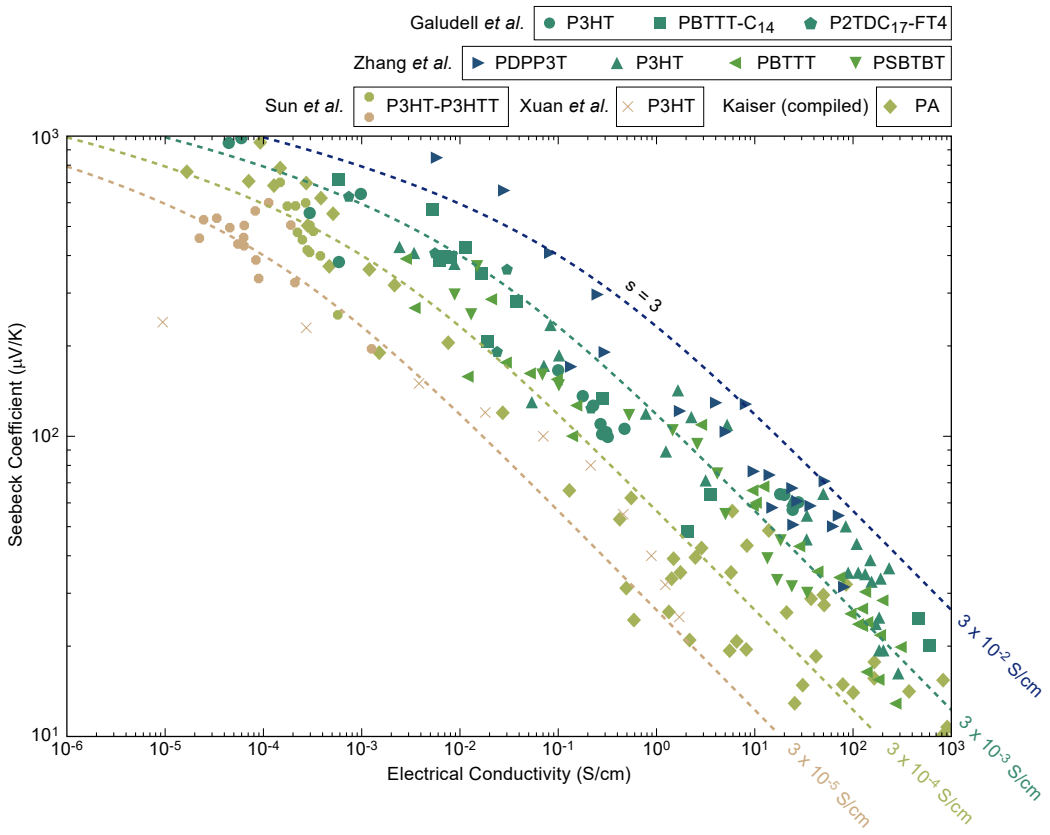

Figure 3.3: Compilation of room temperature Seebeck-conductivity data of various conducting polymers. Data are from Refs.[17, 20, 22–24]. The dashed lines show the $s = 3$ model relation with different values of σ_{E_0} as annotated on each line. As a guide to eyes, the markers are colored in accordance to the approximate value of average σ_{E_0} observed in each data set. Chemical abbreviations are listed in Table.3.1.

temperature are shown in Fig.3.3. Compared to the data is the $s = 3$ model curves with different values of $\sigma_{E_0}(T = 300\ \mathrm{K})$. It is seen that, despite significant sample variation, the overall trend in data resembles the $s = 3$ relation. It should be kept in mind that much of these experimental data were obtained from the intent of improving σ_{E_0} (which allows one to reach a higher power factor $S^2\sigma$ near the optimum doping level), rather than trying to keep σ_{E_0} constant with the intent of keeping the transport function "rigid" and facilitating mechanistic studies. A resemblance in the overall trend despite the lack of such efforts indicates that there exists a common underlying mechanism that strongly restricts, or determines, the charge transport in these conducting polymers. The $s = 3$ phenomenological transport function seems to capture this universality, suggesting that it represents, at least to leading order, the underlying mechanism that should be resolved.

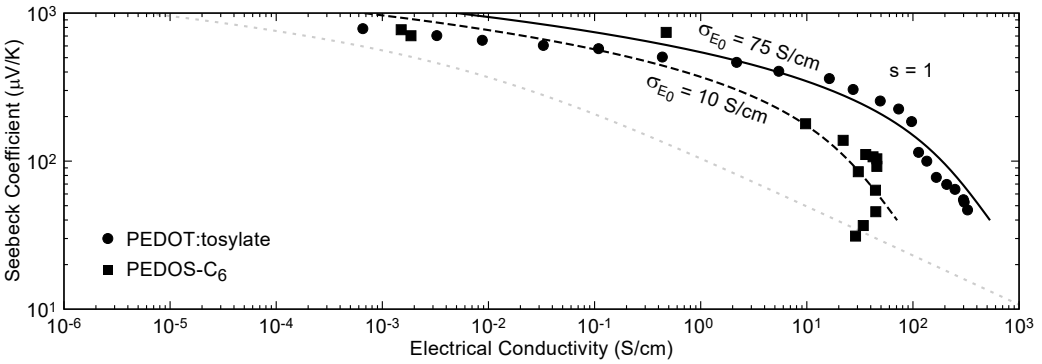

Figure 3.4: The Seebeck-conductivity relation in PEDOT:tosylate and PEDOS-C_6. Data are from Refs.[9, 25]. The black lines show the $s = 1$ model relation with different values of σ_{E_0} as annotated on each line. The $s = 3$ relation found from other polythiophenes in Fig.3.1 is plotted together (gray dotted line) for reference. Chemical abbreviations are listed in Table.3.1.

On the other hand, some variants show a clearly distinctive $S - \sigma$ relation that is better described with $s = 1$, as shown in Fig.3.4. It is interesting that these materials are also the types that generally exhibit better electric characteristics such as a higher thermoelectric power factor or field effect mobility (note that the data points in Fig.3.4 are populated on the upper right side of the reference curve for other $s = 3$ polythiophenes). Understanding these exceptional cases would help to understand the mechanism underlying $s = 1$ or 3 and possibly lead to better performing materials.

Although the phenomenology of the s exponent, by itself, does not offer a reason for its correlation to better performance in electronic applications, the phenomenology provides a curious analogical comparison to a similar case observed in inorganic materials. In band conductors, deformation potential scattering maps to the phenomenology of $s = 1$ while ionized impurity scattering maps to the phenomenology of $s = 3$ (see Table 1.1). It is generally true that, at a given temperature, band conductors dominated by deformation potential scattering are better conductors (or of higher mobility) than those governed by ionized impurity scattering. The mathematical form provided by the ionized impurity scattering or $s = 3$ might lead one to expect better conduction in such cases (conductivity increases more rapidly with E_F); however, ionized impurity scattering dominates when it is a much stronger scattering source than the deformation potential, meaning that the conductivity will only decrease from the additional influence of ionized impurity scattering.

Associated with the better conductance (for a given E_F or S) in PEDOT-based

materials is a lower activation energy. Galliani *et al.* have shown that $W_{\frac{1}{2}} \approx 0.1$ eV in PEDOT:tosylate, which is an order of magnitude lower than the 1.0 eV found from polyacetylene in Fig.3.2 [26]. Similarly low $W_{\frac{1}{2}}$ values of $0.2 - 0.3$ eV have also been found in PEDOT:PSS (although $W_{\frac{1}{2}}$ was extracted from σ rather than σ_{E_0} in this study, $W_{\frac{1}{2}}$ is expected to be similar either way in this case because of the sample most likely being in the degenerate regime) [27].

3.3 Physical interpretation of the phenomenological transport function

Although the $s = 3$ (or 1) phenomenological transport functions have some immediate usefulness as a transport model (which will be used as a basis for thermoelectric quality factor analysis in Ch.6), the ultimate goal would be to develop a physical model that is consistent with the phenomenology. Some important aspects that must be considered or further experimented will be discussed in this section.

One of the biggest questions is why a homogeneous transport function is sufficiently effective in describing such inherently inhomogeneous materials like conducting polymers. The inhomogeneous microstructure has been studied extensively in the recent literature [28–31] revealing locally ordered domains as small as < 10 nm embedded in an amorphous matrix with varying degrees and types of disorder. Although inhomogeneity does not necessary make it impossible for a homogeneous transport function to be an effective description (*e.g.* use of Matthiessen's rule to combine different scattering mechanisms is a homogeneous approach but is often used to described inhomogeneous features such as grain boundaries [32, 33]), the high resistivity and volume fraction of the amorphous region renders a regime in which the effective homogeneous function typically breaks down (this topic will be the focus of Ch.4).

Another feature that requires a physical explanation is the (phenomenological) presence of a transport edge. The large thermopowers observed in conducting polymers cannot be explained without presuming that there should be a transport edge. However, those materials with large thermopower can be doped to have such a small thermopower ("metallic" values) while retaining the thermally activated conduction behavior. From studies on homogeneously disordered amorphous materials like silicon, it is known that the band edges are smeared out due to disorder. Instead of a band edge, there could exist a mobility edge that sharply delineates the localized and extended states. Moving E_{F} above the mobility edge (Anderson transition), however, is supposed to accompany a change in the thermally activated conduction

behavior as well. The coexistence of metallic thermopower and thermally activated conduction has generally been attributed to inhomogeneity, but the physical origin of a transport edge (or even the existence of one) has not been bought to attention in the literature.

One explanation that could be conceived in the context of the inhomogeneous microstructure is that the $s = 3$ phenomenology reflects the inhomogeneity itself; *i.e.* the character of the inhomogeneous microstructure could be the origin of such a power-law transport function, as in percolation networks. Classically, the power law in percolative microstructures is more often discussed in terms of volume fraction, because the power law has been heavily studied from experiments on metal-embedded dielectric media with varying metal volume fractions [34–36]. Such a power law in volume fraction implies a power law also for energy, which can be illustrated with the approach illustrated by Eggarter [37]. Suppose that the space in a media can be divided into allowed and disallowed volumes for each particle. This division will depend on the potential landscape of the media and the energy of the particle. If the volume fraction V allowed at for a particle with energy E is defined as $c(E)$, this function will be a monotonically increasing function with energy [37]. At a critical energy E_c, $c(E_c)$ will be such that particles can transport across the media effectively (delocalized). This E_c is referred to as the percolation edge, and $c(E_c)$ is the critical volume fraction V_c. Now, assume that conductivity is empirically observed to be $\sigma(V) \propto (V - V_c)^\alpha$. Then, for a metal inclusion with $E_F = E_c$, one could infer that $\sigma(E) \propto [c(E) - c(E_c)]^\alpha$. If $c(E)$ is expanded around E_c, the leading order term in the expansion $c \propto (E - E_c)^\beta$ would yield an exponent $s \approx \alpha\beta$ above the percolation edge. This argument offers a possible explanation for both a power-law relation and also the origin of the transport edge as a percolation edge.

The temperature dependence of the phenomenological function does also suggest a connection to percolation, but with a difficulty in interpreting the transport edge. What is most interesting is that the temperature dependency of the type $\exp\left[-\left(\frac{W}{k_B T}\right)^{1/2}\right]$ observed in conducting polymers is also observed similarly[2] in classical percolation system, such as Ni-SiO_2, W-Al_2O_3 and many more [34–36]. However, in those metal-dielectric percolation systems, the thermally activated behavior disappears as the volume fraction reaches the critical percolation volume,

[2] Another lesson here is that the power-exponential dependency in temperature should be understood to have a broader implication than just variable range hopping.

which is in contrast to the conducting polymer system where the activation behavior persists above the transport edge. Because of this inconsistency, the transport edge is not fully explained with a percolation edge.

The difficulty of the percolation edge concept in simultaneously explaining the transport edge and temperature dependency suggests that the transport edge and $s = 3$ could be of different origin. It is feasible in many aspects to suppose that the transport edge (and at least part of the $s = 3$) originate from the ordered domains within the conducting polymer. Above all, such a dispersive transport function above an edge is naturally explained from an ordered phase with delocalized wave functions. It is also generally true that the phenomenological transport character is determined by the conductive phase while the magnitude of conductivity is limited by the non-conductive phase[3] (a detailed example case will be discussed with Mg_3Sb_2 in Ch.4). A number of studies also show how the relatively ordered domains control a number of transport related phenomena such as electroluminescence [28], microwave conductivity [39], or local conductivity [30].

If the ordered domains are assumed to be responsible for the transport edge, the $\exp\left[-\left(\frac{W}{k_B T}\right)^{1/2}\right]$ should be attributed to the system being below the percolation edge (or, equivalently, the ordered domain volume fraction being below the critical percolation volume). $W_{\frac{1}{2}}$ remaining constant regardless of doping and finite even at $E_F > E_t$ (Fig.3.2) are then both consistent with the assumption.

In summary of the most probable physical explanation based on the discussion so far, the transport edge seems to originate from the ordered domains that should also provide a dispersive transport function. The overall system is limited by being below the percolation threshold which dominates the temperature dependency. The phenomenological transport function in Eq.3.2 should be an approximate form that combines the effect of ordered domains and a percolation network.

Carefully designed experiments could provide much insight in furthering the understanding. The most direct experiment would be to measure the $S - \sigma$ relation locally from ordered domains. The small structural coherence length scale of conducting polymers make this experiment a challenging one. Use of scanning probes [29, 30, 40] or nano-patterned electrodes could be a good strategy to overcome experimental challenges. Development of films with larger ordered domains would make it easier to probe local transport properties.

[3] When far from the threshold in a percolation system, effective medium theory is a reasonable framework for describing an inhomogeneous system [38].

3.4 Appendix: Chemical abbreviations

Table 3.1: Abbreviations for chemical formulae used in the current chapater

Abbreviation	Chemical formula
PA	polyacetylene
P3HT	poly(3-hexylthiophene)
P3HTT	poly(3-hexylthiothiophene)
PBTTT-C_{14}	poly(2,5-bis(3-tetradecylthiophen2-yl)thieno[3,2-b]thiophene)
P2TDC$_{17}$-FT4	poly(2,5-bis(thiphen-2-yl)-(3,7-diheptadecantyltetrathienoacene))
F4TCNQ	tetrafluorotetracyanoquinodimethane
FTS	alkyl silane (tridecafluoro-1,1,2,2,-tetrahydrooctyl)-trichlorosilane
PDPP3T	poly[2,5-bis(2-hexyldecyl)-2,3,5,6-tetrahydro-3,6 -dioxopyrrolo[3,4-c]pyrrole-1,4-diyl-*alt* -[2,2′:5′,2″-terthiophene]-5,5″-diyl
PSBTBT	poly[(4,4′-bis(2-ethylhexyl)dithieno[3,2-b:2′,3′-d]silole)-2,6-diyl -*alt*-(2,1,3-benzothiadiazole)-4,7-diyl]
PEDOT	poly(3,4-ethylenedioxythiophene)
PEDOS-C_6	poly(hexyl-3,4-ethyl-enedioxyselenophene)

References

[1] S. D. Kang and G. J. Snyder, "Charge-transport model for conducting polymers", Nature Materials **16**, 252–257 (2017) 10.1038/nmat4784.

[2] H. Sirringhaus, T. Kawase, R. H. Friend, T. Shimoda, M. Inbasekaran, W. Wu, and E. P. Woo, "High-resolution inkjet printing of all-polymer transistor circuits", Science **290**, 2123–2126 (2000).

[3] L. Lu, T. Zheng, Q. Wu, A. M. Schneider, D. Zhao, and L. Yu, "Recent advances in bulk heterojunction polymer solar cells", Chemical Reviews **115**, 12666–12731 (2015).

[4] D. Beretta, A. Perego, G. Lanzani, and M. Caironi, "Organic flexible thermoelectric generators: from modeling, a roadmap towards applications", Sustainable Energy & Fuels **1**, 174–190 (2017).

[5] D. Venkateshvaran, M. Nikolka, A. Sadhanala, V. Lemaur, M. Zelazny, M. Kepa, M. Hurhangee, A. J. Kronemeijer, V. Pecunia, I. Nasrallah, I. Romanov, K. Broch, I. McCulloch, D. Emin, Y. Olivier, J. Cornil, D. Beljonne, and H. Sirringhaus, "Approaching disorder-free transport in high-mobility conjugated polymers", Nature **515**, 384–388 (2014).

[6] K. Kang, S. Watanabe, K. Broch, A. Sepe, A. Brown, I. Nasrallah, M. Nikolka, Z. Fei, M. Heeney, D. Matsumoto, K. Marumoto, H. Tanaka, S.-i. Kuroda, and H. Sirringhaus, "2D coherent charge transport in highly ordered conduct-

ing polymers doped by solid state diffusion", Nature Materials **15**, 896–902 (2016).

[7] J. You, L. Dou, K. Yoshimura, T. Kato, K. Ohya, T. Moriarty, K. Emery, C.-C. Chen, J. Gao, G. Li, and Y. Yang, "A polymer tandem solar cell with 10.6% power conversion efficiency", Nature Communications **4**, 1446 (2013).

[8] Z. He, B. Xiao, F. Liu, H. Wu, Y. Yang, S. Xiao, C. Wang, T. P. Russell, and Y. Cao, "Single-junction polymer solar cells with high efficiency and photovoltage", Nature Photonics **9**, 174–179 (2015).

[9] O. Bubnova, Z. U. Khan, A. Malti, S. Braun, M. Fahlman, M. Berggren, and X. Crispin, "Optimization of the thermoelectric figure of merit in the conducting polymer poly(3,4-ethylenedioxythiophene)", Nature Materials **10**, 429–433 (2011).

[10] G.-H. Kim, L. Shao, K. Zhang, and K. P. Pipe, "Engineered doping of organic semiconductors for enhanced thermoelectric efficiency", Nature Materials **12**, 719–723 (2013).

[11] H. Shirakawa, E. J. Louis, A. G. MacDiarmid, C. K. Chiang, and A. J. Heeger, "Synthesis of electrically conducting organic polymers: halogen derivatives of polyacetylene, $(CH)_x$", Journal of the Chemical Society, Chemical Communications, 578 (1977).

[12] A. J. Heeger, "Nobel lecture: semiconducting and metallic polymers: the fourth generation of polymeric materials", Reviews of Modern Physics **73**, 681–700 (2001).

[13] S. Kivelson and A. Heeger, "Intrinsic conductivity of conducting polymers", Synthetic Metals **22**, 371–384 (1988).

[14] Z. H. Wang, C. Li, E. M. Scherr, A. G. MacDiarmid, and A. J. Epstein, "Three dimensionality of "metallic" states in conducting polymers: polyaniline", Physical Review Letters **66**, 1745–1748 (1991).

[15] A. Epstein, W.-P. Lee, and V. Prigodin, "Low-dimensional variable range hopping in conducting polymers", Synthetic Metals **117**, 9–13 (2001).

[16] N. F. Mott and E. A. Davis, *Electronic processes in non-crystalline materials*, 2nd ed. (Oxford University Press, 1979).

[17] A. M. Glaudell, J. E. Cochran, S. N. Patel, and M. L. Chabinyc, "Impact of the doping method on conductivity and thermopower in semiconducting polythiophenes", Advanced Energy Materials **5**, 1401072 (2015).

[18] R. Schmechel and H. von Seggern, "Electronic traps in organic transport layers", physica status solidi (a) **201**, 1215–1235 (2004).

[19] J. Bisquert, "Interpretation of electron diffusion coefficient in organic and inorganic semiconductors with broad distributions of states", Physical Chemistry Chemical Physics **10**, 3175 (2008).

[20] A. B. Kaiser, "Electronic transport properties of conducting polymers and carbon nanotubes", Reports on Progress in Physics **64**, 1 (2001).

[21] Y. W. Park, "Structure and morphology: relation to thermopower properties of conductive polymers", Synthetic Metals **45**, 173–182 (1991).

[22] Q. Zhang, Y. Sun, W. Xu, and D. Zhu, "What to expect from conducting polymers on the playground of thermoelectricity: lessons learned from four high-mobility polymeric semiconductors", Macromolecules **47**, 609–615 (2014).

[23] J. Sun, M. L. Yeh, B. J. Jung, B. Zhang, J. Feser, A. Majumdar, and H. E. Katz, "Simultaneous increase in Seebeck coefficient and conductivity in a doped poly(alkylthiophene) blend with defined density of states", Macromolecules **43**, 2897–2903 (2010).

[24] Y. Xuan, X. Liu, S. Desbief, P. Leclere, M. Fahlman, R. Lazzaroni, M. Berggren, J. Cornil, D. Emin, and X. Crispin, "Thermoelectric properties of conducting polymers: the case of poly(3-hexylthiophene)", Physical Review B **82**, 115454 (2010).

[25] B. Kim, H. Shin, T. Park, H. Lim, and E. Kim, "Nir-sensitive poly(3,4-ethylenedioxyselenophene) derivatives for transparent photo-thermo-electric converters", Advanced Materials **25**, 5483–5489 (2013).

[26] D. Galliani, S. Battiston, R. Ruffo, S. Trabattoni, and D. Narducci, "Modulation of charge transport properties in poly(3,4-ethylenedioxythiophene) nanocomposites for thermoelectric applications", Journal of Physics D: Applied Physics **51**, 034002 (2017).

[27] A. M. Nardes, R. A. J. Janssen, and M. Kemerink, "A morphological model for the solvent-enhanced conductivity of PEDOT:PSS thin films", Advanced Functional Materials **18**, 865–871 (2008).

[28] R. Noriega, J. Rivnay, K. Vandewal, F. P. V. Koch, N. Stingelin, P. Smith, M. F. Toney, and A. Salleo, "A general relationship between disorder, aggregation and charge transport in conjugated polymers", Nature Materials **12**, 1038–1044 (2013).

[29] K. D. O'Neil, B. Shaw, and O. A. Semenikhin, "On the origin of mesoscopic inhomogeneity of conducting polymers", The Journal of Physical Chemistry B **111**, 9253–9269 (2007).

[30] C.-G. Wu and S.-S. Chang, "Nanoscale measurements of conducting domains and current-voltage characteristics of chemically deposited polyaniline films", The Journal of Physical Chemistry B **109**, 825–832 (2005).

[31] D. T. Duong, V. Ho, Z. Shang, S. Mollinger, S. C. Mannsfeld, J. Dacuña, M. F. Toney, R. Segalman, and A. Salleo, "Mechanism of crystallization and implications for charge transport in poly(3-ethylhexylthiophene) thin films", Advanced Functional Materials **24**, 4515–4521 (2014).

[32] A. F. Mayadas and M. Shatzkes, "Electrical-resistivity model for polycrystalline films: the case of arbitrary reflection at external surfaces", Physical Review B **1**, 1382–1389 (1970).

[33] W. Steinhögl, G. Schindler, G. Steinlesberger, and M. Engelhardt, "Size-dependent resistivity of metallic wires in the mesoscopic range", Physical Review B **66**, 075414 (2002).

[34] B. Abeles, H. L. Pinch, and J. I. Gittleman, "Percolation conductivity in W-Al_2O_3 granular metal films", Physical Review Letters **35**, 247–250 (1975).

[35] P. Sheng, B. Abeles, and Y. Arie, "Hopping conductivity in granular metals", Physical Review Letters **31**, 44–47 (1973).

[36] B. Abeles, P. Sheng, M. Coutts, and Y. Arie, "Structural and electrical properties of granular metal films", Advances in Physics **24**, 407–461 (1975).

[37] T. P. Eggarter, "Semiclassical theory of electron transport properties in a disordered material", Physical Review A **5**, 2496–2509 (1972).

[38] S. Kirkpatrick, "Percolation and conduction", Reviews of Modern Physics **45**, 574–588 (1973).

[39] A. Epstein, J. Joo, R. Kohlman, G. Du, A. MacDiarmid, E. Oh, Y. Min, J. Tsukamoto, H. Kaneko, and J. Pouget, "Inhomogeneous disorder and the modified Drude metallic state of conducting polymers", Synthetic Metals **65**, 149–157 (1994).

[40] S. Cho, S. D. Kang, W. Kim, E.-S. Lee, S.-J. Woo, K.-J. Kong, I. Kim, H.-D. Kim, T. Zhang, J. A. Stroscio, Y.-H. Kim, and H.-K. Lyeo, "Thermoelectric imaging of structural disorder in epitaxial graphene", Nature Materials **12**, 913–918 (2013).

Chapter 4

INHOMOGENEOUS TRANSPORT: Mg_3Sb_2

It has been discussed how the transport equations used so far assume a homogeneous transport function for the material system. In the conducting polymer case (Ch.3), this assumption was one of the puzzling factors due to the highly inhomogeneous microstructure of conducting polymers that is evident from structure characterization studies. In oxides (Ch.2), this complication was avoided by analyzing data measured from single crystals. Then, exactly how does the homogeneous transport function approach breakdown? What are the pitfalls that could lead to erroneous conclusions? The answers to these questions are very well illustrated by the transport properties observed in Mg_3Sb_2-based polycrystalline materials [1, 2].

4.1 Erroneous interpretation of the thermally activated conduction

The majority of the polycrystalline Mg_3Sb_2-based samples reported in the literature exhibit thermally activated conduction, even when heavily doped. Both variable range hopping [5] and ionized impurity scattering-dominated band transport [3, 4, 6] have been suggested as the cause for this thermally activated behavior. Due to the lack of any reports on heavily doped single crystals, determining the validity of those suggestions requires analysis of the transport properties rather than a simple experimental comparison. The $S - \sigma$ relation will once again help to show that the simple suggestions based on $\sigma(T)$ are inconsistent with the phenomenology of the transport function.

The thermally activated conduction in n-type $Mg_{3+\delta}Sb_{1.5}Bi_{0.5}$ and $Mg_{3+\delta}Sb_2$ samples doped with various amounts of Te (on the Sb/Bi site) is shown in Fig.4.1, where $\mu_H \propto T^n$ and also $\sigma(T) \propto T^n$ with $n \approx 1.5$ is observed near room temperature. This behavior has been the basis of an ionized impurity scattering argument because it is customary to associate a $T^{1.5}$ mobility with such a scattering mechanism; the crossover in temperature dependence has been attributed to a crossover to acoustic phonon scattering [3, 4, 6]. Some insight can be gained by reviewing where this $T^{1.5}$ argument originates from. The Drude mobility in band conductors was derived

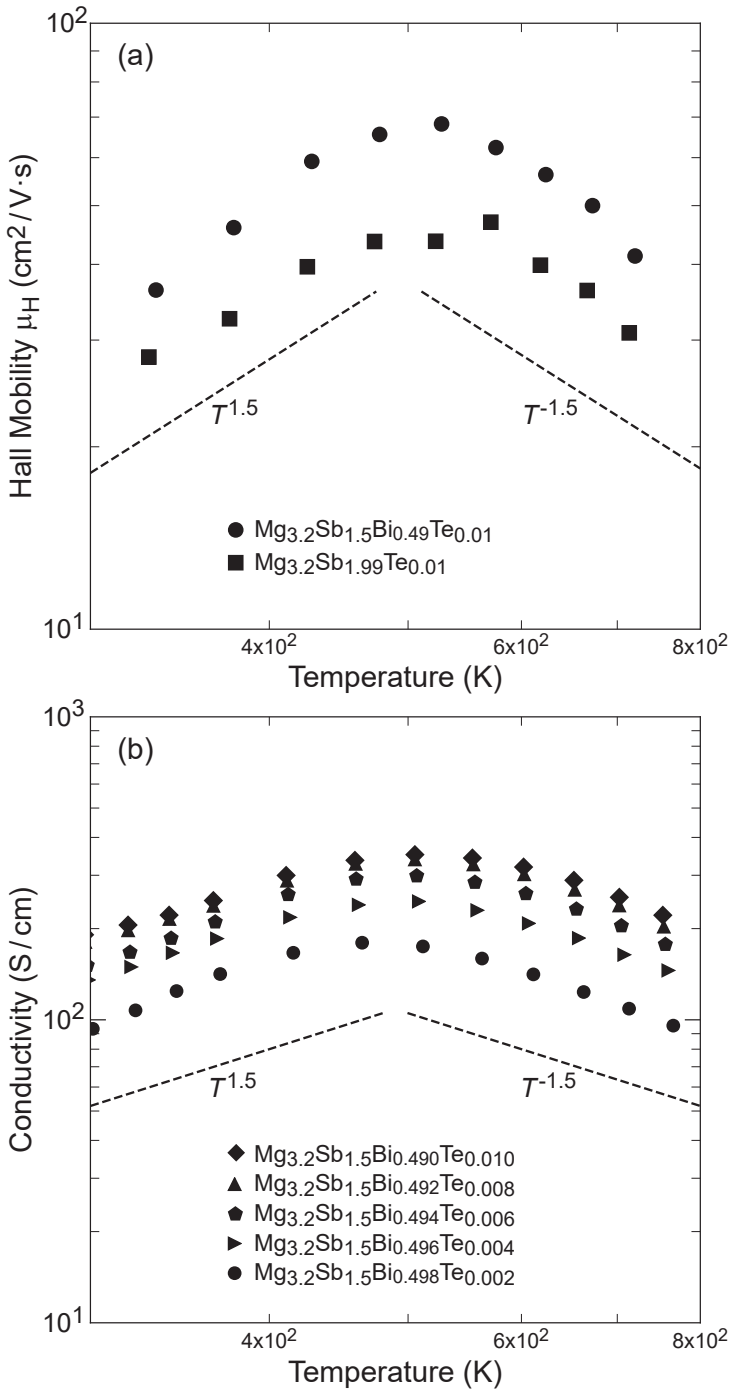

Figure 4.1: Temperature dependent properties of n-type Mg_3Sb_2-based compounds: **(a)** Hall mobility (data from Ref.[3]); **(b)** Conductivity (data from Ref.[4]).

in Eq.1.60. In the non-degenerate limit, the equation reduces to

$$\mu_{\mathrm{d}} = \frac{2}{3}\frac{e\tau_0(T)}{m_{\mathrm{b}}^*} \cdot \frac{\left(r+\frac{3}{2}\right)\Gamma(r+\frac{3}{2})}{\Gamma(\frac{3}{2})}. \qquad (\eta \ll -1) \tag{4.1}$$

By recalling the form of $\tau_0(T)$ from Table 1.1, μ_{d} becomes $T^{1.5}$ for ionized impurity scattering and $T^{-1.5}$ for deformation potential scattering in the non-degenerate limit. Because the temperature dependency of $r_{\mathrm{H}}(T)$ is weak, $\mu_{\mathrm{H}} = r_{\mathrm{H}}\mu_{\mathrm{d}}$ also follows a similar temperature dependency. In systems where carrier concentration is fixed (no bipolar excitation), conductivity will also follow a similar temperature dependency as μ_{d}. In the degenerate limit, the temperature dependency is different:

$$\mu_{\mathrm{d}} = \frac{e\tau_0(T)}{m_{\mathrm{b}}^*} \cdot \left(\frac{E_{\mathrm{F}}}{k_{\mathrm{B}}T}\right)^r. \qquad (\eta \gg 1) \tag{4.2}$$

It is seen that μ_{d} becomes temperature-independent for ionized impurity scattering and T^{-1} for deformation potential scattering. Because samples investigated for thermoelectrics usually have doping levels in between the two limits (small $|\eta|$), as is the case in Fig.4.1 as well, a temperature exponent n in the range of $0 < n < 1.5$ and $-1.5 < n < -1$ is customarily associated with ionized impurity scattering and deformation potential scattering, respectively.

Numerous literature cases have been discussed in the previous chapters where a simple analysis of the temperature dependency misled to erroneous conclusions about transport. Using a similar approach as previous cases, the $S - \sigma$ relation in Fig.4.2 clearly shows that ionized impurity scattering fails to explain the experimental data. The usefulness of investigating the $S - \sigma$ relation is once again demonstrated here: the ability to test previous hypotheses based on temperature dependencies by simply plotting data that was already reported in the original report.

An interesting feature found in Fig.4.2 is that the $S - \sigma$ relation at 550 K is virtually identical to that observed at 330 K, within experimental resolution. This similarity indicates that the phenomenological energy-dependency of the transport function is similar. However, the temperature dependencies at those two temperatures are completely opposite, as see in Fig.4.1. None of the physical models discussed so far simultaneously explain the energy and temperature dependency of the 330 K data, nor do any of them offer a good explanation for the crossover behavior. It is evident that a different physical model is required to describe this material system.

A key experimental observation [2] sheds light on this puzzling situation: it has been shown that the thermal activation behavior can be greatly mitigated by increasing

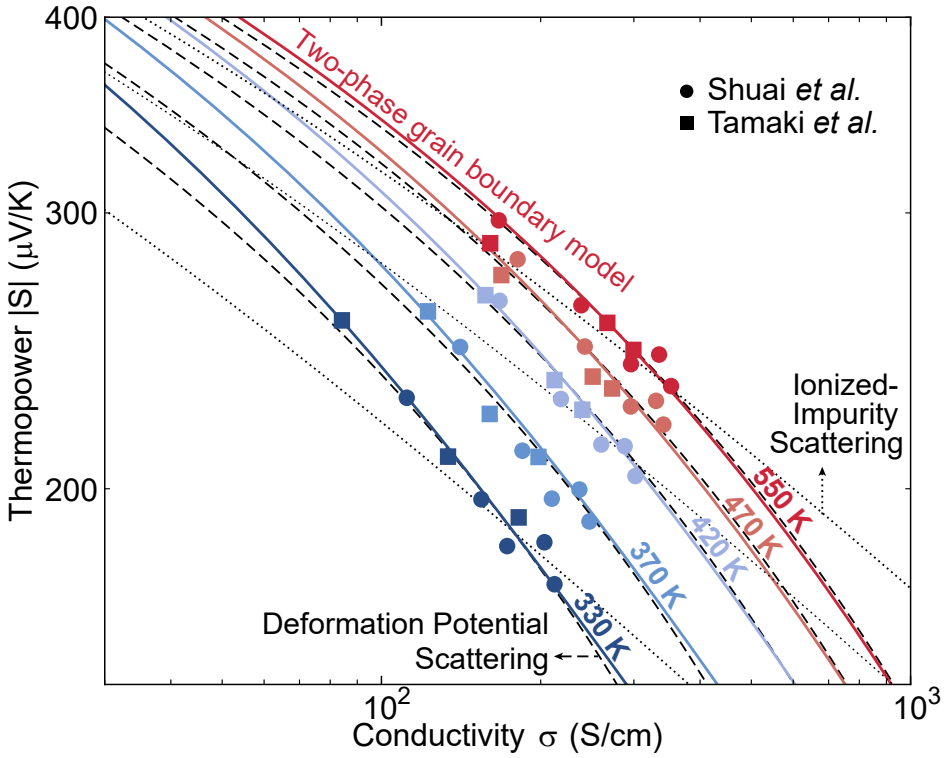

Figure 4.2: The $S - \sigma$ relation in n-type $Mg_{3+\delta}Sb_{1.5}Bi_{0.5}$ polycrystalline samples doped with various amounts of Te. The $S - \sigma$ relation for deformation potential scattering (dashed line) and ionized impurity scattering (dotted line) are drawn together for comparison. The data at each temperature show a relation that better resembles deformation potential scattering rather than ionized impurity scattering. The two-phase grain boundary model is shown to well describe the data at both low and high temperatures. Data are from Refs.[3, 4]. Regions of bipolar conduction were excluded from the plot and analysis.

the grain size (*i.e.* by decreasing the grain boundary density). After the grain size was increased by a factor of eight (average size from 1 to 8 μm), the temperature dependent conductivity became a monotonically decreasing function with respect to temperature and the 300 K conductivity increased by more than four-fold. This observation once again falsifies the previous suggestions about ionized impurity scattering. Furthermore, it hints that the proper physical model for polycrystalline Mg_3Sb_2 should address the grain boundary resistance.

4.2 Limitations in the homogeneous approach

In conventional grain boundary transport models such as those for classical metals [7, 8], the grain boundary contribution to resistance is treated by using Matthiessen's

rule on the carrier scattering rate such as

$$\tau^{-1} = \sum_{\text{processes}} \tau_i^{-1}. \tag{4.3}$$

The assumption in this approach is that the scattering processes are independent and also that they are homogeneously probable in space. The justification for using this approach for grain boundaries is that the grain boundary region is physically small enough to be approximated as a homogeneous system, just as defects or impurities are modeled. The approach has been applied not just to metals but also for doped silicon semiconductors such as SiGe [9]. Use of this approach allows one to model the transport system with a homogeneous transport function.

Use of this homogeneous approach for Mg_3Sb_2-based materials, however, faces challenges both physically and mathematically. Physically, it is questionable whether the grain boundary region is small enough in doped semiconductors like Mg_3Sb_2. Unlike classical metals such as Cu or Al, charge screening is not as effective in semiconductors. In the extreme case of insulators, the grain boundary region is known to have an influence in the electronic structure over a length scale large enough (much larger than what the atomic structure length scale might suggest) that it must be modeled as a separate phase [10]. Since the charge transfer due to grain boundaries is a generic phenomenon, a similar issue is of concern in semiconductors [11, 12], although to a lesser extent than insulators. The physical extension of the grain boundary-induced space charge region is estimated to be around 10 nm in Mg_3Sb_2 based on the calculation scheme described in Ref.[11]. This length scale is comparable to the electron mean free path in Mg_3Sb_2. For example, a mobility of $< 50\ \mathrm{cm}^2/V \cdot s$, Fermi velocity of $10^6\ \mathrm{m}/s$, and an effective mass of $0.3\mathrm{m_e}$ [13, 14] yield a mean free path of < 8 nm. This comparison suggests that treating the grain boundary simply as a scattering source could be irrelevant.

The mathematical challenge is that a homogeneous function built from mixing scattering mechanisms cannot produce a crossover in the temperature dependency as sharp as that shown in Fig.4.1; in addition, keeping the energy-dependency consistent before and after the crossover is even more prohibitive. The inability to produce a crossover can be illustrated most easily using an imaginary Drude model system in which the temperature dependency of μ_d is simply identical to that of $\tau(T)$ (although this is not true in the semiclassical model, even in the non-degenerate limit, as shown in Eq.4.1, we make this assumption for simplicity; the conclusion is not affected). In this Drude model system two scattering mechanisms are combined

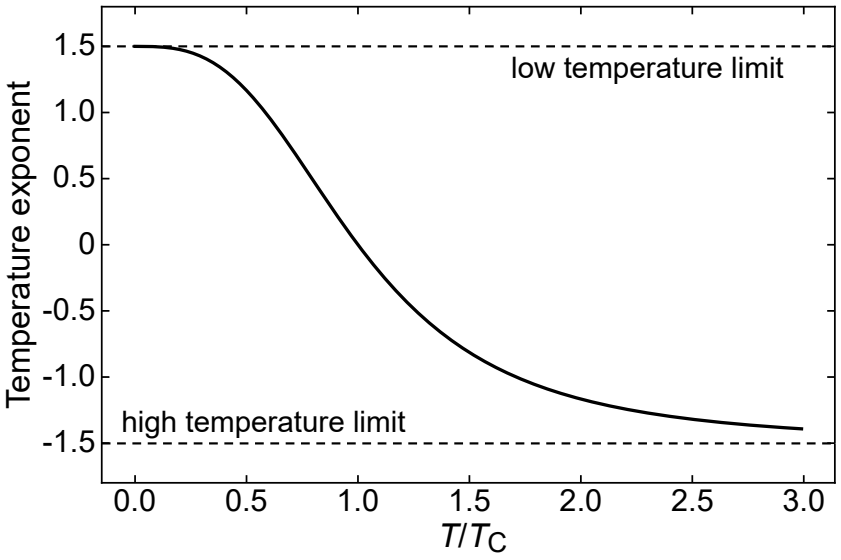

Figure 4.3: Crossover behavior in the temperature exponent with respect to temperature (normalized with the crossover temperature) as described in Eq.4.6. The crossover is gradual with respect to the normalized temperature.

to describe the temperature dependencies in the low and high temperature limits:

$$\tau^{-1} = \tau_{\mathrm{LT}}^{-1} + \tau_{\mathrm{HT}}^{-1}. \tag{4.4}$$

Here, $\tau_{\mathrm{LT}} \propto T^{3/2}$ and $\tau_{\mathrm{HT}} \propto T^{-3/2}$ dominate the temperature dependencies at low and high temperature, respectively (in the semiclassical model, it would be τ_0's rather than τ). For a crossover in temperature dependency to exist, there must be a crossover temperature T_{C} at which the two scattering mechanisms have identical rates:

$$\tau_{\mathrm{LT}}(T_{\mathrm{C}}) = \tau_{\mathrm{HT}}(T_{\mathrm{C}}). \tag{4.5}$$

Then the power exponent of the temperature dependency can be written in terms of T/T_{C}:

$$\frac{d\log\tau}{d\log T} = \frac{3}{2} - \frac{3(T/T_{\mathrm{C}})^3}{1+(T/T_{\mathrm{C}})^3}. \tag{4.6}$$

This equation is plotted in Fig.4.3, where it is seen that the crossover happens gradually. For a crossover temperature of 500 K, the transition would have to happen from about 250 K to 1000 K rather than a drastic change as seen in Fig.4.1. Now coming back to the semiclassical model, recall that τ_{LT} and τ_{HT} would actually have energy dependencies that are different with each other. Accordingly, a crossover temperature would have to also accompany a change in the phenomenological exponent s. It can therefore be concluded that a homogeneous transport function is mathematically not viable for describing the behavior in Mg_3Sb_2,

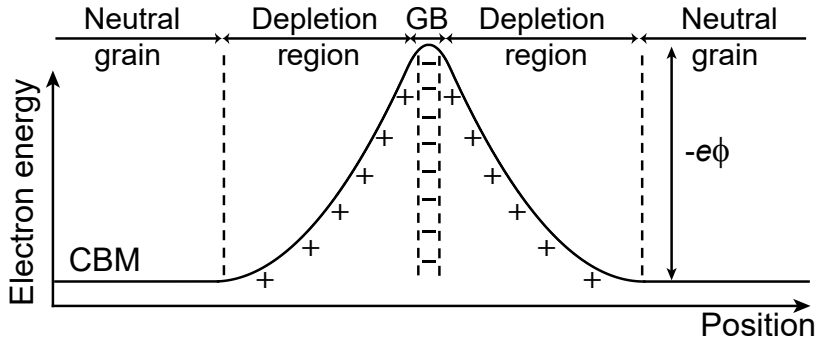

Figure 4.4: Schematic potential landscape for an electron across a grain boundary when grain boundary-induced charge transfer produces a potential barrier and associated charge depletion regions. The conduction band minimum is indicated as CBM and the potential barrier height is represented as $-e\phi$.

Use of Matthiessen's rule on mobility such as $\mu^{-1} = \sum \mu_i^{-1}$ [15–17] suffers from similar problems. An additional issue in this approach is that it fails to take into account the different energy dependencies of each scattering mechanism.

4.3 Mg_3Sb_2 modeled with an inhomogeneous approach

The limitations of a homogeneous transport function approach for polycrystalline Mg_3Sb_2 has been explained in the previous chapter. Unlike the $SrTiO_3$ or Ce_2O examples discussed in Ch.2 where such problems were avoided by analyzing single crystal data, Mg_3Sb_2 is a case where technological interest is actually in the polycrystalline form for its strong merits as a mid-temperature n-type thermoelectric material [2, 3, 18] (not many material options exist for a n-type thermoelectrics at $< 600K$). In this section, the simplest form of an inhomogeneous model (a two phase model) is developed to describe the transport in n-type polycrystalline Mg_3Sb_2-based materials.

Developing the model

The effect of grain boundaries on the electronic structure is generally understood in terms of a charge transfer between the grain and grain boundary that results in either a potential barrier or valley across the grain boundary [11, 12, 19, 20]. The occurrence of charge transfer is a generic phenomenon because any type of lattice mismatch, defects, or impurities will always result in a different electronic structure and work function, causing charge transfer in order to maintain an equilibrated Fermi-level across the material. Grain boundaries especially become a resistant

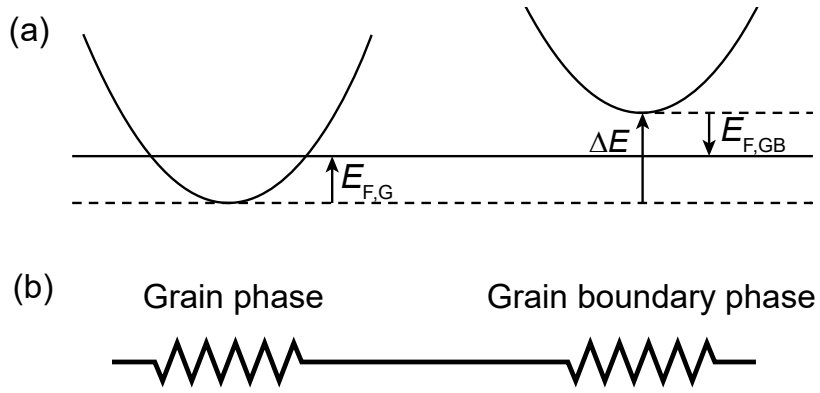

Figure 4.5: The simplified two phase grain boundary transport model. **(a)** An effective band offset of ΔE takes into account the potential barrier. This offset relates the Fermi-level of each phase (defined relative to the band edge of each phase). **(b)** A series circuit representation of the two phase model, which is equivalent to the core-shell effective medium model in the limit of a small grain boundary phase relative to the grain phase.

part of the sample when a potential barrier (rather than a valley) develops. Fig.4.4 illustrates such a potential barrier.

The exact shape, barrier height, and extent of the potential barrier has been modeled in many ways in the literature [11], and those models generally requires numerous physical parameters that cannot be determined easily and independently. Developing an inhomogeneous transport model based on those detailed models obviously results in an overfitting situation.

The approach that is the simplest (*i.e.* least number of parameters) while still being able to capture the most essential feature – the potential barrier – is to model the system with only two phases: one that represents the grain and the other that represents the grain boundary region with an effective and constant band energy offset, as illustrated in Fig.4.5a. The two model phases are simply referred to as the "grain phase" and the "grain boundary" phase. The transport properties of each model phase will be determined with their own transport function.

Since the model contains two separate phases, the overall transport properties must be determined from the properties of each model phase, for which effective medium theory can be used. The effective medium theory for a core-shell geometry (Hashin-Shtrikman microstructure [21]) should be relevant for grain-grain boundary geometry. Properties of this type of effective medium can be solved by using equations given by Bergman *et al.* [22, 23]. It can be shown that, in the limit of small grain

boundary phase fractions, the effective medium is identical to that of a simple series circuit model that is shown in Fig.4.5b, which allows one to greatly simplify the equations for the effective transport properties. The electrical conductivity is

$$\sigma^{-1} = (1 - t_{\mathrm{GB}})\sigma_{\mathrm{G}}^{-1} + t_{\mathrm{GB}}\sigma_{\mathrm{GB}}^{-1}, \tag{4.7}$$

where t_{GB} is the size fraction of the grain boundary phase in the total sample, and subscripts G and GB refer to the grain and grain boundary phase, respectively. The Seebeck coefficient is

$$S = \frac{S_{\mathrm{G}}\frac{1-t_{\mathrm{GB}}}{\kappa_{\mathrm{G}}} + S_{\mathrm{GB}}\frac{t_{\mathrm{GB}}}{\kappa_{\mathrm{GB}}}}{\frac{1-t_{\mathrm{GB}}}{\kappa_{\mathrm{G}}} + \frac{t_{\mathrm{GB}}}{\kappa_{\mathrm{GB}}}}, \tag{4.8}$$

where κ is thermal conductivity. Since t_{GB} is very small and S_i's and κ_i's are each similar in orders of magnitude between the two phases, Eq.4.8 simply reduces to

$$S \approx S_{\mathrm{G}}. \tag{4.9}$$

A key feature of the model seen from Eqs.4.7 and 4.9 is that the thermopower is virtually unchanged due to the grain boundaries whereas the conductivity could be significantly reduced when σ_{GB} is much less conductive than σ_{G}. This behavior is consistent with many experimental observations in grain boundary dominated materials such as SiGe [9], Mg_2Si [15], $CoSb_3$ [24], and Ca_3AlSb_3 [25]. This behavior is in direct contrast to what a Matthiessen's rule approach (homogeneous approach) would predict: a significant change in the Seebeck coefficient due to grain boundaries.

Determining the model parameters

Each model phase is described with their own transport functions. For the grain phase, $s = 1$ is used because the high temperature limit of transport and also the $S - \sigma$ relation indicate that deformation potential scattering is the transport mechanism. For the grain boundary phase, $s = 3$ for ionized impurity scattering is used considering the potential barrier.

Table 4.1: Parameters for the two-phase transport model of polycrystalline n-type $Mg_{3+\delta}Sb_{1.5}Bi_{0.5}$ doped with Te

Grain phase	σ_{E_0} = 900 S/cm (s=1)
Grain boundary phase	σ_{E_0} = 0.2 S/cm at 300 K (s=3) t_{GB} = 0.001
Band offset	ΔE_0 = 60 meV a = 0.3

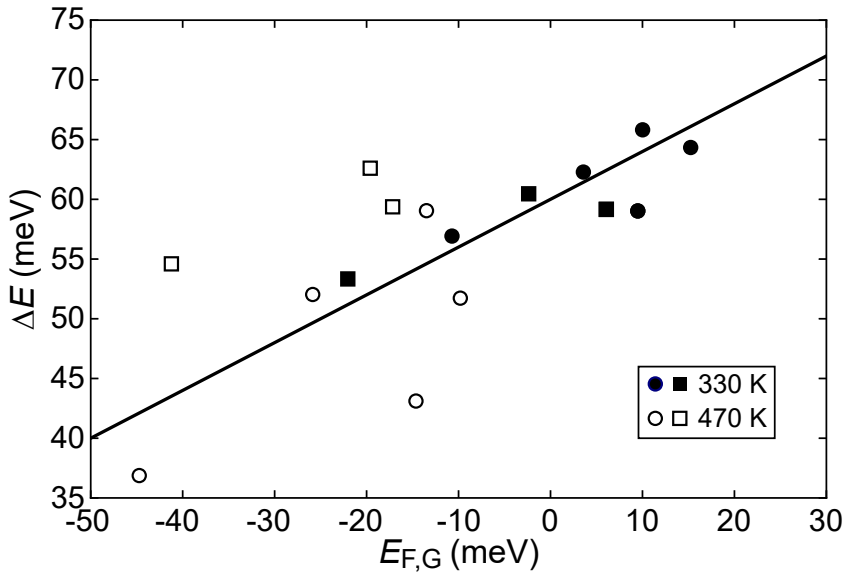

Figure 4.6: Band offsets that give the best fit for individual samples at a given temperature. The overall trend shows an increasing relation between the band offset and Fermi-level, which is a trend that is expected from the charge transfer mechanism that produces the offset. A linear fit to the individually determined offset values is used as an empirical function for determining the band offset in the data set. While this procedure apparently reduces the quality of the fits, it greatly reduces the fitting degree-of-freedom and also gives predictive power to the model. Circled and squared data points are from Refs.[4] and [3], respectively.

The band offset ΔE is an increasing function of the Fermi level of the grain phase $E_{\mathrm{F,G}}$. To find the band offset function empirically, the band offset is first let to be a free parameter. By fitting the $S - \sigma$ relation and also the temperature derivative of σ at both 330 and 470 K, the best band offset ΔE parameters are found and plotted with respect to $E_{\mathrm{F,G}}$ in Fig.4.6. This empirical trend is fit with a linear function:

$$\Delta E = \Delta E_0 + a E_{\mathrm{F,G}}. \tag{4.10}$$

The band offset is now restricted to be this linear function form rather than being allowed to be a free parameter. This approach decreases the fitting degree of freedom.

Finally, the best parameter set is found by fitting all S and σ measurements at all temperatures to produce the best fit in the $S - \sigma$ and $\sigma(T)$ plots. The parameters found by this procedure are listed in Table 4.1.

The final grain boundary model is plotted as solid lines in Fig.4.2 ($S - \sigma$ relation) and Fig.4.7a (temperature dependency of conductivity) showing good agreement

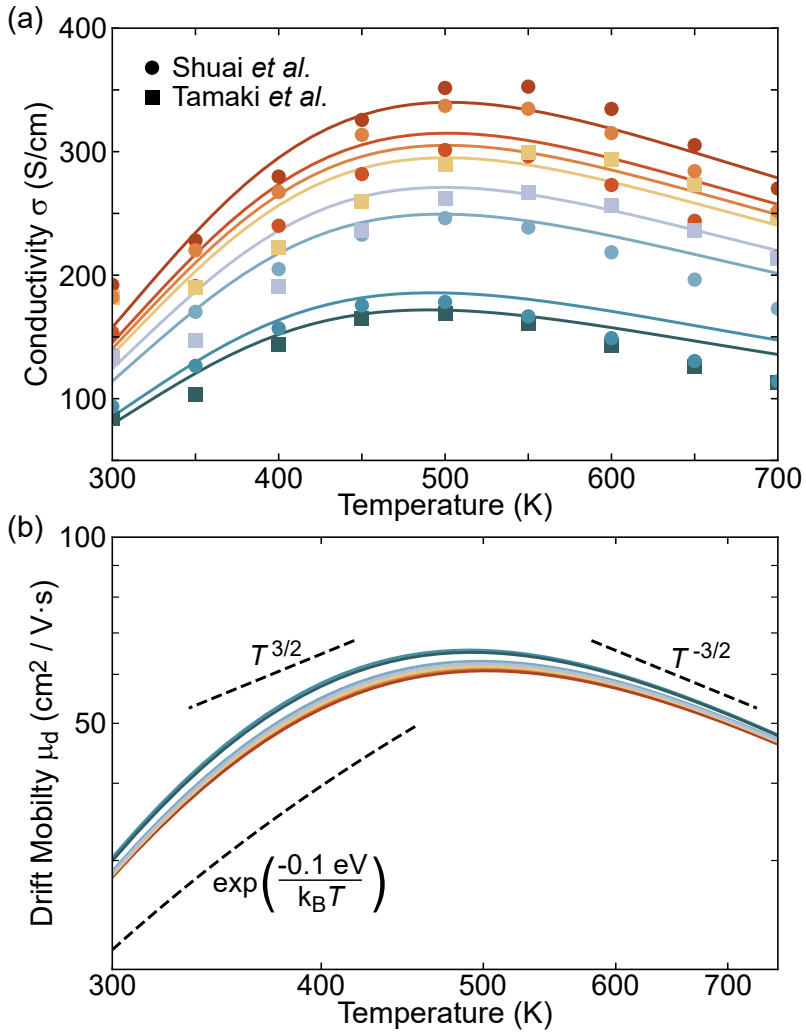

Figure 4.7: The grain boundary transport model using parameters listed in Table 4.1. **(a)** Conductivity as a function of temperature, showing good agreement with data. Data points are from Refs.[3, 4]. **(b)** Drift mobility calculated from the conductivity in (a) and using a density-of-states effective mass of $m^*_{\mathrm{DOS}} = N_{\mathrm{V}}^{2/3} m^*_{\mathrm{b}} \approx 6^{2/3} 0.3 m_{\mathrm{e}}$.

with the reported data. It is seen that the grain boundary model shows a $S - \sigma$ relation very similar to that of deformation potential scattering ($s = 1$) while also reproducing the thermally activated conduction behavior at low temperature. The essential feature in the model that makes it possible to capture this key behavior of the experimental data is the thin second phase with a band offset, but not the $s = 3$ setting of the grain boundary phase; a same fitting quality can be achieved by alternatively assuming $s = 1$ for the grain boundary phase (the only difference is that this alternative setting produces much larger band offset values). Therefore, it can be concluded that the simplified model devised to take into account the potential

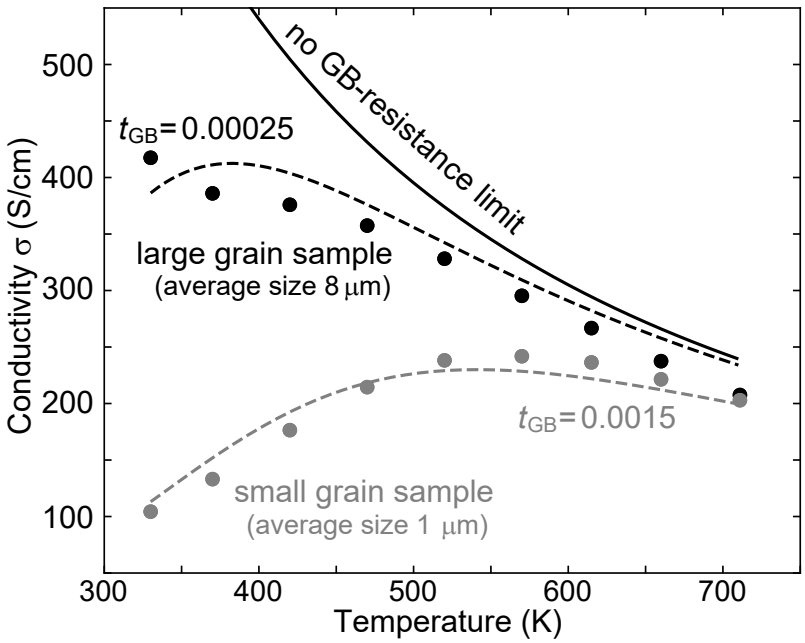

Figure 4.8: The grain boundary model applied to a different data set where the grain size was changed. All model parameters were fixed to that in Table 4.1 expect for t_{GB}. The scaling in t_{GB} required to best fit the data is similar to that of the measured average grain size. The model limit with no grain boundary resistance ($t_{GB} = 0$) is also shown for comparison. Data points are from Ref.[2].

barrier with a simplified offset is working as intended.

The drift mobility is also calculated from the model, showing the temperature dependencies that led to the previous suggestions about ionized impurity scattering. Within a small temperature span, the dependency resembles that of not just a power law, but also that of an exponential or even a variable range hopping type dependency. This resemblance once again demonstrates how one should be cautious in interpreting temperature dependencies of measured conductivity or mobility.

The predictive power of the model for grain size scaling is tested by fitting to a different set of experimental data measured from samples with different average grain sizes. The results plotted in Fig.4.8 shows reasonable agreement, which allows to project the conductivity limit of a single crystal.

This big increase predicted in the low temperature conductivity (recall that the Seebeck coefficient remains unchanged) has important implications for thermoelectric applications, because it indicates a possible increase in the figure-or-merit if the benefit could outweigh any increases in thermal conductivity. Such improvements were

demonstrated in Refs.[1, 2]. Based on the understanding gained from the Mg_3Sb_2 model, similar opportunities could be explored in other thermoelectric materials that also show signatures of grain boundary dominated transport near room temperature. Some examples include polycrystalline SnSe [17], $KAlSb_4$ [26], Sr_3GaSb_3 [27], NbFeSb [16], $Ca_5Al_2Sb_6$ [28], and Ca_3AlSb_3 [25].

References

[1] J. J. Kuo, S. D. Kang, K. Imasato, H. Tamaki, S. Ohno, T. Kanno, and G. J. Snyder, "Grain boundary dominated charge transport in Mg_3Sb_2-based compounds", Energy & Environmental Science **11**, 429–434 (2018) 10.1039/C7EE03326E.

[2] T. Kanno, H. Tamaki, H. K. Sato, S. D. Kang, S. Ohno, K. Imasato, J. J. Kuo, G. J. Snyder, and Y. Miyazaki, "Enhancement of average thermoelectric figure of merit by increasing the grain-size of $Mg_{3.2}Sb_{1.5}Bi_{0.49}Te_{0.01}$", Applied Physics Letters **112**, 033903 (2018) 10.1063/1.5016488.

[3] H. Tamaki, H. K. Sato, and T. Kanno, "Isotropic conduction network and defect chemistry in $Mg_{3+\delta}Sb_2$-based layered Zintl compounds with high thermoelectric performance", Advanced Materials **28**, 10182–10187 (2016).

[4] J. Shuai, J. Mao, S. Song, Q. Zhu, J. Sun, Y. Wang, R. He, J. Zhou, G. Chen, D. J. Singh, and Z. Ren, "Tuning the carrier scattering mechanism to effectively improve the thermoelectric properties", Energy & Environmental Science **10**, 799–807 (2017).

[5] H. X. Xin, X. Y. Qin, X. G. Zhu, and Y. Liu, "Temperature dependence of electrical resistivity for nanocrystalline $Mg_{3+x}Sb_2$ prepared by mechanical alloying", Journal of Physics D: Applied Physics **39**, 375 (2006).

[6] J. Mao, J. Shuai, S. Song, Y. Wu, R. Dally, J. Zhou, Z. Liu, J. Sun, Q. Zhang, C. dela Cruz, S. Wilson, Y. Pei, D. J. Singh, G. Chen, C.-W. Chu, and Z. Ren, "Manipulation of ionized impurity scattering for achieving high thermoelectric performance in n-type Mg_3Sb_2-based materials", Proceedings of the National Academy of Sciences **114**, 10548–10553 (2017).

[7] A. F. Mayadas and M. Shatzkes, "Electrical-resistivity model for polycrystalline films: the case of arbitrary reflection at external surfaces", Physical Review B **1**, 1382–1389 (1970).

[8] W. Steinhögl, G. Schindler, G. Steinlesberger, and M. Engelhardt, "Size-dependent resistivity of metallic wires in the mesoscopic range", Physical Review B **66**, 075414 (2002).

[9] A. Minnich, H. Lee, X. Wang, G. Joshi, M. Dresselhaus, Z. Ren, G. Chen, and D. Vashaee, "Modeling study of thermoelectric SiGe nanocomposites", Physical Review B **80**, 155327 (2009).

[10] R. Waser, "Electronic properties of grain boundaries in $SrTiO_3$ and $BaTiO_3$ ceramics", Solid State Ionics **75**, 89–99 (1995).

[11] G. E. Pike and C. H. Seager, "The dc voltage dependence of semiconductor grain-boundary resistance", Journal of Applied Physics **50**, 3414–3422 (1979).

[12] H. F. Mataré, "Carrier transport at grain boundaries in semiconductors", Journal of Applied Physics **56**, 2605–2631 (1984).

[13] K. Imasato, S. D. Kang, S. Ohno, and G. J. Snyder, "Band engineering in Mg_3Sb_2 by alloying with Mg_3Bi_2 for enhanced thermoelectric performance", Materials Horizons **5**, 59–64 (2018) 10.1039/C7MH00865A.

[14] K. Imasato, S. Ohno, S. D. Kang, and G. J. Snyder, "Improving the thermoelectric performance in $Mg_{3+x}Sb_{1.5}Bi_{0.49}Te_{0.01}$ by reducing excess Mg", APL Materials **6**, 016106 (2018) 10.1063/1.5011379.

[15] J. de Boor, T. Dasgupta, H. Kolb, C. Compere, K. Kelm, and E. Mueller, "Microstructural effects on thermoelectric efficiency: a case study on magnesium silicide", Acta Materialia **77**, 68–75 (2014).

[16] R. He, D. Kraemer, J. Mao, L. Zeng, Q. Jie, Y. Lan, C. Li, J. Shuai, H. S. Kim, Y. Liu, D. Broido, C.-W. Chu, G. Chen, and Z. Ren, "Achieving high power factor and output power density in p-type half-heuslers $Nb_{1-x}Ti_xFeSb$", Proceedings of the National Academy of Sciences **113**, 13576–13581 (2016).

[17] T.-R. Wei, G. Tan, X. Zhang, C.-F. Wu, J.-F. Li, V. P. Dravid, G. J. Snyder, and M. G. Kanatzidis, "Distinct impact of alkali-ion doping on electrical transport properties of thermoelectric p-type polycrystalline SnSe", Journal of the American Chemical Society **138**, 8875–8882 (2016).

[18] S. Ohno, K. Imasato, S. Anand, H. Tamaki, S. D. Kang, P. Gorai, H. K. Sato, E. S. Toberer, T. Kanno, and G. J. Snyder, "Phase boundary mapping to obtain n-type Mg_3Sb_2-based thermoelectrics", Joule **2**, 141–154 (2018) 10.1016/j.joule.2017.11.005.

[19] J. Y. Seto, "The electrical properties of polycrystalline silicon films", Journal of Applied Physics **46**, 5247–5254 (1975).

[20] W. Taylor, N. Odell, and H. Fan, "Grain boundary barriers in germanium", Physical Review **88**, 867 (1952).

[21] Z. Hashin and S. Shtrikman, "A variational approach to the theory of the effective magnetic permeability of multiphase materials", Journal of Applied Physics **33**, 3125–3131 (1962).

[22] D. J. Bergman and O. Levy, "Thermoelectric properties of a composite medium", Journal of Applied Physics **70**, 6821–6833 (1991).

[23] D. J. Bergman and L. G. Fel, "Enhancement of thermoelectric power factor in composite thermoelectrics", Journal of Applied Physics **85**, 8205–8216 (1999).

[24] M. S. Toprak, C. Stiewe, D. Platzek, S. Williams, L. Bertini, E. Müller, C. Gatti, Y. Zhang, M. Rowe, and M. Muhammed, "The impact of nanostructuring on the thermal conductivity of thermoelectric $CoSb_3$", Advanced Functional Materials **14**, 1189–1196 (2004).

[25] W. G. Zeier, A. Zevalkink, E. Schechtel, W. Tremel, and G. J. Snyder, "Thermoelectric properties of Zn-doped Ca_3AlSb_3", Journal of Materials Chemistry **22**, 9826–9830 (2012).

[26] B. R. Ortiz, P. Gorai, L. Krishna, R. Mow, A. Lopez, R. McKinney, V. Stevanovic, and E. S. Toberer, "Potential for high thermoelectric performance in n-type Zintl compounds: a case study of Ba doped $KAlSb_4$", Journal of Materials Chemistry A **5**, 4036–4046 (2017).

[27] A. Zevalkink, W. G. Zeier, G. Pomrehn, E. Schechtel, W. Tremel, and G. J. Snyder, "Thermoelectric properties of Sr_3GaSb_3 - a chain-forming Zintl compound", Energy & Environmental Science **5**, 9121 (2012).

[28] E. S. Toberer, A. Zevalkink, N. Crisosto, and G. J. Snyder, "The Zintl compound $Ca_5Al_2Sb_6$ for low-cost thermoelectric power generation", Advanced Functional Materials **20**, 4375–4380 (2010).

Chapter 5

ANOMALOUS TRANSPORT: SUPERIONIC Cu_2Se

In degenerate semiconductor crystals showing metallic transport behavior, one would model and analyze transport properties by applying typical concepts relevant for band conductors. The conceptual distinction between transport phenomenology (*i.e.* transport function) and the physical model (effective mass and kinematic parameters) may not be necessarily beneficial if the system is well described with effective masses and mobilities. However, when those band parameters do not behave like a typical band conductor, it could be challenging to determine whether conventional analysis methods remain valid in such a system. The copper selenide material system is such an example [1, 2], and it will be shown that many analysis concepts can still be used if one avoids the determination of effective mass or carrier concentration and rather rely on phenomenological concepts. Because of the practical interest in copper selenide as a thermoelectric material, this approach provides some useful means for evaluating the practical values of this material.

Copper selenide, Cu_2Se, is the prototypical compound that represents the class of superionic thermoelectric materials [3]. The ionic conductivity of these materials in their high temperature solid phase are comparable to that of an ionic liquid ($\approx$ 1 S/cm) due to high cation diffusivity [4, 5], which is believed to be associated with a high degree of structural disorder that results in a low lattice thermal conductivity advantageous for thermoelectrics [6]. The electrical properties resemble that of a heavily doped semiconductor, which is also good for obtaining the optimum carrier concentration required for thermoelectrics. The native defects (*e.g.* Cu vacancies in $Cu_{2-x}Se$) are abundant enough to provide carrier concentrations on the order of 10^{20} /cm^3 without using foreign dopants.

In Cu_2Se, the high temperature transport properties are of primary interest because of its competitive thermoelectric figure-of-merit zT; however, modeling transport through the typical route of determining an effective mass could be puzzling because of the apparent order-of-magnitude increase in the Hall carrier concentration from a temperature increase of about 600 K. This unexplained behavior has sometimes raised questions about whether band equations could be used for these highly disordered materials. In Section 5.1, it is shown that, by avoiding the individual

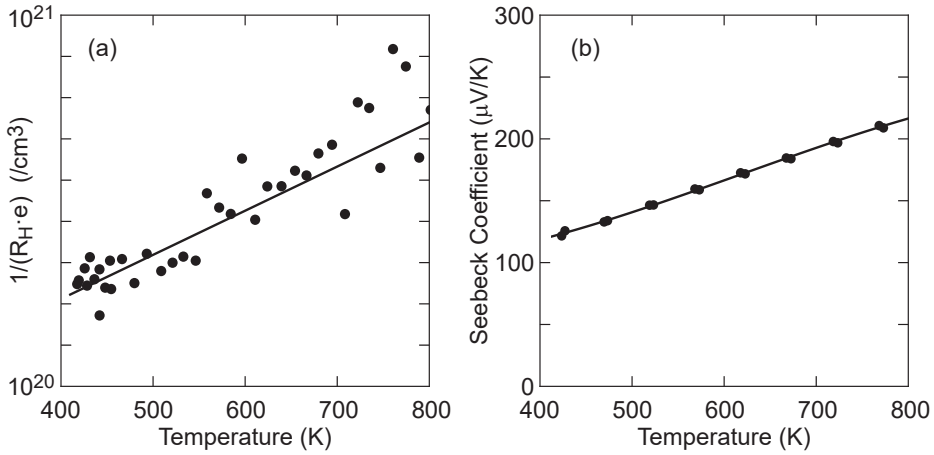

Figure 5.1: Measured **(a)** Hall carrier concentration ($n_{\mathrm{H}} = 1/R_{\mathrm{H}}/e$) and **(b)** Seebeck coefficient of $Cu_{1.985}Se$ in the superionic cubic phase. Solid lines are guides to the eyes.

determination of m^* and n, the Seebeck coefficient and conductivity can still be described with the phenomenological relation $s = 1$, which is the typical behavior of a high temperature degenerate semiconductor. This modeling strategy is used to explore routes for material improvement and also to understand the uncertainty in some zT values reported in the literature.

Another interesting phenomenon in Cu_2Se for thermoelectrics is the superionic phase transition where a sharp peak in zT and thermopower is found. High estimations for zT of > 2 have been suggested around the phase transition, and theories of critical phenomena enhancing the thermopower or zT has also been proposed. In Section 5.2, the controversies over the phase transition is elucidated with the help of transport analysis.

5.1 Transport analysis of the superionic phase

Anomaly in the Hall effect

The effective mass is not straightforwardly determined in the high temperature cubic phase of $Cu_{2-x}Se$. This difficulty is due to the peculiar feature observed in Hall measurements, where the Hall carrier concentration increases significantly with temperature as shown in Fig.5.1a. It is rather unphysical to attribute this increase to an actual increase in the (chemical) carrier concentration – the real number of carriers populated in the valence band as a function of chemical composition – because the thermopower shows a typical curve resembling that of a degenerate

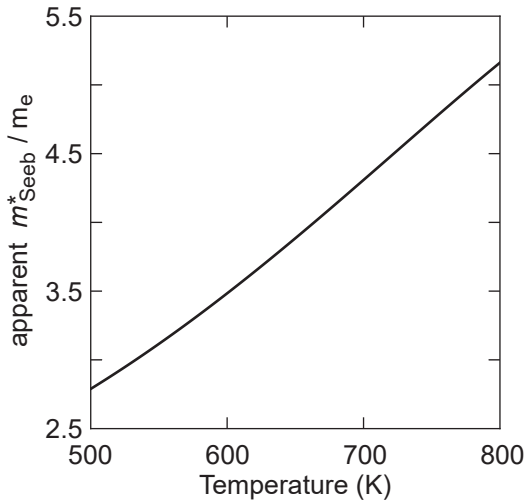

Figure 5.2: m^*_{Seeb} extracted from n_{H} and S in Fig.5.1, apparently showing a significant increase with temperature.

semiconductor with a fixed carrier concentration (Fig.5.1b). This peculiarity is most obviously seen by combining the thermopower and Hall measurements into a Seebeck effective mass[1] m^*_{Seeb}. It is seen in Fig.5.2 that m^*_{Seeb} increases significantly from $\approx 2.8\,(500\,\mathrm{K})$ to $\approx 5.2\,(800\,\mathrm{K})$, which is in contrast to the valence band structure of the phase where no other bands than the Γ band are expected to contribute to transport [7].

Considering the possibility that the anomalous Hall coefficient is simply an issue related to the Hall measurement rather than effective mass, the $S - \sigma$ relation[2] is used to extract the temperature dependency of the transport function and compared to the band conduction model. Fig.5.3 shows the measured S and $\rho = 1/\sigma$ values from a number of $Cu_{2-x}Se$ samples in the high temperature cubic phase. To test the band conduction model with deformation potential scattering, weighted mobility μ_{w} (Eq.1.53) is evaluated from $S - \sigma$ data pairs at each temperature while assuming $s = 1$ (*i.e.* $r = -\frac{1}{2}$). This procedure avoids the direct determination of effective mass because it is mathematically equivalent to determining the phenomenological

[1] m^*_{Seeb} is defined by the effective mass experimentally determined combining measurements of the Seebeck coefficient and Hall coefficient with the use of Eqs.1.55 and 1.57. $m^*_{\mathrm{H}} = N_{\mathrm{V}}^{2/3} m^*_{\mathrm{b}}$ in Eq.1.57 should be replaced with m^*_{Seeb} for this definition: *i.e.* m^*_{Seeb} is an estimate of m^*_{H} by using S as a means to find η, which one could also refer to as the Seebeck-Hall mass.

[2] Unfortunately, the $S - \sigma$ relation at a given temperature cannot be studied directly using samples with different Seebeck coefficients as has been done to confirm the s exponent in previous chapters because $Cu_{2-x}Se$ or Li-doped $Cu_{2-x}Se$ do not show a rigid band behavior with respect to off-stoichiometry or doping.

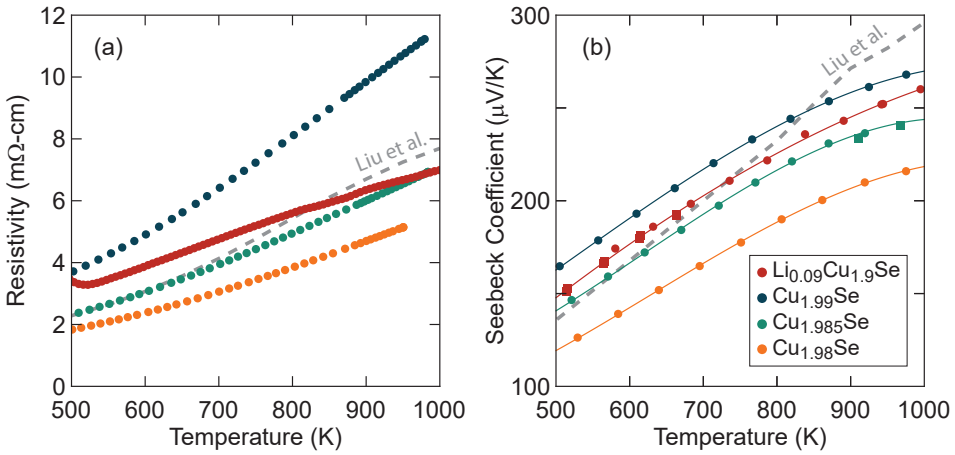

Figure 5.3: Measured **(a)** electrical resistivity and **(b)** Seebeck coefficient of $Cu_{2-x}Se$ and related compounds in the superionic cubic phase. Literature data from Ref.[3] is shown together for comparison.

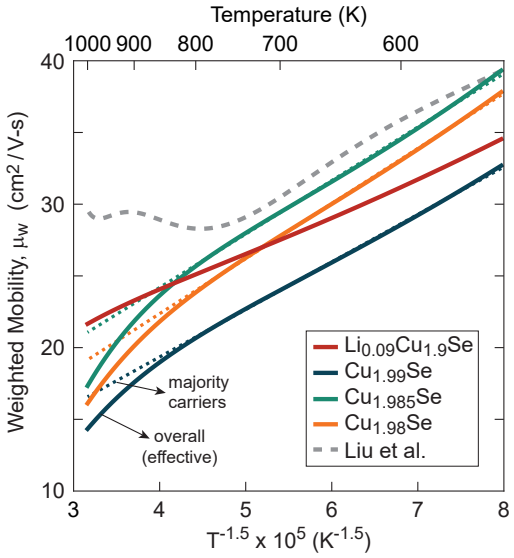

Figure 5.4: Weighted mobilities extracted from the Seebeck coefficient and conductivity data shown in Fig.5.3. At high temperatures where minority carriers negate the thermopower from the majority hole carriers, the extracted μ_w values (solid lines) show a further decrease than the extrapolated trend; the extrapolated lines (dotted lines) are what is expected for the majority carriers. Extracted values in the bipolar conduction region could be considered an effective overall value. The Li-doped compound does not show any sign of bipolar conduction up to 1000 K due to an enlarged band gap. The unexpected break in the literature-extracted μ_w curve (gray dashed line; Ref.[3]) around 800 K corresponds to the temperature where the Seebeck measurement (Fig.5.3) shows a sudden increase in the $S(T)$ slope.

transport coefficient (σ_{E_0}) and converting to a weighted mobility with T and physical constants. The extracted μ_{w} values are shown in Fig.5.4, where $T^{-3/2}$ behavior is seen in the non-bipolar region. These results are compared to the deformation potential scattering model for acoustic phonons [8] which also predicts $T^{-3/2}$:

$$\mu_{\mathrm{w}} = \frac{N_{\mathrm{V}}\pi e\hbar^4 C_{\mathrm{l}}}{\sqrt{2}m_{\mathrm{I}}^*(k_B T)^{3/2}\Xi^2}. \tag{5.1}$$

Here, C_{l} is the longitudinal elastic constant, m_{I}^* is the inertial effective mass $\approx m_{\mathrm{b}}^*$ and Ξ is the deformation potential. Had the apparent increase in m_{Seeb}^* (Fig.5.2) represented an actual increase in the effective mass, μ_{w} would have not shown a linear scaling with $T^{-3/2}$. Therefore, it seems reasonable to attribute the apparent increase in effective mass to a complication in the Hall measurement (or its interpretation).

Although the particular physical origin for the anomalous Hall measurement is unclear, it is worth to note that it is not uncommon to have challenges in interpreting Hall measurements even when other transport properties are reasonably understood or described. One suspect is the presence of a high mobility impurity phase. Since high mobility bands are much more sensitive to an applied magnetic field (roughly speaking, mobility acts as a weighting factor for sensitivity in magnetoresistance measurements as shown by the $\frac{\tau}{m_{\mathrm{b}}^*}$ factor in Eq.1.47), even a small amount of impurities at the level not detectable with diffraction could contribute significantly to the Hall measurement if they have high mobility carriers. For example, a small amount of Cu precipitates would contribute negatively to the Hall coefficient and partially cancel the positive value of $Cu_{2-x}Se$, producing an apparent increase in the Hall carrier concentration. The impact of such impurities would be negligible for Seebeck measurements because the Seebeck coefficient of a composite is weighted by electrical conductance and thermal resistance [9] which is usually negligible when in small amounts. This example scenario illustrates how the Seebeck coefficient is often a more robust measurement than the Hall coefficient for extracting information about E_{F}.

In the next sections, we center the analysis around S and σ rather than R_{H} or effective mass. This approach will also be used for the quality factor evaluation in Ch.6.

Assessment of the high temperature zT variation in the literature

One of the difficulties in evaluating the true potential of $Cu_{2-x}Se$ compounds for thermoelectric applications is related to the significantly varied high temperature zT values reported in the literature. As shown in Fig.5.5, the peak zT of the

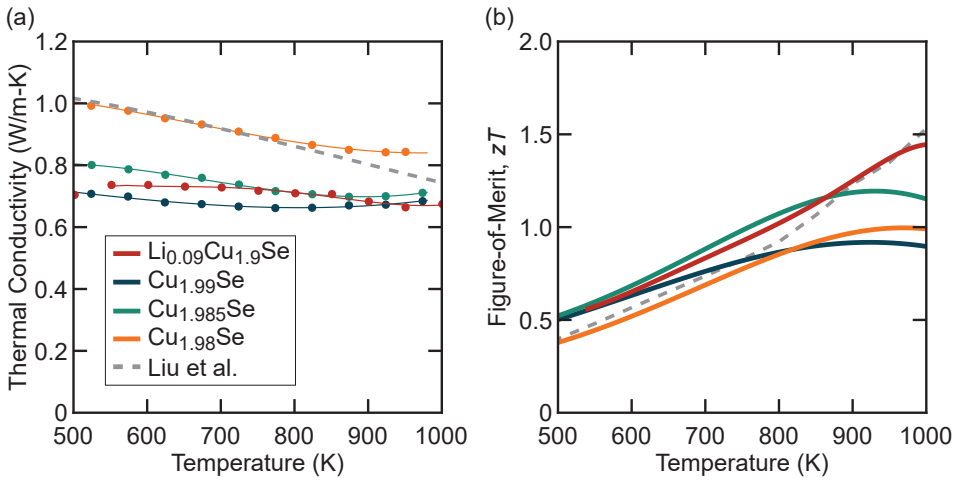

Figure 5.5: Determining the thermoelectric figure-of-merit in Cu_2Se. **(a)** Thermal conductivity evaluated by measuring the thermal diffusivity with the laser flash method. Identical heat capacity values as reported in Ref.[3] were used for the comparison. **(b)** Thermoelectric figure-of-merit zT evaluated. It is seen that the literature data apparently shows no sign of bipolar conduction in the zT curve. In the current study, suppressed bipolar conduction is only seen in Li-doped samples, in which the band gap is enlarged due to the alloying effect with Li_2Se, a wide band gap compound [10]. The discrepancy is attributed to the Seebeck measurement as seen in Figs.5.3 and 5.4.

undoped compound varies not only in its value ($\approx$ 30% difference) but also the peak temperature (900 vs. $>$ 1000 K). It is interesting to note that the earliest reports on the identical material [11] also showed only moderate zT values.

The biggest source of variation in $zT = S^2\sigma T/\kappa$ is identified in the difference in Seebeck measurements. The Seebeck coefficient difference of $\approx$ 15% at 1000 K contributes to a $>$ 30% difference in zT. The identification of a well behaved μ_w in the samples from the present study (solid lines in Fig.5.4), which is in contrast to the rather unphysical behavior of that extracted from literature data (gray dashed line), suggests that the steep increase in the literature Seebeck coefficient values might be associated with measurement issues.

Majority of the recent literature data are obtained using a commercial four-probe configuration with type S thermocouples and a static atmosphere [12]; many issues relating to potential measurement errors in this commercial system have been discussed in the literature [13, 14]. An overestimation due to the cold finger effect inherent in the four-probe configuration, platinum reactivity with the material, and oxidation due to the poorly controlled atmosphere (which is not dynamic vacuum)

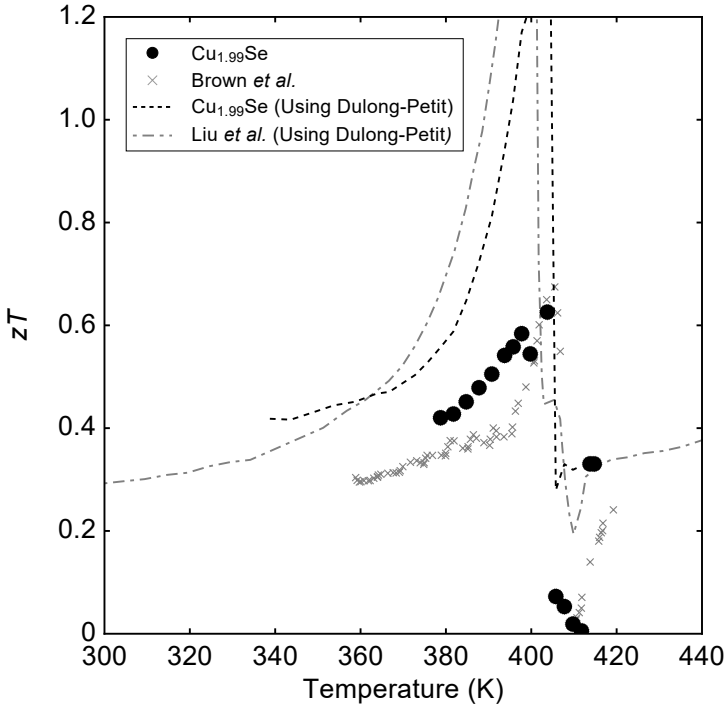

Figure 5.6: Thermoelectric figure-of-merit evaluation near the superionic phase transition of Cu_2Se. Use of the Dulong-Petit value results in an erroneous overestimation in the zT value. Literature data are from Refs.[16, 17].

are a number of possible causes that could explain the overestimation. The Seebeck coefficient measured in the present study uses a home built system which circumvents many of the potential issues discussed above [15]. Above all, the Seebeck coefficients measured in the present study are highly reproducible and steady over long periods of time which is in contrast to anecdotal notes from commercial system users that note unstable and noisy measurements very often encountered in the measurement of copper chalcogenide materials. More details regarding Seebeck measurements will be discussed in Ch.7.

5.2 Two-phase description of the anomalous transport observed during the superionic phase transition

Cu_2Se goes through a phase transition around 350-400 K, during which the room temperature phase gradually transforms into a superionic high temperature phase. This superionic phase transition has drawn great interest because of a number of interesting observations accompanied during the transformation. The Seebeck coefficient and zT both show a sharp peak around 400 K. Thermal diffusivity plunges to almost zero. The phenomena have brought up a great discussion regarding the

thermodynamic nature of the transition and also about the true peak zT value. Clarifications regarding the phenomena have been published in Ref.[1]; here, the key conclusions are summarized, and then it will be briefly demonstrated how the transport analysis of S and σ support those conclusions.

Whether the true peak zT value is as high as > 2, or is a moderate value < 1, has been one of the issues that results from using different heat capacity values for converting thermal diffusivity into thermal conductivity. Use of the Dulong-Petit value results in a peak $zT > 2$ as shown in Fig.5.6, but measurements from scanning calorimetry show a peak in the heat capacity measurement which gives a peak $zT < 1$ if taken into account. Using the Dulong-Petit value is not correct regardless of assuming the phase transition to be 1st or 2nd order. If a 2nd order phase transition is assumed, the measured peak in heat capacity would be due to critical fluctuations, an inherent part of the heat capacity that would have to be included in the conversion in any case. If a 1st order phase transition is assumed, the measured peak would be due to the transformation enthalpy that is distributed over the two-phase region temperatures. Then, as long as the transformation enthalpy can contribute during the diffusivity measurement, it should be taken into account. Alternative measurements of thermal effusivity also indicate that the plunging diffusivity is due to the peak in heat capacity, regardless of the physical origin of the peak.

Many reports have suggested that the superionic phase transition is a 2nd order transition [16–20], but closer examination strongly suggests that the phase transition is of 1st order [1]. Above all, it has been shown that the Landau criterion for a 2nd order phase transition based on group theory [21, 22] is violated in Cu_2Se. Then, it has been pointed out that most features that had been associated with the continuous nature of the transition is simply explained with a gradual change in the phase fractions between two phases. The misconception about gradual vs. abrupt changes being associated with 1st and 2nd order transitions, respectively, seems to result from the simplified schematics used for elementary introduction where only unary systems (one component) are considered. In binary systems, the degree of freedom to adjust phase fractions always makes the transformation a 1st order transition unless at a special point of particular composition or pressure. The observation of similar phenomena from a wide range of off-stoichiometry is then additional evidence that the phenomena is not from a 2nd order phase transition.

The two-phase mixture picture for the phase transformation offers an excellent explanation for the transport properties measured during the transformation as shown

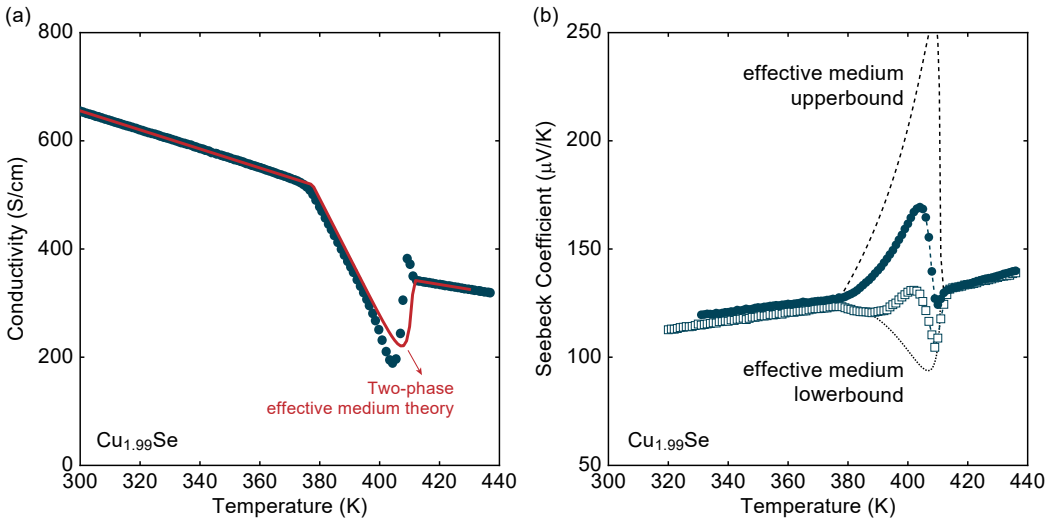

Figure 5.7: Transport properties of $Cu_{1.99}Se$ near the superionic phase transition. **(a)** Conductivity measured upon heating with a rate of 6 K/h. The kink around 380 K indicates the onset of the phase transformation. The red solid line represents the calculated result from effective medium theory. **(b)** Seebeck coefficient measured upon repeated heating cycles with a ramping rate of 25 K/h. Each marker type represents a measurement with a different sample loading (cycled multiple times with a given loading) using the same sample. The filled circle markers represent the behavior observed in the majority of loadings. The open square markers represent a minority behavior occasionally observed. The difference is attributed to different microstructure evolution during the phase transformation with respect to the loaded probes. The dashed line shows the calculated upper bound from effective medium theory (microstructure equivalent to a series circuit connection of two phases) and dotted line shows the lower bound (equivalent to a parallel circuit).

in Fig.5.7. According to the phase diagram reported in [1] (based on information from Refs.[23] and [24]), $Cu_{1.99}Se$ nucleates the high temperature phase near 378 K and completes the transformation near 411 K. Nucleation of a new phase causes a big decrease in the copper vacancy concentration in the lower temperature phase (which is the main phase during the majority of the heating transformation), which explains the decrease in conductivity and increase in Seebeck coefficient.

Conductivity can be calculated with effective medium theory using the phase diagram, and the results agree well with the measured data (Fig.5.7a). The phase diagram provides the relative phase fractions throughout the transition temperature range, and also the chemical compositions for both phases. Using this information, the changes in the Fermi-level for each phase can be calculated. One can also calculate the phenomenological trend of the transport coefficient $\sigma_{E_0}(T)$ by fitting to

the single phase region at below and above the phase transition temperature range. Combining these information, and assuming spherical grains, the effective medium conductivity during the phase transformation can be calculated with no fitting parameters. The result shows good agreement despite a simplistic assumption about the microstructure. It should be noted that the most critical factor for this calculation is the phase diagram information, rather than the detailed procedure of the transport modeling. A more simplified transport calculation as was previously given in [1] yields results similar to that shown in Fig.5.7a.

The Seebeck coefficient during the phase transformation is also well explained with effective medium theory using the phase diagram (Fig.5.7b). Previously, it has been argued that the increase in the Seebeck coefficient is in "excess" to what is expected from a single phase material [17]. However, with the two-phase picture, it is shown in Fig.5.7b that the upper and lower limits of effective medium (calculated using the theory by Bergman *et al.* [9]) envelope any of the measured instances. The actual experimental manifest is highly dependent on the particular microstructure evolution that happens in the measurement loading, which is due to the nature of Seebeck coefficient highly depending on the microstructure of the effective medium. Indeed, measuring upon many different loadings result in a number of different transformation curves. Data of two of the most representative cases are plotted in Fig.5.7b.

Overall, transport analysis support the two-phase mixture picture based on a first order phase transition. The apparently "anomalous" behavior that was thought to resemble signatures of critical phenomena has been shown to be well explained with classical effective medium theory.

5.3 Experimental notes on synthesis and stoichiometry control

Sample variation in Cu_2Se depending on synthesis routes has been another major source for some of the discrepancies found in the literature. Much of the variation is caused by the native oxides and hydroxides present in the raw Cu elements provided by standard market suppliers. These native impurities react with conventional reaction vessels such as fused quartz (even when they are carbon coated), in addition to compromising the purity and stoichiometry of the final compound. Such complications could be easily avoided by reducing the raw Cu material under H_2 atmosphere. Purchasing pre-reduced materials from suppliers (often labeled "oxygen-free") is an alternative that yields similar results.

Most notable difference is seen from the properties of the sample with a nominally stoichiometric composition of Cu_2Se. Most literature reports [3, 11, 16, 25–29] on the nominally stoichiometric Cu_2Se show transport properties (S or room temperature n_H) that are similar to oxygen-reduced samples with a nominal stoichiometry of $Cu_{1.98}Se$ or $Cu_{1.985}Se$. Another difference is the sample reproducibility. Samples synthesized with oxygen-reduced copper show very reproducible properties for a given nominal composition, whereas significant sample variation is seen in the literature even for samples synthesized from the same lab.

References

[1] S. D. Kang, S. A. Danilkin, U. Aydemir, M. Avdeev, A. Studer, and G. J. Snyder, "Apparent critical phenomena in the superionic phase transition of $Cu_{2-x}Se$", New Journal of Physics **18**, 013024 (2016) 10.1088/1367-2630/18/1/013024.

[2] S. D. Kang, J.-H. Pöhls, U. Aydemir, P. Qiu, C. C. Stoumpos, R. Hanus, M. A. White, X. Shi, L. Chen, M. G. Kanatzidis, and G. J. Snyder, "Enhanced stability and thermoelectric figure-of-merit in copper selenide by lithium doping", Materials Today Physics **1**, 7–13 (2017) 10.1016/j.mtphys.2017.04.002.

[3] H. Liu, X. Shi, F. Xu, L. Zhang, W. Zhang, L. Chen, Q. Li, C. Uher, T. Day, and G. J. Snyder, "Copper ion liquid-like thermoelectrics", Nature Materials **11**, 422–425 (2012).

[4] S. Danilkin, M. Avdeev, M. Sale, and T. Sakuma, "Neutron scattering study of ionic diffusion in Cu-Se superionic compounds", Solid State Ionics **225**, 190–193 (2012).

[5] D. J. Voneshen, H. C. Walker, K. Refson, and J. P. Goff, "Hopping time scales and the phonon-liquid electron-crystal picture in thermoelectric copper selenide", Physical Review Letters **118**, 145901 (2017).

[6] H. Kim, S. Ballikaya, H. Chi, J.-P. Ahn, K. Ahn, C. Uher, and M. Kaviany, "Ultralow thermal conductivity of β−Cu_2Se by atomic fluidity and structure distortion", Acta Materialia **86**, 247–253 (2015).

[7] M. Råsander, L. Bergqvist, and A. Delin, "Density functional theory study of the electronic structure of fluorite Cu_2Se", Journal of Physics: Condensed Matter **25**, 125503 (2013).

[8] J. Bardeen and W. Shockley, "Deformation potentials and mobilities in non-polar crystals", Physical Review **80**, 72–80 (1950).

[9] D. J. Bergman and O. Levy, "Thermoelectric properties of a composite medium", Journal of Applied Physics **70**, 6821–6833 (1991).

[10] S. Alay-e-Abbas, N. Sabir, Y. Saeed, and A. Shaukat, "Electronic and optical properties of alkali metal selenides in anti-CaF_2 crystal structure from first-principles", Journal of Alloys and Compounds **503**, 10–18 (2010).

[11] D. R. Brown, T. Day, T. Caillat, and G. J. Snyder, "Chemical stability of $(Ag,Cu)_2Se$: a historical overview", Journal of Electronic Materials **42**, 2014–2019 (2013).

[12] *ULVAC ZEM-3 series, http://www.ulvac.com.*

[13] J. Martin, "Protocols for the high temperature measurement of the Seebeck coefficient in thermoelectric materials", Measurement Science and Technology **24**, 085601 (2013).

[14] J. Mackey, F. Dynys, and A. Sehirlioglu, "Uncertainty analysis for common Seebeck and electrical resistivity measurement systems", Review of Scientific Instruments **85**, 085119 (2014).

[15] S. Iwanaga, E. S. Toberer, A. LaLonde, and G. J. Snyder, "A high temperature apparatus for measurement of the Seebeck coefficient", Review of Scientific Instruments **82**, 063905 (2011).

[16] H. Liu, X. Yuan, P. Lu, X. Shi, F. Xu, Y. He, Y. Tang, S. Bai, W. Zhang, L. Chen, Y. Lin, L. Shi, H. Lin, X. Gao, X. Zhang, H. Chi, and C. Uher, "Ultrahigh thermoelectric performance by electron and phonon critical scattering in $Cu_2Se_{1-x}I_x$", Advanced Materials **25**, 6607–6612 (2013).

[17] D. R. Brown, T. Day, K. A. Borup, S. Christensen, B. B. Iversen, and G. J. Snyder, "Phase transition enhanced thermoelectric figure-of-merit in copper chalcogenides", APL Materials **1**, 052107 (2013).

[18] G. D. Mahan, "The Seebeck coefficient of superionic conductors", Journal of Applied Physics **117**, 045101 (2015).

[19] A. A. Sirusi, S. Ballikaya, C. Uher, and J. H. Ross, "Low-temperature structure and dynamics in Cu_2Se", The Journal of Physical Chemistry C **119**, 20293–20298 (2015).

[20] E. Eikeland, A. B. Blichfeld, K. A. Borup, K. Zhao, J. Overgaard, X. Shi, L. Chen, and B. B. Iversen, "Crystal structure across the β to α phase transition in thermoelectric $Cu_{2-x}Se$", IUCrJ **4**, 476–485 (2017).

[21] L. D. Landau and E. Lifshitz, *Statistical physics part 1*, 3rd ed. rev. (Oxford: Pergamon, 1980).

[22] A. Khachaturyan, "Ordering in substitutional and interstitial solid solutions", Progress in Materials Science **22**, 1–150 (1978).

[23] T. Ishikawa and S.-y. Miyatani, "Electronic and ionic conduction in $Cu_{2-\delta}Se$, $Cu_{2-\delta}S$ and $Cu_{2-\delta}(Se,S)$", Journal of the Physical Society of Japan **42**, 159–167 (1977).

[24] Z. Vučić, O. Milat, V. Horvatić, and Z. Ogorelec, "Composition-induced phase-transition splitting in cuprous selenide", Physical Review B **24**, 5398–5401 (1981).

[25] B. Yu, W. Liu, S. Chen, H. Wang, H. Wang, G. Chen, and Z. Ren, "Thermoelectric properties of copper selenide with ordered selenium layer and disordered copper layer", Nano Energy **1**, 472–478 (2012).

[26] S. Ballikaya, H. Chi, J. R. Salvador, and C. Uher, "Thermoelectric properties of Ag-doped Cu_2Se and Cu_2Te", Journal of Materials Chemistry A **1**, 12478 (2013).

[27] T. W. Day, K. A. Borup, T. Zhang, F. Drymiotis, D. R. Brown, X. Shi, L. Chen, B. B. Iversen, and G. J. Snyder, "High-temperature thermoelectric properties of $Cu_{1.97}Ag_{0.03}Se_{1+y}$", Materials for Renewable and Sustainable Energy **3**, 1–7 (2014).

[28] T. P. Bailey, S. Hui, H. Xie, A. Olvera, P. F. P. Poudeu, X. Tang, and C. Uher, "Enhanced ZT and attempts to chemically stabilize Cu_2Se via Sn doping", Journal of Materials Chemistry A **4**, 17225–17235 (2016).

[29] K. Zhao, A. B. Blichfeld, E. Eikeland, P. Qiu, D. Ren, B. B. Iversen, X. Shi, and L. Chen, "Extremely low thermal conductivity and high thermoelectric performance in liquid-like $Cu_2Se_{1-x}S_x$ polymorphic materials", Journal of Materials Chemistry A **5**, 18148–18156 (2017).

Chapter 6

APPLICATION TO THERMOELECTRICS: MATERIAL QUALITY FACTOR

It has been shown through many examples that stationary charge transport can be phenomenologically characterized even when there is no satisfactory physical model to explain the phenomenology. As long as a transport function $\sigma_E(E)$ can be identified, predictions on how S, σ, and L will change upon changing E_F (*e.g.* doping) can be made. This predictive ability of the transport function makes it immediately useful for thermoelectric applications. In thermoelectrics, the figure-of-merit is a function of both E_F and material quality. Thus, knowing how transport properties change with respect to E_F allows one to understand the optimization process of different types of materials and also quantify the quality of materials. This process is referred to as the material quality factor analysis and effective mass modeling in thermoelectrics [1], which will be discussed in this chapter. The practical message of the method we introduce in this chapter is that, in contrary to the common belief, quality factor analysis and optimum doping analysis require neither a Hall measurement nor explicit determination of the effective mass.

6.1 Concept and derivation of the thermoelectric material quality factor

One of the primary goals for thermoelectric materials research is to develop materials with the best possible thermoelectric figure-of-merit, which is defined as

$$zT = \frac{S^2\sigma}{\kappa}T. \tag{6.1}$$

All transport properties constituting zT are functions of η as shown in Fig.6.1a (recall that η is defined positive when above the transport edge; *i.e.* positive when inside the band for band conductors). Thermal conductivity is also an increasing function of η because the electronic term κ_e is proportional to σ (Eq.1.23):

$$\kappa = \kappa_\mathrm{L} + L\sigma T + \kappa_\mathrm{B}. \tag{6.2}$$

Here, κ_L is lattice thermal conductivity. κ_B is bipolar (or ambipolar) thermal conductivity which will be neglected for now and later addressed separately in section 6.4. As a result of competing dependencies, zT is a peak function with respect to η. In material synthesis, η is controlled by tuning the carrier concentration

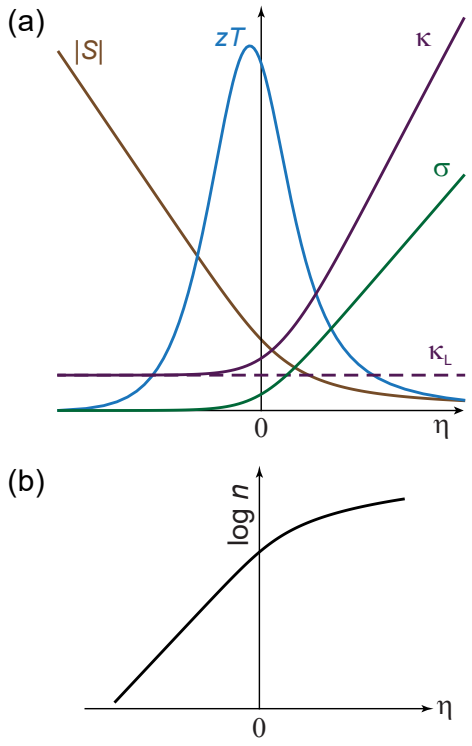

Figure 6.1: Thermoelectrics-related properties as a function of reduced Fermi-level. **(a)** Thermopower is a decreasing function with η whereas conductivity and thermal conductivity is an increasing function with η. Figure-of-merit is thus a peaked function with respect to η. **(b)** Carrier concentration is an increasing function with η and is the primary means for controlling η.

(Fig.6.1b), from which the concept of optimum doping originates. The optimum zT reached after tuning the carrier concentration is, obviously, dependent on the material. Some materials can reach higher zT values at optimum, which one could refer to as higher quality thermoelectric materials. Since zT depends on both the doping level and "material quality", a practical question is whether the two factors can be separated so that the material quality can be assessed before spending time and resources to optimally dope the material. The material quality factor is a tool that fulfills this purpose, a concept first devised by Chasmar and Stratton [2]. The concept was first introduced with the concepts relevant for band conductors, but here it will be derived based on phenomenological functions that do not necessarily require a particular physical system.

The goal of the derivation is to express zT with two independent variables: η and another independent variable which will be referred to as the quality factor B. Then, one can separate η dependencies from $zT(\eta, B)$ to find a convenient definition for B.

For this procedure, it is assumed that only one type of majority carrier dominates the transport. The zT equation (Eq.6.1) can be decomposed by identifying terms that only depend on η (for a given phenomenological exponent s):

$$\begin{aligned} zT(\eta, B) &= \frac{S^2\sigma}{\kappa_\mathrm{L} + L\sigma T}T \\ &= \frac{S^2}{\frac{\kappa_\mathrm{L}}{T\sigma} + L} \\ &= \frac{S^2(\eta)}{\frac{\kappa_\mathrm{L}}{T\sigma_{E_0} sF_{s-1}(\eta)} + L(\eta)} \\ &= \frac{S^2(\eta)}{\left(\frac{k_\mathrm{B}}{e}\right)^2 \frac{1}{B}\frac{1}{sF_{s-1}(\eta)} + L(\eta)}. \end{aligned} \tag{6.3}$$

Here, Eq.1.77 was used for decomposing conductivity. B combines all the η-independent material parameters, which was defined as

$$B = \left(\frac{k_\mathrm{B}}{e}\right)^2 \frac{\sigma_{E_0}}{\kappa_\mathrm{L}} T. \tag{6.4}$$

This expression defines the *dimensionless thermoelectric material quality factor* B. The natural unit of the Lorenz number $\left(\frac{k_\mathrm{B}}{e}\right)^2$ was multiplied to make B dimensionless[1]. The phenomenological exponent s was also excluded so that the definition of B could have the same expression regardless of the s exponent[2]. It is seen from Eq.6.3 that B determines the zT vs. η function; thus the peak zT value with respect to η and the optimum η at which the peak zT occurs are both determined for a given B. In other words, the material quality factor allows one to quantify the potential

[1]Some authors [3] use the non-dimensionless quality factor $\beta = B/\left(\frac{k_\mathrm{B}}{e}\right)^2$; however, β is much more inconvenient than B not just because of the awkward units but also because of the big numerical value on the order of 10^7 (in SI units). By contrast, B is elegantly normalized to a numerical value on the order of $10^{-1} - 10^0$.

[2]In the original introduction [2], B was defined from a parameter σ_0 that refers to the non-degenerate limit equation for conductivity such as $\sigma = \sigma_0 \exp(\eta)$. In the typical $s = 1$ case which is applicable to the majority of thermoelectric materials, $\sigma_0 = \sigma_{E_0}$ and therefore the definition in Eq.6.4 coincides with that in Ref.[2]. However, the original definition is an inconvenient choice for thermoelectrics in practice because thermoelectric materials are always optimized at small η values (heavily doped samples) which is far from the non-degenerate limit. The non-degenerate limit is often not accessible due to spontaneous defect formation, or is often a regime with a different scattering description not applicable to heavily doped samples. For this reason, some authors have reformulated the definition of B using parameters relevant for heavily doped semiconductors (such as μ_0 in Eq.1.52 or μ_w in Eq.1.53). Use of σ_{E_0} is analogous to such expressions, but keeps the definition at a phenomenological level. It should be noted that σ_{E_0} is related to the σ_0 parameter in Ref.[2] through $\sigma_{E_0} s\Gamma(s) = \sigma_0$. Therefore, the definition of B differs, for example, by a factor of $3\Gamma(3) = 6$ in the case of $s = 3$.

of a material to reach a certain zT value, and also provides a guideline for doping optimization. The approach works well as long as σ_{E_0} and κ_{L} are insensitive to η (in addition to having no bipolar conduction).

The correspondence between a particular B and zT vs. η curve depends on the phenomenological exponent s. Thus, comparison of B between materials require that the transport is described with the same s. Current interest is the case of $s = 1$ which is applicable to the majority of thermoelectric materials and also the special case of $s = 3$.

The zT vs. η curve for the case of $s = 1$ is shown in Fig.6.2a. Most thermoelectric materials, which are band conductors dominated by deformation potential scattering, fall into this category. It is seen that $B > 0.4$ is when the material is able to reach a $zT > 1$. This is a good reference value to use for evaluating "good" thermoelectric materials. The peak zT obtainable with each B value is plotted in Fig.6.2b.

The optimum η that yields the best zT for a given material is conveniently tracked by converting the optimum η into $|S|$ as shown in Fig.6.2c. It is seen that a material with $B > 0.4$ is optimized at $|S| > 240\ \mu\mathrm{V/K}$. For synthesis, carrier concentration could be an easier way to track optimization, but this requires knowledge of a density-of-states effective mass. Fig.6.2c plots the optimum carrier concentration (scaled with m^*_{DOS} and T) which could be used to find the target doping level. The Seebeck effective mass m^*_{Seeb} determined by combining S and n_{H} measurements[3] (Eqs.1.55 and 1.57) provides a good approximate for m^*_{DOS}.

The case of $s = 3$ is shown in Fig.6.3. At first glance the $s = 3$ case might appear to be more favorable than $s = 1$ because a higher zT is obtainable with a lower B factor. However, σ_{E_0} values for $s = 3$ cases are generally found to be much lower than those for $s = 1$ materials. See the discussion in section 3.2.

[3]The following approximate equations can be used do quickly determine m^*_{Seeb} within 2% without numerical integration. When $|S| > 75\ \mu\mathrm{V/K}$:

$$m^*_{\mathrm{Seeb}} \approx \frac{h^2}{2k_{\mathrm{B}}T}\left\{\frac{3n_{\mathrm{H}}}{16\sqrt{\pi}}\left(\exp\left[\frac{|S|}{(k_{\mathrm{B}}/e)} - 2\right] - 0.17\right)\right\}^{2/3}. \tag{6.5}$$

When $|S| < 75\ \mu\mathrm{V/K}$:

$$m^*_{\mathrm{Seeb}} \approx \frac{3h^2}{8\pi^2 k_{\mathrm{B}}T}\frac{|S|}{(k_{\mathrm{B}}/e)}\left(\frac{3n_{\mathrm{H}}}{\pi}\right)^{2/3}. \tag{6.6}$$

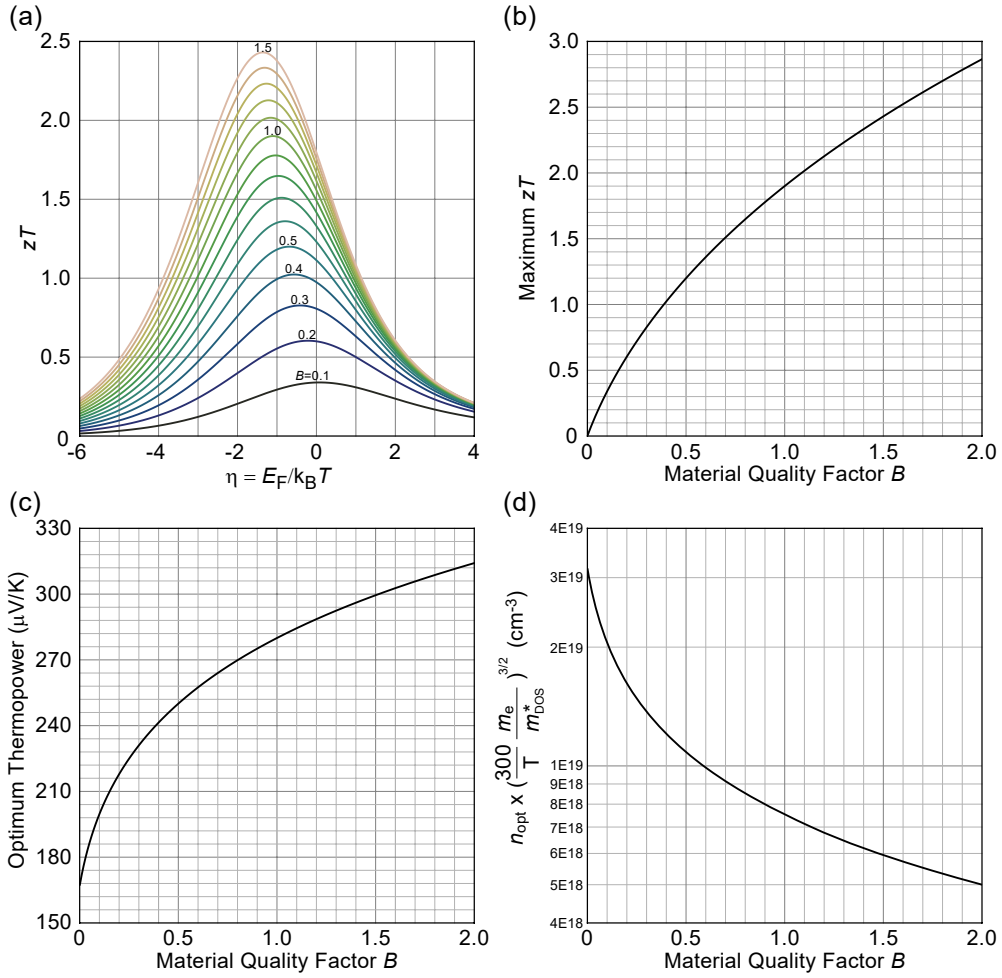

Figure 6.2: Quality factor analysis for $s = 1$, applicable to thermoelectric materials dominated by deformation potential scattering. **(a)** The $zT(\eta)$ curve is determined for a given B. The curves are calculated by substituting Eqs.1.77,1.79, and 1.80 into Eq.6.3. **(b)** The peak zT value for a given B. Note that $B = 0.4$ gives a peak $zT > 1$. **(c)** The optimum thermopower $|S|$ at at which the peak zT occurs **(d)** The optimum carrier concentration n_{opt} at which the peak zT occurs, multiplied by a scaling factor that depends on the density-of-states effective mass and temperature. Example calculation: at $B = 0.4$ the vertical axis reads 1.2×10^{19} /cm^3; if $m^*_{\text{DOS}} = 3m_{\text{e}}$ and $T = 500$ K, then $n_{\text{opt}} = 1.2 \times 10^{19} \cdot (\frac{500}{300} \times 3)^{3/2} = 1.3 \times 10^{20}$ /cm^3.

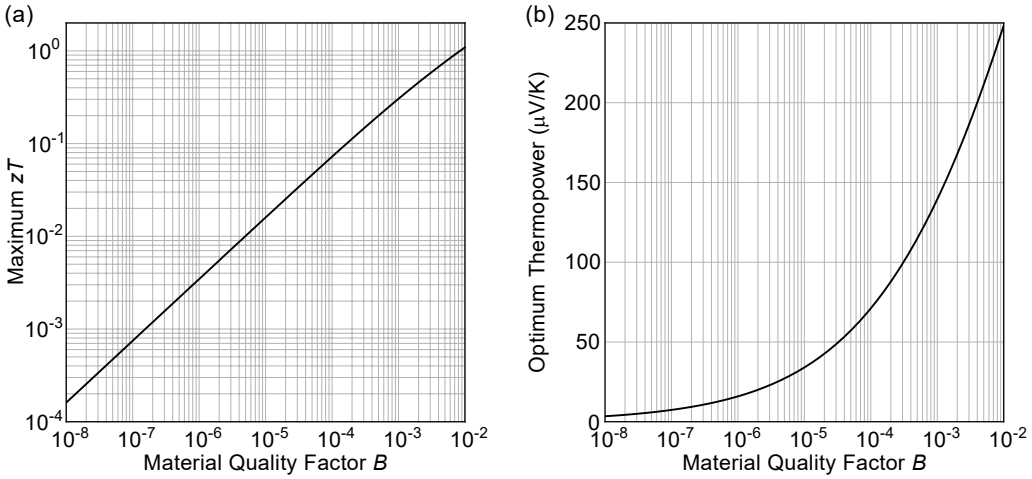

Figure 6.3: Quality factor analysis for $s = 3$. **(a)** The peak zT value for a given B. **(b)** The optimum thermopower at at which the peak zT occurs.

6.2 Determination of B from measurements on S, σ, and κ

B can be determined with at least one sample with measurements of S, σ, and κ at a given temperature of interest. In the literature, Hall measurements are also used, but as has been shown in the previous section a Hall measurement is not required for the derivation or determination of the quality factor. One does need to know the s exponent in prior, which would require a $S - \sigma$ analysis as was done in Ch.2. However, even when the transport mechanism is not well studied, $s = 1$ is a good initial guess that will usually turn out to be valid for most thermoelectric materials.

One needs to first find η of the sample, which could be done by finding the η that gives the measured Seebeck (Eq.1.79). Then, one could also calculate $L(\eta)$ from Eq.1.80, which allows one to calculate k_{L} from Eq.6.2 (assuming $\kappa_{\mathrm{B}} = 0$), which is one of the two values need to calculate B. The other need value σ_{E_0} can be simply obtained by dividing the measured σ with $sF_{s-1}(\eta)$ (calculated from the η obtained above) as was derived in Eq.1.77.

With this procedure outlined above, the explicit determination of the effective mass or mobility[4] is completely avoided (and proved redundant) for the determination of B. Hall measurements are only needed for mapping the optimum η to the optimum

[4]Historically, evaluation of B using mobilities has led to some inconsistencies due to the mix-matching of different mobility definitions. For $s = 1$ band conductors, σ_{E_0} can be written in terms of band parameters such as: $\sigma_{E_0} = \frac{8\pi e(2m_{\mathrm{e}}k_{\mathrm{B}}T)^{3/2}}{3h^3}\mu_{\mathrm{w}}$, where μ_{w} was defined in Eq.1.53 using μ_0. Some authors [4] use the notation "μ_0" to refer to the classical mobility μ_{cl}, which is the Drude mobility in the non-degenerate limit. The two are related by $\mu_{\mathrm{cl}} = 4/3\sqrt{\pi}\mu_0 \approx 0.75\mu_0$. Using μ_{cl} in place of μ_0 in the equations defined here causes a 25% underestimation in B.

carrier concentration.

6.3 Application to thermoelectric materials

Typical $s = 1$ materials

The B factor analysis with $s = 1$ applies to the most typical cases encountered in thermoelectric materials and has been discussed extensively in the literature [4]. Here, two non-typical cases are briefly noted.

First is the Cu_2Se case discussed previously in Ch.5. It has been shown how Hall measurements, the conventional means for determining B, are not easy to understand in this material. Instead, the approach using $S - \sigma$ to determine σ_{E_0} as explained in section 6.2 can be used to find B and also examine if the sample is properly doped to an optimum level. Fig.6.4 shows that the Li-doped sample is indeed at an optimum doping level, with a zT corresponding to that predicted by the calculated B factor.

Next is the case of PEDOT and PEDOS-based conducting polymers, previously discussed in Section 3.2 and Fig.3.4. Although the physical origin for $s = 1$ is not known in this case, since the phenomenology is identical to that of band conduction with deformation potential scattering, B factors can be compared. The quality factor

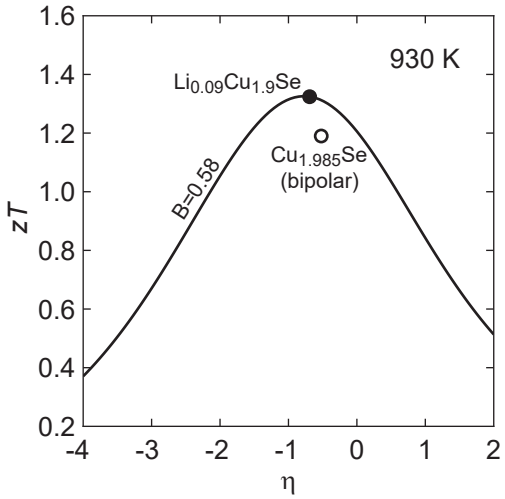

Figure 6.4: Quality factor analysis for Cu_2Se. The Li-doped sample (filled circle), calculated to have a quality factor of $B = 0.58$ at 930 K based on the data shown in Figs.5.3-5.5, appears to be doped to a near-optimum level. The undoped sample (open circle) has a similar B factor if the B of majority p-type carriers is inferred from extrapolation (Fig.5.4), but the actual zT is smaller due to the bipolar effect reducing the Seebeck coefficient. The η value of the undoped sample is an effective value converted from S with the non-bipolar equation (Eq.1.79).

for PEDOT:tosylate is evaluated as $B \approx 0.06$ at 300 K with $\sigma_{E_0} = 75$ S/cm and $\kappa_L \approx 0.3$ W/m·K. From Fig.6.2, this B value corresponds to a maximum $zT > 0.2$ at an optimum thermopower of $|S| \approx 190\ \mu$V/K. These values indeed agree well with those reported in Ref.[5]. Furthermore, the quality factor can be compared on the same scale with values from band conductors like Sb_2Te_3-Bi_2Te_3 where $B > 0.4$ at 300 K [6].

Conducting polymers with $s = 3$

In Ch.3, it was shown that most conducting polymers show $s = 3$. Again, this phenomenology makes it possible to find B despite of the physical origin being unknown. The polythiophene data compiled in 3.1 was fit with $\sigma_{E_0} = 2\times10^{-2}$ S/cm. Assuming $\kappa_L \approx 0.3$ W/m·K, $B > 10^{-5}$ (300 K) is obtained. From Fig.6.3, it is seen that this B value predicts a maximum $zT > 10^{-2}$ at an optimum thermopower of $|S| > 35\ \mu$V/K.

6.4 Quality factors for bipolar conduction and peak zT

So far, primary interest was on materials with a single type of carrier. In transport data on heavily doped semiconductors, the onset of bipolar conduction (*i.e.* the onset of minority carrier conduction) is most easily seen in the thermopower $|S|$ measured as a function of temperature, where it starts to roll over and show a sublinear increase as was shown in Fig.5.3 for undoped Cu_2Se. It is this bipolar conduction that makes the zT have a maximum at a peak temperature (unless the material stability limit is reached first) rather than increase indefinitely. Since the peak zT value is of popular interest in the thermoelectric research community, here it is discussed how an approach analogous to the quality factor analysis can be developed for predicting the peak zT value from material parameters.

With bipolar conduction, largely three additional phenomena must be addressed. One is the increased conductivity due to the minority carriers.

$$\sigma = \sigma_p + \sigma_n, \tag{6.7}$$

where σ now has two contributors, p- and n-type carriers, instead of one. This increase, by itself, is beneficial for thermoelectrics, but greatly outweighed by the other two effects. The first is a decrease in thermopower because of the canceling effect of the two different carriers (derived from Eq.1.28 by separately considering n- and p-type contributions):

$$S = \frac{S_p\sigma_p + S_n\sigma_n}{\sigma}. \tag{6.8}$$

Here, S_p and S_n will have different signs, decreasing the magnitude of S. Lastly, bipolar (or ambipolar) thermal conduction[5] starts to contribute to thermal conductivity in Eq.6.2:

$$\kappa_\mathrm{B} = \frac{\sigma_\mathrm{p}\sigma_\mathrm{n}}{\sigma}(S_\mathrm{p} - S_\mathrm{n})^2 T. \tag{6.9}$$

This term is derived in the appendix of this chapter (section 6.5). This additional term is based on very general thermodynamic phenomenology, occurring whenever there is parallel conduction by two different types of carriers. It allows the electronic conduction to produce more heat transport than for each individually combined.

The equation for zT reflecting the bipolar conducting phenomena becomes

$$zT = \frac{\left(\frac{S_\mathrm{p}\sigma_\mathrm{p}+S_\mathrm{n}\sigma_\mathrm{n}}{\sigma}\right)^2\left(\sigma_\mathrm{p}+\sigma_\mathrm{n}\right)}{\kappa_\mathrm{L}+L_\mathrm{p}\sigma_\mathrm{p}T+L_\mathrm{n}\sigma_\mathrm{n}T+\frac{\sigma_\mathrm{p}\sigma_\mathrm{n}}{\sigma}(S_\mathrm{p}-S_\mathrm{n})^2 T} T. \tag{6.10}$$

As for the derivation of B, η dependencies can be separated from material property terms. A number of new terms can be defined to make this process more transparent. The contributing fraction of each carrier to conductivity is defined as $f_i = \sigma_i/\sigma$. Dimensionless properties $S' = S/(k_\mathrm{B}/e)$ and $L' = L/(k_\mathrm{B}/e)^2$ are defined. The quality factor for p- and n-type conductors are separately defined such as

$$B_i = \left(\frac{k_\mathrm{B}}{e}\right)^2 \frac{\sigma_{E_0,i}}{\kappa_\mathrm{L}} T. \tag{6.11}$$

Finally, the reduced Fermi-level of each carrier type is defined separately. That is, η_p and η_n are each defined with respect the transport edges (band edges) of p- and n-type, respectively, and each of them are positive when moving into their respective bands. Assuming $s = 1$ for both carrier types, the zT equation reduces to

$$zT = \frac{\left(f_\mathrm{p}S'_\mathrm{p}+f_\mathrm{n}S'_\mathrm{n}\right)^2}{\frac{1}{B_\mathrm{p}F_0(\eta_\mathrm{p})+B_\mathrm{n}F_0(\eta_\mathrm{n})}+f_\mathrm{p}L'_\mathrm{p}+f_\mathrm{n}L'_\mathrm{n}+f_\mathrm{p}f_\mathrm{n}\left(S'_\mathrm{p}-S'_\mathrm{n}\right)^2}. \tag{6.12}$$

It is noticed from Eq.6.12 that

$$zT = zT(B_\mathrm{p}, B_\mathrm{n}, \eta_\mathrm{p}, \eta_\mathrm{n}). \tag{6.13}$$

Temperature dependency is only implicit through B_i terms. The η_i terms are restricted through

$$-(\eta_\mathrm{p} + \eta_\mathrm{n}) = \eta_\mathrm{g} = \frac{E_\mathrm{g}}{k_\mathrm{B}T}. \tag{6.14}$$

[5] Some authors [7–9] classify this bipolar term as part of κ_e. Here, it is kept separate to make a clear distinction from the κ_e contribution through the Wiedemann–Franz law.

Here, E_g is the band gap (only positive gaps are of interest here). While temperature is unrestricted, the reduced band gap η_g can be any value.

From Eq.6.13, it is seen that, for a given set of (B_p, B_n), *i.e.* for a given material with an unspecified or unrestricted band gap, zT is a function of only (η_p, η_n). Furthermore, since zT is a peaked function (with two peaks from the majority carrier being either p- or n-type; the following arguments apply for any of those two peaks), the peak in zT for a given (B_p, B_n) will always occur at $(\eta_p, \eta_n)_{peak}$. A corollary is that, the peak in zT always occurs at a fixed $(\eta_g)_{peak}$ for a given (B_p, B_n).

Next, assume that the band gap is also given so that information about the material is complete: with a given (B_p, B_n, E_g), the temperature T_{peak} at which the peak zT occurs is decided because $k_B T_{peak} = E_g/(\eta_g)_{peak}$, where $(\eta_g)_{peak}$ is determined by (B_p, B_n). The relation is somewhat recursive because the B_i's actually depend on T, which is taken into account for now by referring to $(B_i)_{peak}$. Now, the goal is to extract the two independent parameters from $[(B_p)_{peak}, (B_n)_{peak}, E_g]$ that will dictate $(zT)_{peak}$ (it has been identified in the previous argument that there should be only two independent variables that determine $(zT)_{peak}$). The first independent variable is $(B_n/B_p)_{peak}$, which is simply $(\sigma_{E_0,n}/\sigma_{E_0,p})_{peak}$. Recall that, for deformation potential scattering, σ_{E_0} is ideally temperature-independent. Even when it is moderately dependent on temperature, the dependency is likely to be similar for the two types of carriers. Therefore, it seems fairly general to use $\sigma_{E_0,n}/\sigma_{E_0,p}$, not necessarily restricted to a temperature of $T = T_{peak}$. Next, we identify that

$$(B_n)_{peak} = \left(\frac{k_B}{e}\right)^2 \frac{\sigma_{E_0,n}}{\kappa_L} T_{peak} = \left(\frac{k_B}{e}\right)^2 \frac{\sigma_{E_0,n}}{\kappa_L} \frac{E_g}{k_B (\eta_g)_{peak}}. \tag{6.15}$$

Again, the peak subscript was dropped from $\sigma_{E_0,n}$, anticipating a nearly temperature independent value. Notice here that $(\eta_g)_{peak}$ is what is already determined by $(B_n)_{peak}$ and $\sigma_{E_0,n}/\sigma_{E_0,p}$ which makes it a redundant term for extracting independent variables. Finally, the p- and n-type is replaced with minority and majority carriers, because the interest usually is in the peak zT obtainable with majority carriers regardless of its type. Therefore, we can write $(zT)_{peak}$ as a function of two independent dimensionless variables:

$$(zT)_{peak} = f\left(\frac{k_B}{e^2} \frac{\sigma_{E_0,major}}{\kappa_L} E_g\,,\ \frac{\sigma_{E_0,major}}{\sigma_{E_0,minor}}\right). \tag{6.16}$$

These two independent variables could be defined as the set of dimensionless material quality factors for peak zT. For a more linear prediction of peak zT, a square

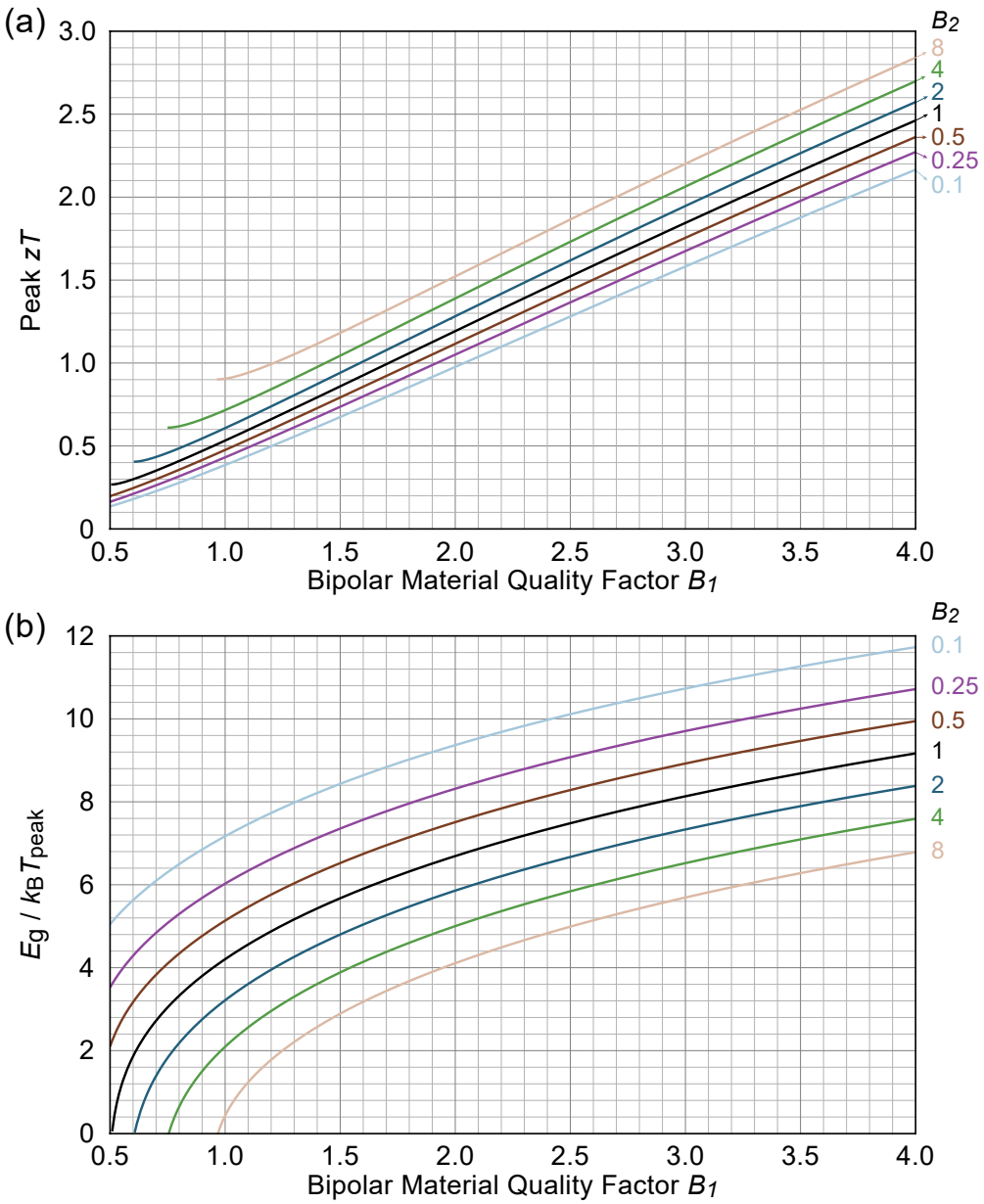

Figure 6.5: Peak zT and T_{peak} due to majority carriers from the quality factors (B_1, B_2) for bipolar conductors. **(a)** The peak zT value obtainable for given quality factors (B_1, B_2). **(b)** The reduced band gap E_g/k_BT at which the peak zT occurs. Example calculation: if $B_2 = 1$ and $B_1 = 1.7$, the peak zT obtainable is $zT \approx 1$; this peak zT occurs at a reduced gap $E_g/k_BT \approx 6.1$; if the band gap is $E_g = 0.3$ eV, then the peak zT would occur at $0.3\text{ eV}/6.1k_B \approx 570\ K$.

root is taken on the first:

$$(B_1, B_2) = \left(\sqrt{\frac{k_B}{e^2} \frac{\sigma_{E_0,\text{major}}}{\kappa_L} E_g} \, , \, \frac{\sigma_{E_0,\text{major}}}{\sigma_{E_0,\text{minor}}} \right). \tag{6.17}$$

The relation between $(zT)_{\text{peak}}$ and (B_1, B_2) is plotted in Fig.6.5a. It is seen that the $(zT)_{\text{peak}}$ is approximately linear with respect to B_1 for a given B_2 in the practical range. Fig.6.5b shows how η_g changes with the bipolar quality factors, allowing one to deduce T_{peak} from a known E_g or the other way around.

The bipolar quality factor analysis also provides a quantitative evaluation of how T_{peak} is increased from an enlarged band gap. For a fixed (B_1, B_2), $T_{\text{peak}} \propto E_g$ as shown in Fig.6.5b. In real materials, however, B_1 and E_g are correlated [10, 11], where an increase in E_g (*e.g.* by alloying) results in a decreased B_1 due to an increased band effective mass [12]. As a result, the increase in T_{peak} from an enlarged E_g is somewhat more than the linear scaling. For example, assume a material with $(B_1, B_2) = (2, 1)$ and band gap 0.2 eV. From Fig.6.5b, $\eta_g \approx 6.7$ meaning that $T_{\text{peak}} \approx 350$ K. Then, assume that the band gap is enlarged to 0.25 eV at the expense of a decrease in B_1 to 1.8. The simple scaling relation would suggest an increase in T_{peak} to ≈ 430 K, but the reduced B_1 now means $\eta_g \approx 6.3$ which gives $T_{\text{peak}} \approx 460$ K.

This method of evaluating T_{peak} could be useful for high throughput material searching where a proper descriptor is needed to evaluate the potential of a material. Using the band gap as one of the descriptors is common in high throughput material searching and screening [13–15], but there is no good descriptor for T_{peak} other than the qualitative understanding that narrow gap materials give a lower T_{peak}. Use of (B_1, B_2) can provide this information. For example, to screen for the requirement of $T_{\text{peak}} > 300$ K, one could look for $E_g/(\eta_g)_{\text{peak}} > 300$ K, where $(\eta_g)_{\text{peak}}$ can be found from a look up table similar to that of Fig.6.5b.

The benefit of having a large B_2, demonstrated in Fig.6.5, highlights the significance of having a high contrast in the weighted mobility between the majority and minority carriers (in band conductors, the ratio of σ_{E_0}'s is equivalent to the ratio of μ_w's). High valley degeneracy in the majority carrier band is one of the electronic structures that could give rise to a high B_2. Many n-type Zintl compounds and related materials are predicted to have high valley degeneracy in the conduction band (and low degeneracy in the valence band) [16–19], which would result in a high B_2.

6.5 Appexdix: Derivation of bipolar thermal conductivity

Here, the electronic bipolar thermal conductivity (ambipolar diffusion thermal conductivity), shown in Eq.6.9, is derived. Although originally studied in the context of bipolar conduction [7], it will be shown that whenever there are two different types of electronic carriers contributing to conduction in parallel channels, there is additional thermal transport [9]. In fact, even when the two carriers are both n-type (or both p-type), there is additional thermal transport if those two carriers have different individual Seebeck coefficients (as suggested by Eq.6.9). The effect is simply much larger when the two carriers have opposite signs in the Seebeck coefficient.

Assume the presence of two types of electronic carriers p and n, which will be noted with italic subscripts. Although labeled p and n, each does not necessarily have to be p- or n-type in this derivation (they can be any type). Recall the heat flux equation in the presence of both an electric field and temperature gradient (Eq.1.26) which can be rewritten by taking into account of the carrier types:

$$\boldsymbol{U} = TS\sigma\boldsymbol{E} - (\kappa_{0,p} + \kappa_{0,n})\nabla T. \tag{6.18}$$

Here, S and σ are now that from the combined contribution from both types as in Eqs.6.7 and 6.8. Since thermal conductivity is defined in the zero current condition (*i.e.* $\boldsymbol{J} = 0$), $\boldsymbol{E}$ is substituted with $S\nabla T$:

$$\boldsymbol{U}|_{\boldsymbol{J}=0} = -(-TS^2\sigma + \kappa_{0,p} + \kappa_{0,n})\nabla T = -\kappa\nabla T. \tag{6.19}$$

The electronic thermal conductivity in the presence of only one type of carrier is $\kappa_{e,i} = \kappa_{0,i} - TS_i^2\sigma_i$ (Eq.1.29). Then substituting $\kappa_{0,i}$'s in Eq.6.19 gives

$$\begin{aligned}\kappa &= \kappa_{e,p} + \kappa_{e,n} + TS_p^2\sigma_p + TS_n^2\sigma_n - TS^2\sigma \\ &= \kappa_{e,p} + \kappa_{e,n} + \frac{\sigma_p\sigma_n}{\sigma}\left(S_p - S_n\right)^2 T \\ &= \kappa_{e,p} + \kappa_{e,n} + \kappa_B.\end{aligned} \tag{6.20}$$

Setting p =p-type and n =n-type gives Eq.6.9, the bipolar thermal conductivity.

References

[1] S. D. Kang and G. J. Snyder, "Transport property analysis method for thermoelectric materials: material quality factor and the effective mass model", arXiv:1710.06896 [cond-mat.mtrl-sci], https://arxiv.org/abs/1710.06896.

[2] R. P. Chasmar and R. Stratton, "The thermoelectric figure of merit and its relation to thermoelectric generators", Journal of Electronics and Control **7**, 52–72 (1959).

[3] A. F. May and G. J. Snyder, "Introduction to modeling thermoelectric transport at high temperatures", in *Materials, preparation, and characterization in thermoelectrics*, edited by D. M. Rowe (CRC Press, 2012), pp. 1–18.

[4] H. Wang, Y. Pei, A. D. LaLonde, and G. J. Snyder, "Material design considerations based on thermoelectric quality factor", in *Thermoelectric nanomaterials: materials design and applications*, edited by K. Koumoto and T. Mori (Springer-Verlag Berlin Heidelberg, 2013), pp. 3–32.

[5] O. Bubnova, Z. U. Khan, A. Malti, S. Braun, M. Fahlman, M. Berggren, and X. Crispin, "Optimization of the thermoelectric figure of merit in the conducting polymer poly(3,4-ethylenedioxythiophene)", Nature Materials **10**, 429–433 (2011).

[6] H.-S. Kim, N. A. Heinz, Z. M. Gibbs, Y. Tang, S. D. Kang, and G. J. Snyder, "High thermoelectric performance in $(Bi_{0.25}Sb_{0.75})_2Te_3$ due to band convergence and improved by carrier concentration control", Materials Today **20**, 452–459 (2017) 10.1016/j.mattod.2017.02.007.

[7] P. Price, "CXXXV. Ambipolar thermodiffusion of electrons and holes in semiconductors", Philosophical Magazine **46**, 1252–1260 (1955).

[8] C. J. Glassbrenner and G. A. Slack, "Thermal conductivity of silicon and germanium from 3°K to the melting point", Physical Review **134**, A1058–A1069 (1964).

[9] J. R. Drabble and H. J. Goldsmid, "The electronic part of the therml conductivity in semiconductors", in *Thermal conduction in semiconductors* (Pergamon Press, 1961) Chap. 4, pp. 104–119.

[10] W. G. Zeier, A. Zevalkink, Z. M. Gibbs, G. Hautier, M. G. Kanatzidis, and G. J. Snyder, "Thinking like a chemist: intuition in thermoelectric materials", Angewandte Chemie International Edition **55**, 6826–6841 (2016).

[11] J. O. Sofo and G. D. Mahan, "Optimum band gap of a thermoelectric material", Physical Review B **49**, 4565–4570 (1994).

[12] K. Imasato, S. D. Kang, S. Ohno, and G. J. Snyder, "Band engineering in Mg_3Sb_2 by alloying with Mg_3Bi_2 for enhanced thermoelectric performance", Materials Horizons **5**, 59–64 (2018) 10.1039/C7MH00865A.

[13] J. Yang, H. Li, T. Wu, W. Zhang, L. Chen, and J. Yang, "Evaluation of half-Heusler compounds as thermoelectric materials based on the calculated electrical transport properties", Advanced Functional Materials **18**, 2880–2888 (2008).

[14] S. Wang, Z. Wang, W. Setyawan, N. Mingo, and S. Curtarolo, "Assessing the thermoelectric properties of sintered compounds via high-throughput *ab-initio* calculations", Physical Review X **1**, 021012 (2011).

[15] W. Chen, J.-H. Pöhls, G. Hautier, D. Broberg, S. Bajaj, U. Aydemir, Z. M. Gibbs, H. Zhu, M. Asta, G. J. Snyder, B. Meredig, M. A. White, K. Persson, and A. Jain, "Understanding thermoelectric properties from high-throughput calculations: trends, insights, and comparisons with experiment", Journal of Materials Chemistry C **4**, 4414–4426 (2016).

[16] G. K. H. Madsen, "Automated search for new thermoelectric materials: the case of LiZnSb", Journal of the American Chemical Society **128**, 12140–12146 (2006).

[17] S. Ohno, K. Imasato, S. Anand, H. Tamaki, S. D. Kang, P. Gorai, H. K. Sato, E. S. Toberer, T. Kanno, and G. J. Snyder, "Phase boundary mapping to obtain n-type Mg_3Sb_2-based thermoelectrics", Joule **2**, 141–154 (2018) 10.1016/j.joule.2017.11.005.

[18] B. R. Ortiz, P. Gorai, L. Krishna, R. Mow, A. Lopez, R. McKinney, V. Stevanovic, and E. S. Toberer, "Potential for high thermoelectric performance in n-type Zintl compounds: a case study of Ba doped $KAlSb_4$", Journal of Materials Chemistry A **5**, 4036–4046 (2017).

[19] B. R. Ortiz, P. Gorai, V. Stevanović, and E. S. Toberer, "Thermoelectric performance and defect chemistry in n-type Zintl $KGaSb_4$", Chemistry of Materials **29**, 4523–4534 (2017).

Chapter 7

SEEBECK METROLOGY: THERMOCOUPLE PROBE ISSUES AND IMPROVEMENT STRATEGIES

How information of the Seebeck coefficient can add much insight into the understanding of solids has been shown throughout the previous chapters. Measuring the Seebeck coefficient is a relatively easy experiment, and many commercial instruments offer the capability to quickly obtain a Seebeck value. However, in contrast to the easiness of the measurement itself, ensuring the accuracy of a Seebeck measurement is a very challenging process. Several concerns regarding popular measurement systems have been raised, but the general lack of appreciation on the issue, partly stemming from the reward system in the modern research community where there is little incentive to scrutinize such issues, has limited improvements in the Seebeck metrology.

In this chapter, measurement issues related to the thermocouple probe are discussed. This is a topic that has not been discussed much compared with other issues such as the cold-finger effect in four-probe measurements systems. Ongoing experimental effort to resolve some of the probe issues are discussed.

7.1 Limitations in using conventional thermocouples as probes

A Seebeck measurement requires the simultaneous measurement of temperature and voltage on a sample (Eq.1.13). Thermocouples are used as the sample probes because the couple junction gives a measurement of the temperature and those same wires can be used to measure the voltage at two sample terminals (Fig.7.1). Most popularly used in Seebeck measurements are type K (Chromel alloy Ni90–Cr10 wt.% as p-wire; Alumel alloy Ni95–Mn2–Al2–Si1 wt.% as n-wire) and type S (Pt90–Rh10 wt.% as p-wire; Pt as n-wire) thermocouples. Customized couples of Chromel/Nb or W/Nb are also used by a number of groups [2]. Limitations of these thermocouples will be discussed in this section.

First to be pointed out is that a near-zero thermopower is preferred as one of the thermocouple wires, so that it could be used as the voltage probing wire that contacts with the sample (*i.e.* red wire in Fig.7.1). This requirement is related to the voltage and temperature probe position difference illustrated in Fig.7.1, which

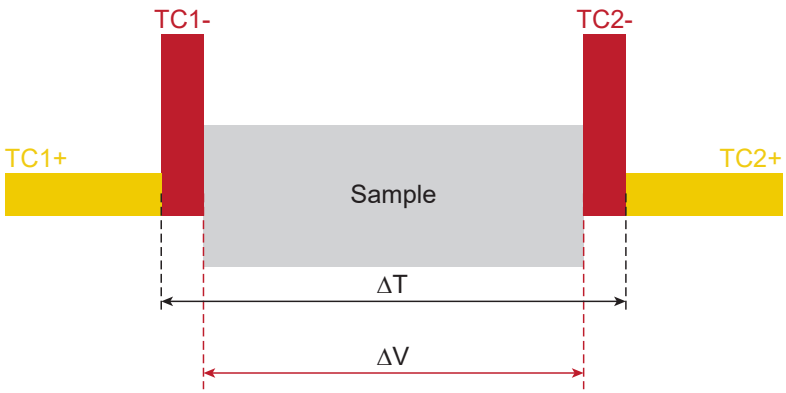

Figure 7.1: Schematic of the thermocouple placement on a sample for Seebeck measurements. The temperature difference ΔT is measured between two thermocouple junctions, whereas the voltage difference ΔV is measured between the two sample terminals. This position difference for ΔT and ΔV contributes to an error in the Seebeck coefficient measurement. Another source of error is the temperature difference between the two probe wire contacts (red wire contacts with the sample). Because the temperatures are different, an additional voltage from the red wire Seebeck coefficient is measured in ΔV, which should be corrected from the measurement. However, that correction relies on the measured ΔT, which is from a different position. Therefore, the error due to the position difference between ΔV and ΔT is amplified with this second source of error.

is an inherent problem in any thermocouple-sample contact geometry. This error is minimized by avoiding the use of junction beads (welded junctions in commercial thermocouples) and also by using wires as thin as possible; nevertheless the error cannot be completely eliminated. Then, this error propagates into the probe wire Seebeck voltage that must be corrected from the measured voltage difference ΔV. This second error related to the wire thermoelectric voltage can be minimized if the wire Seebeck coefficient is close to zero. Nb is a very good metal in this regards because its thermopower is $|S| < 2\ \mu\mathrm{V/K}$ up to around 750 °C as shown in Fig.7.2. Standard thermocouples like type K or type S are not ideal for this issue because of the large Seebeck coefficient on both p- and n-wires.

Next is the reactivity of the thermocouple with sample materials. While thermocouple reactivity is a sample specific issue, there are some important general tendencies. Pt-based type S thermocouples are considered to be one of the most stable materials being resistant against oxidation; thus they are often used for standard references and for measurements on oxides where an oxygen atmosphere might be needed. However, Pt is reactive with many chalcogenide or pnictide materials, or with the vapor

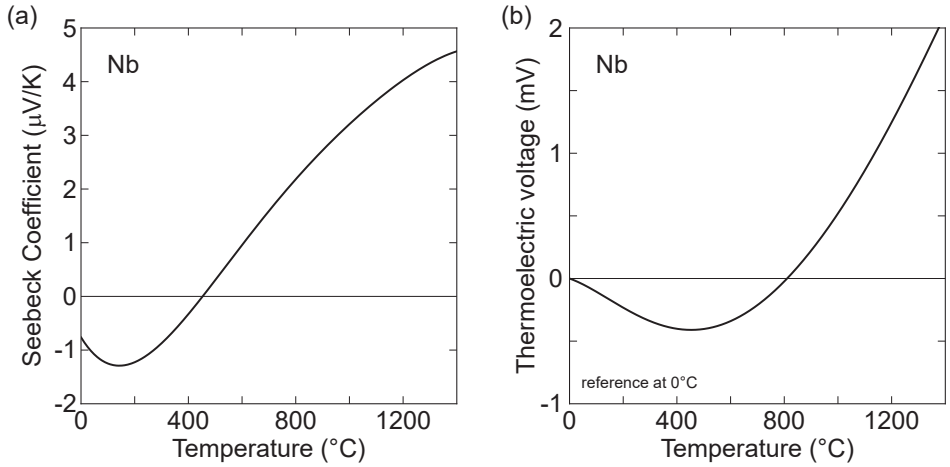

Figure 7.2: Thermoelectric properties of Nb. **(a)** Seebeck coefficient **(b)** Thermoelectric voltage with respect to a reference junction at 0°C. Curves are based on data from Ref.[1].

pressure produced from those materials (for example, see Fig.7.3 demonstrating the reactivity of Pt with Sb vapor pressure). For thermoelectric research where much of the high performance materials are chalcogenides or pnictides, this issue could be a potential issue for both thermocouple degradation and inaccurate measurements. It is not well studied if a reaction concurrent to the measurement could contribute to additional voltages (*e.g.* temperature dependent electrochemical potentials), but such hypothetical scenarios would be able to explain some unexplained systematic tendencies observed when measuring thermoelectric materials with type S thermocouples. In both Type K and Chromel/Nb thermocouples, the Ni contained in the Chromel alloy is of primary concern. Although Ni is generally stable with most materials at moderate temperatures, at higher temperatures it becomes reactive with many materials. For example, Chromel reactivity with Cu_2Se has been observed at above 600 °C in the course of studies presented in Ch.5, even when Graphoil (flexible graphite) was placed between the thermocouple and the sample. 500-600 °C is considered as a general guideline for the upper limit in measurements on thermoelectric materials. In this regard, Nb and W are excellent materials because they are inert against most thermoelectric materials up to higher temperatures above 750 °C.

Last is the small thermopower at low temperatures leading to a limited temperature range where the thermocouples remain practical. W has a thermopower of $|S| < 5$ μV/K below 100 °C. As a result, a W/Nb couple, which is one of the most inert thermocouples at high temperatures for thermoelectric materials, only

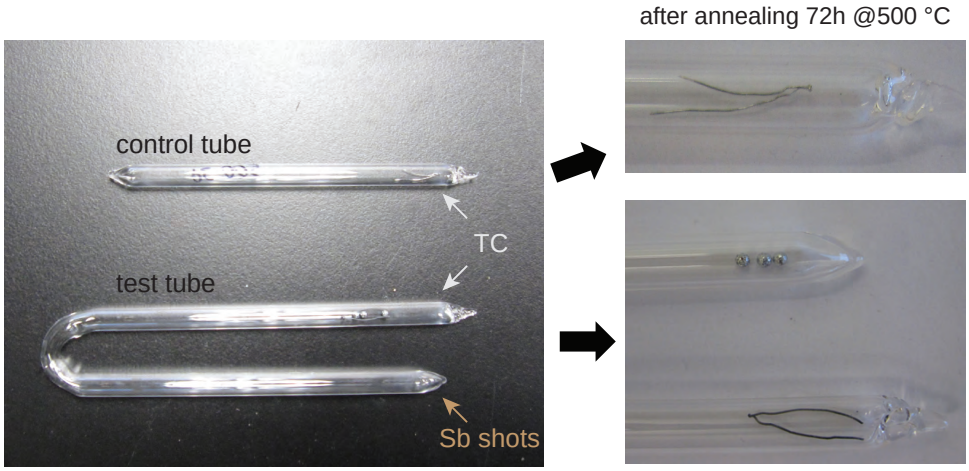

Figure 7.3: Pt reactivity with Sb vapor pressure. A type S thermocouple was sealed in a vacuumed fused quartz tube together with shots of Sb. The thermocouple and Sb were placed at opposite ends of the tube. After annealing at 500 °C, the thermocouple exposed to Sb vapor pressure turned black while no visual sign of Sb deposition was observed at any other places in the tube. Compare with the control where the thermocouple remained intact after the identical annealing conditions but without the Sb vapor pressure.

produces ≈ 0.3 mV for a 0-100 °C difference (Fig.7.4). This does not only mean that the measurement signal is susceptible to noise, but also that the thermocouple calibration table accuracy could be limited around room temperature. It is empirically known that W/Nb thermocouples yield poor measurements at <200 °C. This limited range becomes inconvenient in the study of wide temperature materials because one often needs to combine two measurements, one with Chromel/Nb for near room temperature and then another with W/Nb for high temperature to get one full data set.

7.2 Candidate thermocouples and testing

To overcome the limitations of Chromel/Nb or W/Nb, it is desired to have a p-wire that could replace Chromel and W: a material that is inert with most chalcogenides or pnictides, usable up to high temperatures (minimally > 750 °C), and with a sufficiently large thermopower at room temperature to produce > 1 mV for a 0-100 °C difference. The first candidate is the p-wire of type C thermocouples, which is a W-based alloy (W95–Re5 wt.%, abbreviated W95Re5 hereafter) that shares much of the features of W but with a higher low temperature thermopower due to the addition of Re. Since type C is an industry-level standard thermocouple (although

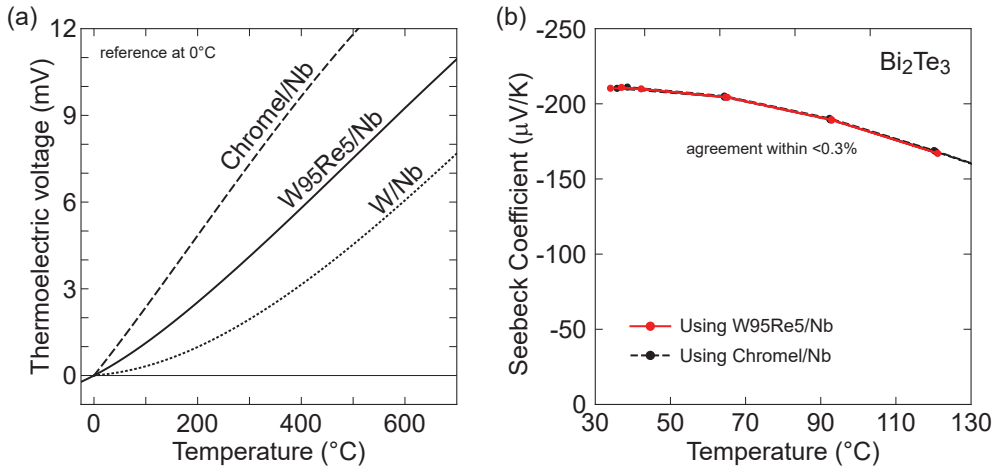

Figure 7.4: W95Re5/Nb thermocouples for Seebeck measurements. **(a)** Calibrated thermoelectric voltage of W95Re5/Nb with respect to a reference junction at 0°C (solid line), compared with type Chromel/Nb (dashed line) and W/Nb thermocouples (dotted line). Calibration was done by putting W95Re5/Nb in contact with a type S thermocouple in a vacuum furnace, and repeating heating and cooling cycles while recording voltage readings. Chromel data is from ITS-90 [3, 4]; W data is from Refs.[5, 6]; Nb data is from Fig.7.2. **(b)** Near room-temperature measurement test on a Bi_2Te_3 sample. The Seebeck coefficients measured using pristine W95Re5/Nb thermocouples agree well with those made using Chromel/Nb thermocouples.

not ANSI standard), it is expected to meet the other basic stability requirements as a thermocouple. However, it will be shown in this section that, surprisingly, the W-Re alloy lacks the basic stability required for use in the < 1000 °C range. Other candidate materials will be discussed at the end.

Measurement tests in Fig.7.4 show that the signal level of the W95Re5/Nb thermocouple is good enough to make reliable Seebeck measurements near room temperature. For the test, high purity W95Re5 wires were purchased from GoodFellow (W025120). The thermoelectric voltage table for reading temperatures was calibrated against a type S thermocouple. The results (Fig.7.4a) show signal level intermediate between Chromel/Nb and W/Nb. Especially near room temperature, where the W/Nb shows a slope approaching zero in the voltage curve, W95Re5/Nb maintains a finite slope. Using the calibration table and pristine W95Re5/Nb thermocouples, Seebeck measurements on a Bi_2Te_3 sample were made. As shown in Fig.7.4b, the results showed very good agreement with the results measured using Chromel/Nb thermocouples.

In the stability test, however, the W95Re5/Nb couple showed drift that resulted

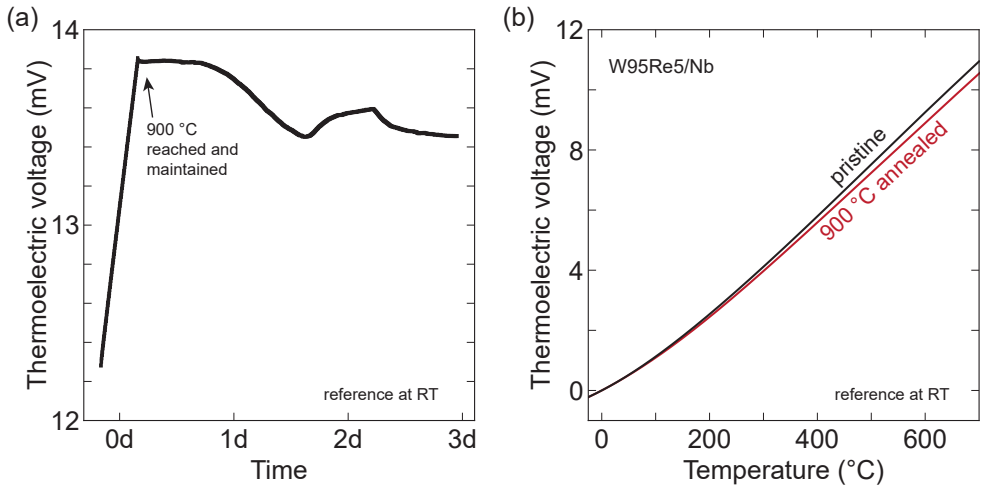

Figure 7.5: Drift in the thermoelectric voltage signal in W95Re5/Nb thermocouples. **(a)** During a 3d annealing test at 900 °C, a reduction in the thermoelectric voltage is observed. **(b)** The resulting voltage curve after the 900 °C annealing shows a permanent reduction in signal.

in permanent reduction in the voltage signal. Fig.7.5 shows the result from a 900 °C annealing test revealing the stability problem. It is rather unexpected for a thermocouple used widely in the industry for high temperature environments to exhibit such drift behavior. An interesting report by Williams *et al.* indicates that the phase boundary for Re solubility could be incorrect in the phase diagram; from studies on the W95Re5 composition, Re was found to precipitate from irradiation at 900 °C [7]. The driving force for Re precipitation would explain the reduction in the Seebeck coefficient because without Re the main phase W has a much smaller Seebeck coefficient. Decalibration of type C thermocouples at higher temperatures (1200-1500 °C) has also been noted in Ref.[8]. The findings in this section and the few literature reports suggest that one may have to be cautious for using type C thermocouples, not just for Seebeck measurements but for any instrumentation.

What could be another candidate if W95Re5 does not work? To avoid concerns about precipitation, it seems best to use single element materials that share the key properties of W95Re5. Single element refractory metals other than W and Nb are Re, Ta, Mo. Out the three, Mo seems to be promising candidate. It has the highest Seebeck coefficient among the three ($S > 6\ \mu$V/K near room temperature [1]), much more ductile than W, and known to be inert against a large variety of thermoelectric materials.

7.3 Thermocouple vacuum feedthroughs: issues in commercial products and custom solutions

One of the unfortunate customs in temperature measurement is the use of thermocouple extension wires. They are cheap alternatives of the actual thermocouple material that *approximately* match the thermoelectric voltage curve of the real thermocouple. Because they are only approximately matched, any temperature difference between the extension wire terminals contribute to measurement errors. Unless making extensions across virtually isothermal environments, use of extension wires should be avoided. Often it is not clearly specified by vendors or manufacturers whether their product use extension wires or not, and more than often they are used even when the specifications suggest otherwise.

The problem is much more serious for Seebeck measurements. The extension wires are made of completely different material, and the approximate matching in signal is only designed to be achieved in *pairs*. The Seebeck coefficient of the individual extension wire (*e.g.* the p-leg extension wire of type C) could even have a different sign than the original thermocouple material. Now, recall that for the sample voltage measurement in a Seebeck measuring setup, only one wire (not the pair) is used, and the subtraction of wire-contributed thermoelectric voltage is necessary. In this case, use of extension wire means that one would be erroneously correcting the measured voltage (which could even be of different sign to only make the the error bigger by the "correction"). Therefore, for Seebeck measurements the use of extension wires should be avoided altogether.

The problem with avoiding the use of extension wires is that it is sometimes not possible by just using commercially available products. To feed the thermocouple wires into a vacuum chamber, one needs a vacuum feedthrough. However, almost all commercial vacuum feedthroughs are made with extension grade material, not the actual thermocouple material (testing products that were advertised to use the actual thermocouple material showed that it was just false advertising possibly due to ignorance). Building a reference junction inside the chamber is also not a convenient solution.

Here, a very easy way to build custom vacuum feedthroughs with almost any type of wires is introduced. The idea is to pass thermocouple wires through thin gas tubes (typically 1/4 in.) and seal the inner tube with vacuum-rated sealants. Then the gas tube could be fed into the chamber through commercially available gas feedthroughs. TorrSeal (Agilent) is a good sealant epoxy that could be used. It is rated for ultra

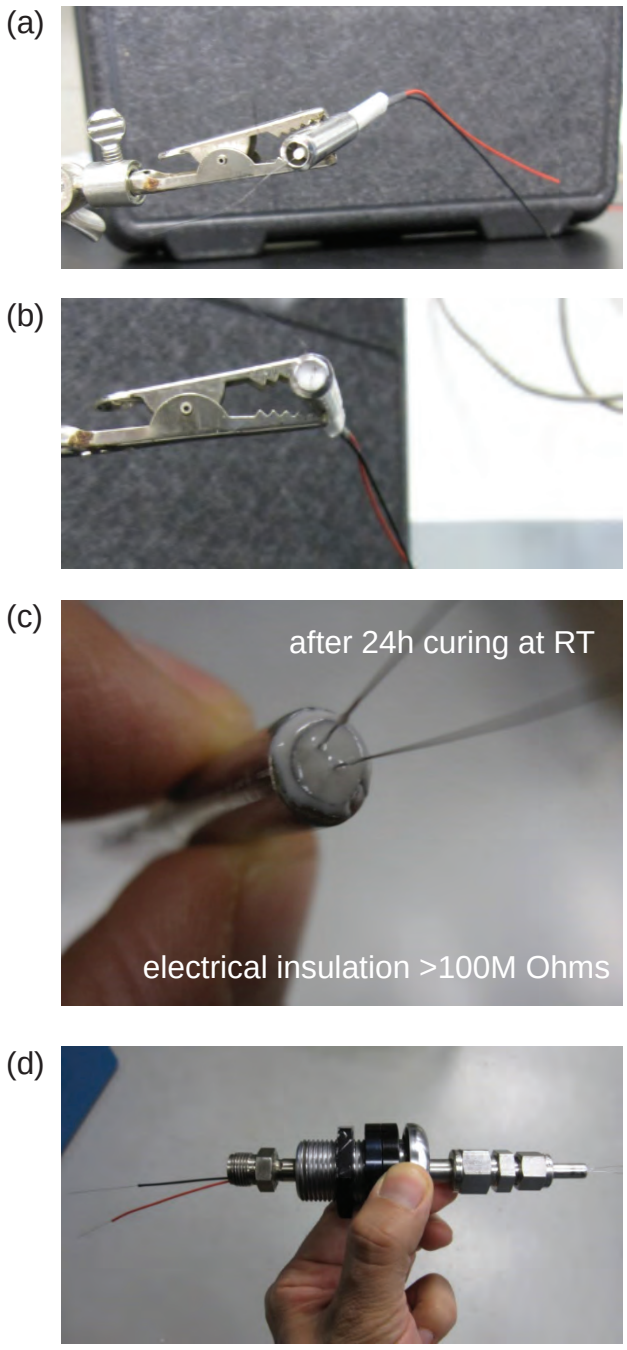

Figure 7.6: Making a custom thermocouple feedthrough for vacuum chambers. **(a)** For easy placement and isolation between two wires, the wires are inserted in a multi-bore alumina tube. The tube is then inserted into a stainless steel 1/4 in. tube. Stuffing in wax paper at one side of the tube can help to maintain the tube in a neutral position throughout the process. **(b)** The tube is filled in with TorrSeal epoxy. After applying the expoxy, the ceramic tube is pulled into the stainless steel tube to help move the epoxy in. Multiple cycles are repeated to get a thick layer of epoxy. **(c)** Cured at room temperature for a day. **(d)** The gas tube is attached to a commercial gas feed through using standard compression fittings with sleeves.

high vacuum, curable at room temperature (it is important to be able to easily cure without oxidizing the thermocouple wire), has extremely good adhesion and strength that works well as long as it is kept away from hot zones (< 90 °C). Ceramabond 552 (Armeco) is another good option that stands up to higher temperatures (up to 1600 °C), but it requires curing by annealing, has a shorter shelf life, and has inferior adhesion properties compared to TorrSeal. The process is illustrated in Fig.7.6.

References

[1] A. T. Burkov and M. V. Vedernikov, "Electrical and thermoelectric properties of disordered metallic binary continuous solid solutions", in *Condensed matter: disordered solids*, edited by S. K. Srivastava and N. H. March (World Scientific, 1995) Chap. 6, pp. 361–424.

[2] S. Iwanaga, E. S. Toberer, A. LaLonde, and G. J. Snyder, "A high temperature apparatus for measurement of the Seebeck coefficient", Review of Scientific Instruments **82**, 063905 (2011).

[3] H. Preston-Thomas, "The international temperature scale of 1990 (ITS-90)", Metrologia **27**, 3–10 (1990).

[4] H. Preston-Thomas, "Erratum: The international temperature scale of 1990 (ITS-90)", Metrologia **27**, 107 (1990).

[5] R. B. Roberts, "The absolute scale of thermoelectricity II", Philosophical Magazine B **43**, 1125–1135 (1981).

[6] R. B. Roberts, F. Righini, and R. C. Compton, "Absolute scale of thermoelectricity III", Philosophical Magazine B **52**, 1147–1163 (1985).

[7] R. K. Williams, F. W. Wiffen, J. Bentley, and J. O. Stiegler, "Irradiation induced precipitation in tungsten based, W-Re alloys", Metallurgical Transactions A **14**, 655–666 (1983).

[8] J. L. Rempe, D. L. Knudson, J. E. Daw, and S. C. Wilkins, "Type C thermocouple performance at 1500 °C", Measurement Science and Technology **19**, 115201 (2008).

Chapter 8

CONCLUDING REMARKS

Motivation to establish better charge transport analysis methods or procedures stemmed from the lack of successful effort in the literature for testing transport models with experimental data. Previously, experimental data have usually been interpreted by focusing on the temperature dependency of electrical conductivity, Seebeck coefficient, or Hall mobility. While these signatures do provide general clues in the early stage of investigation, there are many cases where experimental data have been reported with questionable interpretations or conclusions based on such simple temperature-dependency analyses.

In this thesis, it has been demonstrated that a simple analysis on the interrelation between the Seebeck coefficient and electrical conductivity offers powerful insight about transport mechanisms. Different mechanisms were more straightforwardly distinguished in the interrelation analysis, as exemplified by cases where previous interpretations regarding particular transport mechanisms were shown to be inconsistent with the claimed model by using only the data already reported in the same study. Some examples include: near-room temperature activated conduction in polycrystalline Mg_3Sb_2-based alloys shown to be from grain boundary resistance rather than ionized-impurity scattering; high temperature transport in n-type $SrTiO_3$ to be consistent with deformation potential scattering rather than polar optical phonon scattering, ionized impurity scattering, or electron-electron scattering; conducting polymers to have a dispersive transport spectrum rather than that described by hopping models with relatively narrow energy ranges.

Moreover, it has been shown that, from a more general perspective, the interrelation between transport properties could be understood as information about the underlying function that governs transport properties for a given Fermi-level. This function — the transport function — was shown to govern the Seebeck coefficient, conductivity, and also the Lorenz number of fermion quasiparticles. In this context, the analysis scheme established in this thesis could be viewed as an attempt to change the practice of testing physical models from an individually-projected level to a governing-function level; rather than comparing each measured property with a different function for each property, comparing the transport function, phenomeno-

logically determined from experiments, with the transport function underlying a particular physical or mechanistic model is found to be more useful.

Although this analysis framework was able to yield new insight in the numerous cases tackled throughout this thesis, certain challenges and limitations are expected to be encountered when applied to a wider variety of cases with increased complexity. All cases studied in this thesis followed one of the archetype type functional forms; however, in general, deviations from such typical behavior can result from a variety of causes. For example, in band conductors, when multiple bands with different symmetry are involved, the transport function becomes more complicated than a simple power dependency on energy. Other complexities such as strong intervalley scattering, multiple scattering processes with comparative rates, or strong non-parabolicity near the band edge could potentially make the transport analysis more difficult. In hopping conductors, the narrow energy treatment might prove to be an oversimplification especially at lower temperatures. Another big question related to the analysis framework described in this thesis is the influence of electron-electron interactions; at a certain point, strong interactions are anticipated to make the fermion quasiparticle description not effective. Last, but not least, is the inherent limitation in the ability to flesh out mechanistic details about transport from the interrelation analysis. For example, although the transport function of $SrTiO_3$ was found to be consistent with deformation potential scattering in its energy and temperature dependency, it is not clear why such a simple behavior, as if determined by a single deformation potential value, is observed when different phonon branches are supposed to be involved. On one hand, this is also an inherent limit on the information that can be inferred from transport analysis. On the other hand, one might be able to benefit from expanding the Seebeck coefficient-conductivity analysis to, for example, strain dependencies. Much benefit is anticipated from future studies tackling these challenges and limitations.

As a final remark, it is hoped that the charge transport analysis framework shown here becomes a useful tool especially for experimentalists. With increased reports on the Seebeck coefficient and its interrelation to conductivity, facilitation of a better understanding on charge transport and related fundamental properties of the solid-state is anticipated.

Appendix A

NEAR-EQUILIBRIUM TRANSPORT EQUATIONS: THERMODYNAMIC PHENOMENOLOGY

The transport properties like conductivity in Ch.1 were defined based on the linear response regime where departure from an equilibrium quantity was described with the leading order term of the equilibrium-restoring process that produced a flux linearly proportional to the departure from equilibrium (*e.g.* Current density according to a linear Ohm's law to restore a charge distribution to a state where electric field is zero). This leading order term of the equilibrium-restoring process was also the recurring theme in the Boltzmann transport equation solving.

Transport phenomena can be understood in more general terms of the thermodynamics for irreversible processes, which leads to thermodynamic phenomenology that defines transport properties and also explains certain identities such as the Kelvin relations (relations between the Seebeck coefficient, Peltier coefficient, and Thompson coefficient). In this appendix [1], the heat and charge transport will be described in terms of generalized driving forces and fluxes. The second Kelvin relation will be obtained using Onsager reciprocity.

A.1 Generalized forces, fluxes, and Onsager reciprocity

An equilibrium state is when there is no change in entropy dS with respect to any system variable ξ_i. In non-equilibrium, the change in entropy could be written in an expansion form:

$$dS = \sum_i \frac{dS}{\delta \xi_i} \delta \xi_i + \ldots, \tag{A.1}$$

where $dS > 0$ and entropy is always produced. Then, the leading order term for entropy production rate (entropy source strength) is

$$\frac{dS}{dt} = \sum_i F_i \frac{\delta \xi_i}{dt}, \tag{A.2}$$

where $F_i = \frac{dS}{\delta \xi_i}$ is a "generalized force" that drives the system back to equilibrium with the means of a "generalized flux" $\frac{\delta \xi_i}{dt}$. When the irreversible processes in a system

[1] Symbols in this appendix will be defined independently from those in other chapters to deliver the content more easily with conventional thermodynamics convention. Here, S is entropy and the Seebeck coefficient is replaced with α. Fluxes will be generalized to $\boldsymbol{J}_i$ with i indicating the species or kind. μ is chemical potential rather than mobility.

are described with this linear term F_i, it is referred to as "near-equilibrium" and produces a steady-state such that fluxes are proportional to F_i's. In near-equilibrium, equilibrium thermodynamic variables such as temperature T or chemical potential μ are well defined at a local position in space as stationary states that minimize the local entropy production [1]. Therefore, non-equilibrium phenomena can be described with equilibrium thermodynamic variables.

Onsager coefficients L are defined as the proportional constants between the generalized forces and fluxes:

$$\frac{\delta\xi_i}{dt} = \sum_{ij} L_{ij} F_j. \tag{A.3}$$

For a single isolated process ($i = j$), the flux only depends on its own driving force. In general, however, any generalized driving force F_j in the system can drive other fluxes $\frac{\delta\xi_i}{dt}$ ($i \neq j$) as long as the Onsager coefficient is non-zero ($L_{ij} \neq 0$). Time-reversal symmetry dictates certain identities between these "interference" terms, which is the Onsager reciprocity. For parameters ξ_i such as energy or particle number that do not depend on the direction of particle motion (even parity), the Onsager reciprocity relation is

$$L_{ij} = L_{ji}. \tag{A.4}$$

A.2 Charge transport from electric fields and temperature gradients

Primary interest here is charge transport under the presence of two driving forces: an electric field $\boldsymbol{E}$ and temperature gradient ΔT. Because not just charge but also heat is transported, Eq.A.3 suggests that both fluxes need to be considered for a complete and proper description which takes into account of the interference terms ($i \neq j$). We wish to identify the forms of the generalized forces and fluxes in the presence of $\boldsymbol{E}$ and ΔT by finding expressions for the entropy production rate, but then how should flux be related to entropy? The answer depends on how one decides to define heat flux (the non-uniqueness of heat flux is discussed in Ref.[1]). The definition we will use here is

$$\boldsymbol{J}_Q = T\boldsymbol{J}_S, \tag{A.5}$$

where $\boldsymbol{J}_Q$ and $\boldsymbol{J}_S$ are heat flux and entropy flux, respectively. This definition was used by Callen [2] and is in analogy to the equilibrium thermodynamic relation $\delta Q = TdS$. This definition seems to be more popular in the literature, possibly because it is more intuitive. The flux equations containing the Onsager coefficients

depend on the heat flux definition, but the description for final physical quantities are not affected[2].

To use Eq.A.5 to relate entropy production to charge flux, we use the thermodynamic identity for open systems under an electric potential (no mechanical work is considered):

$$\begin{aligned} dU &= TdS + \sum_i (\mu_i + q_i\phi) dN_i \\ &= TdS + \sum_i \tilde{\mu}_i dN_i. \end{aligned} \tag{A.7}$$

Here U is internal energy, q is particle charge, and ϕ is electric potential. $\tilde{\mu}_i$ is an alternate definition for chemical potential including the long range electric potential contribution. To make connection to Eq.A.5, the identity Eq.A.7 is converted to fluxes:

$$\boldsymbol{J}_U = T\boldsymbol{J}_S + \tilde{\mu}_\mathrm{e}\boldsymbol{J}_\mathrm{e}, \tag{A.8}$$

where $\boldsymbol{J}_U$ is energy flux and $\boldsymbol{J}_\mathrm{e}$ is the particle number flux of charges. Since we are only considering electronic charge carriers, no other particle species appear in this flux equation.

Recall that an expression for entropy production rate is needed (Eq.A.2) to find generalized forces and fluxes. In steady-state, local entropy production is equal to the divergence of entropy flux such as $dS/dt = \nabla \cdot \boldsymbol{J}_S$, which can be used to find the entropy production rate from Eq.A.8. Noting that there is no divergence in energy or particle (conserved quantities) fluxes at steady-state ($\nabla \cdot \boldsymbol{J}_U = 0$ and $\nabla \cdot \boldsymbol{J}_\mathrm{e} = 0$, respectively), it is found that

$$\begin{aligned} \frac{dS}{dt} &= \nabla \cdot \boldsymbol{J}_S \\ &= \boldsymbol{J}_U \cdot \nabla\left(\frac{1}{T}\right) - \boldsymbol{J}_\mathrm{e} \cdot \nabla\left(\frac{\tilde{\mu}_\mathrm{e}}{T}\right). \end{aligned} \tag{A.9}$$

Although this equation identifies generalized [force $\leftrightarrow$ flux] pairs as $\left[\nabla\left(\frac{1}{T}\right) \leftrightarrow \boldsymbol{J}_U\right]$ and $\left[\nabla\left(\frac{\tilde{\mu}_\mathrm{e}}{T}\right) \leftrightarrow -\boldsymbol{J}_\mathrm{e}\right]$ through comparison with Eq.A.2, it is favored to have an

[2] Another definition worth noting is the one used by deGroot [1] in his monograph which is one of the most complete and comprehensive references on non-equilibrium transport.

$$\boldsymbol{J}_Q^{\mathrm{deGroot}} = T\boldsymbol{J}_S + \sum_i \mu_i J_i, \tag{A.6}$$

where μ_i is the chemical potential of species i and $\boldsymbol{J}_i$ is its flux. When reading the literature, it should be kept in mind that depending on the heat flux definition the Onsager equations could be quite different and thus should not be mix-matched.

expression for $\boldsymbol{J}_Q$ rather than $\boldsymbol{J}_U$. Eqs.A.5 and A.8 can be substituted into Eq.A.9 to find

$$\frac{dS}{dt} = \boldsymbol{J}_Q \cdot \nabla\left(\frac{1}{T}\right) - \frac{\boldsymbol{J}_\mathrm{e}}{T} \cdot \nabla\tilde{\mu}_\mathrm{e}. \tag{A.10}$$

Here, the relevant pairs for generalized forces and fluxes are identified as $\left[\nabla\left(\frac{1}{T}\right) \leftrightarrow \boldsymbol{J}_Q\right]$ and $\left[\frac{\nabla\tilde{\mu}_\mathrm{e}}{T} \leftrightarrow -\boldsymbol{J}_\mathrm{e}\right]$. Associating the minus sign with either force or flux is an arbitrary choice.

The Onsager coefficients can then be defined from the flux equations:

$$\begin{aligned} \boldsymbol{J}_Q &= L_{\mathrm{QQ}}\nabla\left(\frac{1}{T}\right) + L_{\mathrm{Qe}}\frac{\nabla\tilde{\mu}_\mathrm{e}}{T} \\ -\boldsymbol{J}_\mathrm{e} &= L_{\mathrm{eQ}}\nabla\left(\frac{1}{T}\right) + L_{\mathrm{ee}}\frac{\nabla\tilde{\mu}_\mathrm{e}}{T}, \end{aligned} \tag{A.11}$$

where Onsager reciprocity (Eq.A.4) guarantees $L_{\mathrm{Qe}} = L_{\mathrm{eQ}}$. By rewriting the equation in terms of conventional forms of driving forces:

$$\begin{aligned} \boldsymbol{J}_Q &= -\frac{L_{\mathrm{QQ}}}{T^2}\nabla T + \frac{L_{\mathrm{Qe}}}{T}\nabla\tilde{\mu}_\mathrm{e} \\ \boldsymbol{J}_\mathrm{e} &= +\frac{L_{\mathrm{eQ}}}{T^2}\nabla T - \frac{L_{\mathrm{ee}}}{T}\nabla\tilde{\mu}_\mathrm{e}. \end{aligned} \tag{A.12}$$

Now, transport properties can be expressed in terms of these Onsager coefficients. Current density $\boldsymbol{I}$ is $q\boldsymbol{J}_\mathrm{e}$ (recall that q contains a sign) and the measured or observed potential gradient is $\nabla\tilde{\mu}_\mathrm{e}/q$ (rather than just $\nabla\phi$ as was discussed in footnote 6 in Ch.1). Electrical conductivity σ therefore becomes

$$\sigma = \left.\frac{q\boldsymbol{J}_\mathrm{e}}{-\nabla\tilde{\mu}_\mathrm{e}/q}\right|_{\nabla T=0} = e^2\frac{L_{\mathrm{ee}}}{T}, \tag{A.13}$$

where q^2 was replaced with e^2 since the sign of q does not matter in squared from. The Seebeck coefficient α is defined at $\boldsymbol{J}_e = 0$, which gives

$$\alpha = \left.\frac{-\nabla\tilde{\mu}_\mathrm{e}/q}{\nabla T}\right|_{\boldsymbol{J}_\mathrm{e}=0} = -\frac{L_{\mathrm{eQ}}}{qTL_{\mathrm{ee}}}. \tag{A.14}$$

The Peltier coefficient Π is obtained as

$$\Pi = \left.\frac{\boldsymbol{J}_Q}{q\boldsymbol{J}_\mathrm{e}}\right|_{\nabla T=0} = -\frac{L_{\mathrm{Qe}}}{qL_{\mathrm{ee}}}. \tag{A.15}$$

Recall that $L_{\mathrm{Qe}} = L_{\mathrm{eQ}}$ from Onsager reciprocity. Then Π and α can be related from Eqs.A.14 and A.15:

$$\Pi = T\alpha, \tag{A.16}$$

which is the second Kelvin relation.

References

[1] S. R. de Groot and P. Mazur, *Non-equilibrium thermodynamics*, Dover edition, 1984 (North-Holland Pub. Co., 1962).

[2] H. B. Callen, "The application of Onsager's reciprocal relations to thermo-electric, thermomagnetic, and galvanomagnetic effects", Physical Review **73**, 1349–1358 (1948).

INDEX

definition of $\boldsymbol{E}^{\mathrm{obs}}$ (effective electric field in a solid), 7
definition of η (reduced Fermi-level), 17
definition of η (reduced Fermi-level, generalized), 23
definition of κ_{B} (bipolar thermal conductivity), 98
definition of κ_{e} (electronic thermal conductivity), 11
definition of κ_0 (zero-field electronic thermal conductivity), 11
definition of μ_{cl} (classical mobility), 95
definition of μ_0 (mobility parameter), 17
definition of μ_{w} (weighted mobility), 17
definition of σ (conductivity), 6
definition of $\sigma_E(E)$ (transport function), 22
definition of σ_{E_0} (transport coefficient, dispersive), 23
definition of σ_{E_0} (transport coefficient, narrow), 25
definition of B (dimensionless thermoelectric material quality factor), 92
definition of B_1, B_2 (dimensionless thermoelectric material quality factors, for peak zT with bipolar conduction), 101
definition of L (Lorenz number), 10
definition of m^*_{DOS} (density-of-states effective mass), 18
definition of m^*_{H} (Hall effective mass), 18
definition of m^*_{Seeb} (Seebeck effective mass), 79
definition of m^*_{b} (band effective mass), 13
definition of m^*_{I} (inertial effective mass), 22
definition of n_{H} (Hall carrier concentration), 12
definition of r_{H} (Hall factor), 12
definition of R_{H} (Hall coefficient), 12
definition of S (Seebeck coefficient), 7
definition of s (transport exponent), 23
defintion of E_{t} (transport edge), 23

figures, 8, 24, 31–33, 35, 38, 39, 50, 51, 53, 54, 63, 65, 67–69, 71–73, 78–80, 82, 83, 85, 91, 94–96, 100, 106–110, 112

tables, 16, 58, 70